

Dynamic stall characterisation and control for vertical-axis wind turbines

Présentée le 13 janvier 2023

Faculté des sciences et techniques de l'ingénieur
Laboratoire de diagnostic des écoulements instationnaires
Programme doctoral en énergie

pour l'obtention du grade de Docteur ès Sciences

par

Sébastien LE FOUEST

Acceptée sur proposition du jury

Prof. J. A. Schiffmann, président du jury
Prof. K. A. J. Mulleners, directrice de thèse
Prof. C. Simão Ferreira, rapporteur
Prof. Ph. Chatelain, rapporteur
Prof. F. Porté-Agel, rapporteur

Nothing has such power to broaden the mind
as the ability to investigate systematically and truly
all that comes under thy observation in life.
— Marcus Aurelius



ACKNOWLEDGEMENTS

Gratitude is a complex emotion that cannot easily be conveyed using words. Here I give a superficial account of my deep gratitude towards those who supported me throughout my journey leading to and throughout this thesis.

To my supervisor, for giving me the tools to succeed as a doctoral student. You taught me to ask the right questions rather than giving me answers. You helped me develop structured reasoning, break things down when they were overwhelming, and align laser sheets straighter than ever. I could not have asked for a better example to follow. To our administrative assistant, for demonstrating what being organised actually means. To my colleagues, for giving me the impression that academic research can be a team effort. We all carried each other at some point. We shared a stimulating, caring, and delightful work environment that I will always keep close to my heart. Nice, UNFoLD people, nice!

To the mechanical engineering workshop, for your dedication to making us better engineers. You could turn our sketchy designs into marvels in the blink of an eye, but you took advantage of every opportunity to share your know-how in the process. To the Cubotron electronic workshop, for bearing with my rudimentary understanding of electronics. Your patience, competence and kindness were invaluable and took my work to new heights.

To those who brought spice to my routine throughout these years. To Bilia, for giving us a reason to look forward to Thursday lunchtime. To my basketball team, for keeping me healthy and happy. To the science communication people, for helping me concretise a growing passion and welcoming me into an exciting, nurturing and meaningful community.

To my friends, for pulling me out of everyday life to make memories, share laughs and put things back into perspective. To my TPE crew, for being the mentos to my Coca-Cola. To my past and current flatmates, for being family when I was far from mine. To my girlfriend, for giving me a reason to grow and a partner to find paths in life's chaos. To my brothers, for catching me when I fall and for being the best partners-in-crime. To my parents, for nurturing me with limitless love and imparting me the values that lead me to this achievement.

Lausanne, December 21, 2022

S. L. F.



ABSTRACT

According to the International Energy Agency, the global *net-zero emissions* objective requires the installed wind power capacity to increase 11-fold between 2020 and 2050. The scientific community has recently voiced concerns about the logistic feasibility of scenarios expecting wind power to meet this target. The deployment of wind energy capacity is limited by the availability of exploitable land. Wake effects are also a significant concern, whereby the installation of new wind farms alters wind conditions and decreases the power generation of wind farms downwind. Increasing the versatility of wind turbine technologies can mitigate concerns around land use and interaction.

Vertical-axis wind turbines provide an attractive design that complements their ubiquitous horizontal-axis counterparts. These turbines can operate in a broad range of wind conditions and emit little noise during operation, making them ideal for urban applications. The structural soundness of vertical-axis wind turbines has also attracted industrial attention for off-shore floating applications. However, the aerodynamic complexity of vertical-axis wind turbines has hampered their industrial deployment.

The blades of a vertical-axis wind turbine encounter varying flow conditions throughout a single turbine rotation, even in a steady wind. When the turbine operates at a low rotational velocity compared to the incoming flow velocity, the blades perceive significant amplitude changes in the angle of attack and relative wind velocity. Varying flow conditions can give rise to flow separation and dynamic stall. Dynamic stall is characterised by the formation, growth, and shedding of large-scale vortices. Vortices are known for enhancing the aerodynamic force experienced by the surface they form on. Although this attribute appears beneficial, dynamic stall is generally not considered desirable. For wind turbine applications, the shedding of large-scale vortices leads to a significant loss in efficiency and load transients that jeopardise the turbine's structural integrity.

This thesis has two main objectives: characterise the occurrence of dynamic stall on vertical-axis wind turbines and investigate control strategies to mitigate the undesirable consequences of dynamic stall. The first step in this endeavour was to study the fundamental role of motion frequency in stall occurrence. We use a simple pitching wing apparatus and perform ramp-up manoeuvres at frequencies ranging from extremely slow to dynamic. Stall timescales

Abstract

are shown to become independent from motion frequency for reduced frequencies below $k \approx 10^{-4}$. A universal power law described the evolution of stall delay against reduced frequency for three different airfoil profiles operating at vastly different Reynolds numbers and undergoing different pitch profiles. At high reduced frequencies ($k > 0.04$), stall onset tends towards a fixed value of about 4 convective times. This value represents the smallest amount of time required for a blade to stall and corresponds to the universal vortex formation time.

The second step was to experimentally investigate the occurrence of dynamic stall on a single-bladed vertical-axis wind turbine model. We conceived an experimental apparatus that allowed us to obtain time-resolved force and flow measurements on a wind turbine blade for a wide operating envelope. We focus on the interplay between the instantaneous aerodynamic performance of the wind turbine blade and the flow structures forming on the surface of the blade. Our findings highlight the dynamic stall dilemma for wind turbine blades. Dynamic stall vortices forming on the turbine blades yield a significant peak in power production, but post-stall conditions lead to prolonged torque-dissipating excursions of the aerodynamic force. We also distinguish and quantify the timespan of six characteristic stall stages: the attached flow, shear-layer growth, vortex formation, upwind stall, downwind stall, and flow reattachment stage.

Lastly, we demonstrate the potential of dynamic blade pitching as a control strategy to enhance wind turbine performance. We couple the scaled-down turbine model to a genetic algorithm optimiser that performed unsupervised experiments to seek optimal pitching kinematics at on and off-design operating conditions. Optimal blade kinematics yielded a three-fold power coefficient increase at both operating conditions compared to the non-actuated turbine and a 70 % reduction in structure-threatening load fluctuations at off-design conditions. Flow measurements uncover how blade pitching manipulates flow structures to achieve performance enhancement.

RÉSUMÉ

Pour atteindre l'objectif 2050 de zéro émission nette, la production mondiale d'énergie éolienne doit être multiplié par 11 dans les trois décennies à venir selon l'Agence Internationale d'Énergie. La communauté scientifique a émis des doutes par rapport à la viabilité de cet objectif, notamment dû à la disponibilité des terrains où l'énergie éolienne serait exploitable. Les effets de sillage, longtemps sous-estimés, sont une source de préoccupations. Ces effets limitent la rentabilité d'un parc éolien lorsqu'il se situe dans le sillage, même distant, d'un autre parc. Une solution pour accroître les surfaces potentielles pour l'exploitation d'énergie éolienne serait d'augmenter la polyvalence des éoliennes.

Les éoliennes à axe de rotation vertical proposent de nombreux avantages qui leur permettraient d'être complémentaires aux éoliennes traditionnelles dans la production d'électricité. Le fonctionnement des éoliennes à axe de rotation vertical émet peu de bruits et leur performance ne dépend pas de la direction du vent. Ces éoliennes sont également considérées comme plus esthétiques, ce qui en fait de parfaites candidates pour une intégration urbaine. Leur centre de gravité se trouve proche de la base de la structure ce qui est très avantageux pour une installation flottante en mer. Cependant, le déploiement massif des éoliennes à axe de rotation vertical est restreint par leur complexité aérodynamique.

Les pâles d'éoliennes à axe de rotation verticales perçoivent une variation continue de l'écoulement qui les entoure, même dans des conditions de vent stables. Quand leur fréquence de rotation est petite par rapport à la vitesse du vent, les variations de l'angle d'attaque et de la vitesse d'écoulement agissant sur les pâles deviennent considérables. Ces variations peuvent entraîner le décrochage dynamique de l'écoulement. Le décrochage dynamique se manifeste par la création de grands tourbillons sur la surface des pâles d'éoliennes. Ces tourbillons vont momentanément augmenter de façon significative la portance générée par les pâles. Si cet effet semble avantageux, il est généralement suivi par un décrochage du tourbillon et une perte importante de portance. Le décrochage dynamique implique aussi des vibrations structurelles qui peuvent mener à la destruction de l'éolienne à terme.

Cette thèse a deux objectifs : caractériser le décrochage dynamique sur les éoliennes à axe de rotation vertical et examiner des techniques de contrôle afin d'éviter les effets néfastes du décrochage dynamique. La première étape a été d'examiner la relation fondamentale entre

Résumé

la fréquence du mouvement de la pôle et le déroulement du décrochage. On a étudié le cas de figure simplifié du tangage d'une pôle dans un écoulement stationnaire. La fréquence de tangage a été variée pour couvrir le domaine du quasi-statique au dynamique. On démontre que le déroulement temporel du décrochage devient indépendant de la fréquence quand celle-ci est très basse $k \approx 10^{-4}$ ou très haute ($k > 0.04$). À haute fréquence, le décrochage se produit en 4 temps convectifs, ce qui équivaut à la valeur universelle de création de tourbillons. Pour les fréquences intermédiaires, le temps dont l'écoulement a besoin pour se décrocher de la pôle suit une loi universelle en puissance. Cette loi est vérifiée pour trois pôles de forme différentes, à trois nombres de Reynolds différents et sujettes à deux formes distinctes de tangage (sinusoïdale et linéaire).

La deuxième étape était d'investiguer le déroulement du décrochage dynamique sur un modèle réduit d'éolienne à une pôle. La conception d'un dispositif expérimental nous a permis d'obtenir des mesures de force et d'écoulement à haute résolution temporelle sur une pôle d'éolienne pour une grande fourchette de conditions de fonctionnement. La performance aérodynamique de la pôle a systématiquement été mise en relation avec l'écoulement qui l'entourait pour les différentes conditions de vent. Nos résultats soulignent le dilemme que présente le décrochage dynamique aux pôles d'éoliennes. La création de grands tourbillons génère un moment important qui participe à la rotation de l'éolienne, mais leur décrochage frêne la rotation et impose des contraintes structurelles. Le déroulement du décrochage a été divisé en 6 étapes dont la durée a été caractérisée pour les différentes conditions de vent.

Finalement, nous avons évalué le potentiel d'une stratégie qui consiste à ajuster l'angle d'attaque de la pôle en temps réel afin d'améliorer la performance et la résilience des éoliennes à axe de rotation verticale. L'éolienne a fonctionné sans supervision à l'aide d'un algorithme génétique qui cherchait à trouver la manière optimale de positionner la pôle au long de sa rotation pour deux conditions de vent. L'une mène au décrochage dynamique et l'autre était celle pour laquelle le rendement de l'éolienne sans actuation était maximal. Le but était de maximiser le rendement de l'éolienne tout en minimisant les contraintes structurelles générées par le décrochage de l'écoulement. L'algorithme a convergé pour les deux conditions de vent vers une solution qui multiplie par 3 le rendement de l'éolienne par rapport au fonctionnement sans actuation de la pôle. Pour les conditions de vent qui menaient au décrochage dynamique, l'actuation a également réussi à diminuer les contraintes de 70 %. Les mesures d'écoulement nous ont permis d'expliquer l'origine de ces améliorations.

CONTENTS

Acknowledgements	i
Abstracts	ii
Contents	vii
List of Figures	xi
Introduction	xv
I Groundwork	1
1 State-of-the-art	3
1.1 Vertical-axis wind turbines	4
1.1.1 Brief history	4
1.1.2 Advantages and applications	5
1.1.3 Basic aerodynamics	6
1.2 Dynamic stall	9
1.3 Rotational effects	12
1.4 Influence of governing parameters on turbine power performance	13
1.4.1 Reynolds number influence	13
1.4.2 Chord-to-diameter influence	14
1.4.3 Tip-speed ratio influence	16
1.5 Blade pitch control	16
2 The dynamics of static stall	19
2.1 Introduction	20
2.2 Experimental setup	21
2.3 Results	23
2.4 Conclusion	33
3 Experimental apparatus: design and validation	35
3.1 Design of a modular H-Darrieus wind turbine	36
3.2 Instrumentation of the blade shaft	38
3.2.1 Load cell conception	38
3.2.2 Load cell calibration	40
	vii

Contents

3.2.3	Load cell uncertainty quantification	40
3.2.4	Load cell aerodynamic validation	42
3.3	Isolation of aerodynamic forces on the wind turbine blade	44
3.4	Design of a rotating mirror apparatus	47
3.5	Performing time-resolved force and flow measurements in a recirculating water channel	48
3.6	Data processing	49
3.6.1	Filtering	49
3.6.2	Force projection and non-dimensionalisation	50
3.6.3	Flow measurement mapping	51
3.6.4	Phase-averaging	53
 II Dynamic stall on vertical-axis wind turbines revisited		55
 4 The dynamic stall dilemma		57
4.1	Introduction	58
4.2	Experimental apparatus and methods	59
4.2.1	Vertical-axis wind turbine model	59
4.2.2	Force measurements	59
4.2.3	Particle image velocimetry	59
4.3	Results	61
4.4	Conclusion	73
 5 Timescales of dynamic stall development		75
5.1	Introduction	76
5.2	Experimental apparatus and methods	77
5.3	Results	78
5.4	Conclusion	89
 III Flow control on vertical-axis wind turbines		91
 6 The role of blade pitch angle in dynamic stall development		93
6.1	Introduction	94
6.2	Experimental methods	95
6.3	Results	95
6.4	Conclusion	99
 7 Optimal blade pitching kinematics		101
7.1	Introduction	102
7.2	Experimental methods	103
7.2.1	Kinematics parametrisation	103
7.2.2	Genetic algorithm	105
7.2.3	Flow conditions	105
7.3	Results	106

7.3.1	Performance overview	106
7.3.2	Off-design flow control	109
7.3.3	On-design flow control	111
7.4	Discussion	111
	Conclusion	115
	Bibliography	119
	Curriculum Vitae	127

LIST OF FIGURES

1.1	Schematic drawings of different vertical-axis wind turbine designs	4
1.2	Vertical-axis wind turbine aerodynamics diagram.	6
1.3	Temporal variation of the effective angle of attack α_{eff} and velocity U_{eff} of a wind turbine blade.	8
1.4	Temporal variation of the effective angle of attack α_{eff} and velocity U_{eff} of a wind turbine blade for different chord-to-diameter ratios.	9
1.5	Schematic representation of the characteristic stages occurring during dynamic stall.	10
1.6	Phase-averaged lift coefficient as a function of angle of attack for a blade undergoing static and dynamic stall.	11
1.7	Negative vorticity field around a vertical-axis wind turbine blade undergoing dynamic stall.	12
1.8	Schematic illustration of the conformal transformation from a symmetric airfoil in a curved flow to a cambered airfoil in a rectilinear flow.	13
1.9	Parametric evolution of power coefficient against tip-speed ratio for various turbine solidities	15
1.10	Schematic drawings of synchronous and active blade pitching designs.	16
2.1	Schematic representation of the pitching wing setup.	22
2.2	Lift coefficient response for a pitching blade undergoing an infinitely slow ramp-up motion and a blade undergoing a small amplitude step-wise increase in the angle of attack.	24
2.3	Drop time occurrence histogram for all runs of the slow continuous ramp-up and the step manoeuvre	25
2.4	Relaxation delay occurrence histogram for all runs of the slow continuous ramp-up and the step manoeuvre.	26
2.5	Reaction delay occurrence histogram for all runs of the slow continuous ramp-up and the step manoeuvre.	27
2.6	Ensemble-averaged temporal evolution of lift coefficient and of the amplitude spectrum of the lift coefficient for the transient portion of the slow continuous ramp-up manoeuvre and the step manoeuvre.	27
2.7	Reaction time against load fluctuations for all runs of the slow continuous ramp-up manoeuvre and the step manoeuvre.	29

List of Figures

2.8	Relaxation time against load fluctuations for all runs of the slow continuous ramp-up manoeuvre and the step manoeuvre.	30
2.9	Average reaction time delay as a function of reduced pitch rate for three different airfoils operating at different Reynolds numbers and undergoing different manoeuvres.	31
2.10	Estimated static stall angle accuracy and the corresponding inertial component of the lift coefficient against reduced frequency for static stall measurements performed with a continuous and uniform ramp-up motion.	32
3.1	Schematic representation of the scaled-down H-type Darrieus wind turbine model with an instrumented shaft and active individual blade pitching. . .	37
3.2	Load cell design diagram.	39
3.3	Orthogonal calibration rig for the wind turbine's load cell	41
3.4	Force measured by the load cell in the tangential direction compared to reference force applied with a static weight.	42
3.5	Lift and drag coefficients against angle of attack of the wind turbine blade undergoing an infinitely slow ramp up.	43
3.6	Free body diagram of the forces experienced by the turbine blade during wind turbine experimentation.	44
3.7	Centripetal force acting on the turbine blade measured and modelled.	45
3.8	Tangential force related to the turbine splitter plates.	46
3.9	Schematic representation of the rotating mirror system for particle image velocimetry.	47
3.10	Schematic of the experimental setup including the wind turbine model, the light sheet, the rotating mirror system and high-speed camera for particle image velocimetry.	49
3.11	Force direction diagram.	50
3.12	Mapping diagram for processed particle image velocimetry	52
4.1	Experimental apparatus to investigate dynamic stall on vertical-axis wind turbines.	60
4.2	Total force and flow measurements for a wind turbine blade at tip-speed ratio 1.5.	62
4.3	Total force and flow measurements for a wind turbine blade at tip-speed ratio 3.0.	64
4.4	Tangential force evolution across tip-speed ratios ranging from 1.2 to 6.	65
4.5	Normalised circulation around the turbine blade operating at tip-speed ratios ranging from 1.2 to 3.	66
4.6	Proposed quantities to assess the magnitude of stall induced load transients.	67
4.7	Stall induced load transients against tip-speed ratio.	68
4.8	Quantification of the dynamic stall delay using the pitching moment.	69
4.9	Dynamic stall delay as a function of the reduced frequency for the vertical-axis wind turbine operating at tip-speed ratios ranging from 1.2 to 4.	70
4.10	Theoretical parametric dynamic stall regime map	71
4.11	Power coefficient against tip-speed ratio for a single-blade wind turbine model.	72

5.1	Polar plot of the temporal evolution of the phase-averaged power coefficient C_p and vorticity field for a wind turbine blade operating at tip-speed ratio $\lambda = 1.5$.	79
5.2	Normalised eigenvalues associated with the first ten spatial POD modes for different tip-speed ratios.	80
5.3	First three spatial POD modes and the evolution of the corresponding time coefficients.	81
5.4	Dynamic stall stages identified using the POD time coefficients.	83
5.5	Duration and timing of dynamic stall stages.	85
5.6	Pitching moment coefficient and first POD mode time coefficient comparison.	86
5.7	Dynamic stall stages identified using the aerodynamic loads.	87
5.8	Stage-wise contribution to the total work completed by the total aerodynamic force throughout the blade's rotation.	89
6.1	Temporal variation of the effective angle of attack for a wind turbine blade with a blade pitch-angle offset.	94
6.2	Wind turbine performance comparison for pitch-angle offset ranging from -24° to 5°	96
6.3	Polar plot comparison of wind turbine blades operating at tip-speed ratio $\lambda = 1.5$ with no pitch-angle offset and a -4° pitch-angle offset	98
7.1	Overview of the experimental apparatus and methodology used to perform the blade pitch profile optimisation.	104
7.2	Optimisation performance overview for all 1860 tested individuals at tip-speed ratio $\lambda = 1.5$, with a focus on optimal kinematics.	107
7.3	Optimisation performance overview for all 2280 tested individuals tip-speed ratio $\lambda = 3.2$, with a focus on optimal kinematics.	108
7.4	Polar plot comparison of the turbine's performance for both the non-actuated case and the optimal kinematics at tip-speed ratio $\lambda = 1.5$	110
7.5	Polar plot comparison of the turbine's performance for both the non-actuated case and the optimal kinematics at tip-speed ratio $\lambda = 3.2$	112
7.6	Graphic summary of optimal pitching kinematics and flow physics enabling performance enhancement.	113



INTRODUCTION

The role of wind energy in the global energy transition

Installed renewable energy capacity almost doubled from 2019 to 2021 according to the International Energy Agency, adding 575 GW to the world's supply in that three-year timespan [86]. Annual renewable energy capacity additions have broken records for the past three consecutive years, and the IEA does not expect the record to hold in 2022. This surge results from a growing corporate and governmental need to meet climate change targets for 2030 and secure energy supplies in a disrupted political climate and energy market.

Nevertheless, the path to net zero emissions by 2050 is narrow. For solar power, it requires installing the world's largest solar park roughly every day until 2030 [51]. We can only follow this path with massive deployment of all available clean energy technology, including renewables, energy-efficient building retrofits and clean transport solutions. The electrical grid needs to evolve from centralised, carbonated, and abundant electricity production to decentralised, well-coordinated and carbon-free power generation.

The installed wind power capacity is expected to increase 11-fold in scenarios that lead to net zero emissions from the electricity generation sector by 2040 [51]. The advent of offshore wind farms offers new territory for wind power production, led by China. The country added 16.9 GW of new offshore wind capacity in 2021 according to Bloomberg News, more than is installed in the entire European Union. The scientific community has recently voiced concerns about the logistic feasibility of scenarios expecting wind power to cover up to 31 % of the electricity supply by 2050 [8]. The deployment of wind energy capacity is limited by the availability of exploitable territory [31]. The installation of new wind farms are also a concern for existing neighbouring farms, as wake effects alter wind conditions and decrease the power generation of wind farms downwind [1, 67]. Increasing the versatility of wind turbine technologies can thus mitigate concerns around land use and interaction.

Vertical-axis wind turbines: a high-potential but challenging design

Vertical-axis wind turbines are excellent candidates to diversify wind turbine technology and increase wind power's installed capacity. These turbines have several advantages that make them attractive for wind energy exploitation in areas where their horizontal counterparts may face shortcomings. Advantages include insensitivity to wind direction and low noise emissions. Quiet and versatile are two key features that make vertical-axis wind turbines adequate for urban applications. The vertical axis of rotation also allows the design of structurally sound units. Heavy components from the drive train can be installed near the ground. Having mechanical parts near the ground facilitates maintenance, reduces structural loads and lowers the centre of mass, enabling floating offshore applications.

The industrial development of vertical-axis wind turbines was hampered by their inherent aerodynamic complexity. The turbine blades undergo a continuous variation in the flow conditions they experience, even in a steady wind. This variation can lead to unsteady flow phenomena, such as flow separation or dynamic stall. Dynamic stall is characterised by the formation, growth, and shedding of large-scale coherent vortices [15]. The shedding of large-scale vortices is generally followed by a dramatic loss in aerodynamic efficiency and highly unsteady loads, potentially leading to turbine failure. Though wind turbines generally operate at conditions that avoid the occurrence of dynamic stall, a change in wind condition can easily lead to dynamic stall. This thesis aims to address the occurrence of dynamic stall on vertical-axis wind turbines.

RESEARCH QUESTIONS

- ⊙ How does the frequency of blade kinematics influence the timescales of stall? Can a motion be slow enough to be considered static from the flow's perspective?
- ⊙ How do flow structures, such as leading-edge vortices, affect the blade's contribution to power production? How does this interplay evolve for changing wind conditions?
- ⊙ What is the sequence of events when a vertical-axis wind turbine blade undergoes dynamic stall? How do these timescales vary across operating conditions?
- ⊙ Can a wind turbine blade harness the lift-enhancing properties of leading-edge vortices using blade pitching? Can blade pitching enhance power performance at both off and on-design operating conditions?

Thesis outline

Part I offers a summary of the existing knowledge about the main topics discussed throughout this thesis. These topics include vertical-axis wind turbine design and performance, dynamic stall, rotational effects and flow control strategies. The first result chapter is included in part I because it investigates the fundamental relationship between the frequency of blade kinematics and flow separation from the blade's surface. The results from this chapter provide a tool to analyse the development of dynamic stall on wind turbine blades in the following part. Part I also provides an extensive description of the design, conception and validation of the experimental apparatus and methodology used to perform wind turbine experiments.

The characterisation of dynamic stall on vertical-axis wind turbine blades is presented in part II. The formation of stall vortices on the blade surface yields significant power production. These vortices eventually lift off from the blade's surface, leading to a drastic loss in aerodynamic performance and heavy load fluctuations. Turbine blades face a dilemma in which they need to find a compromise between torque generation and structural integrity. The dynamic stall dilemma is discussed in the first chapter of part II. The second chapter investigates the timescale of dynamic stall development. We use order reduction methods to decompose the problem and keep only the protagonists that dominate the flow physics. This simplified perception allows us to characterise the succession of landmark events we expect in the occurrence of stall. A sound understanding of the succession of these events can help improve our modelling and control strategies for wind turbine undergoing dynamic stall.

Natural flyers have learned to control the lift-enhancing properties of leading-edge vortices rather than avoiding their formation. Avian species continuously adjust the orientation of their wings to time the formation and release of vortical structures. Bio-inspired flow control strategies previously lead to significant performance improvements in wings interacting with vortices. The final part of this thesis investigates the potential of blade pitching to control flow structure forming on wind turbine blades. We first demonstrate the sensitivity of turbine power performance to a static change in blade pitch angle in chapter 6. Then, we performed an experimental optimisation of the blade's pitching kinematic at on and off-design operating conditions. The objective was to maximise the turbine's power coefficient while minimising the undesired load fluctuations related to flow separation from the blade's surface. The results of our open-loop control are presented in chapter 7.

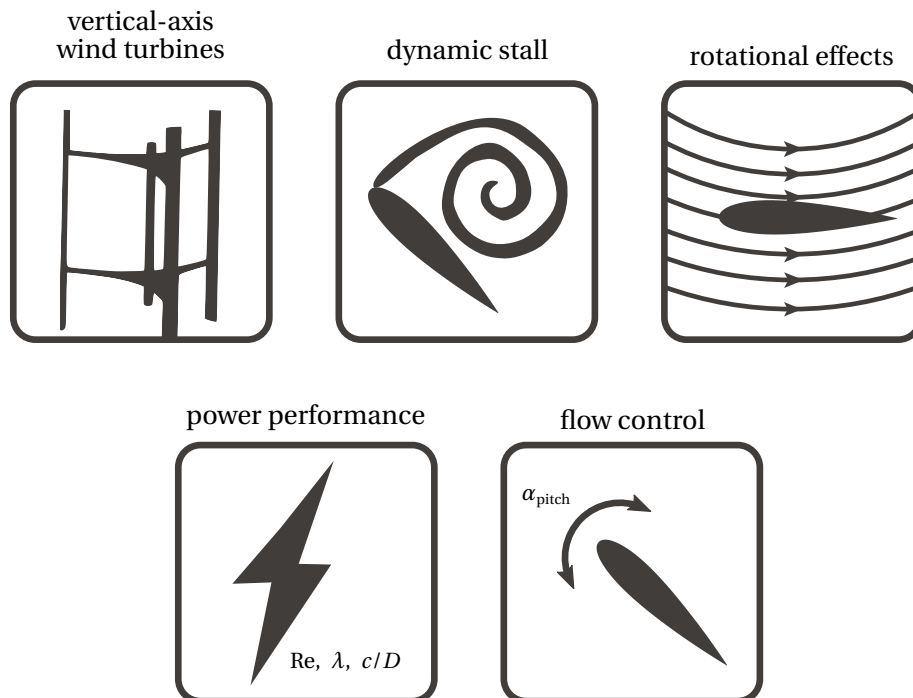
GROUNDWORK

PART I

1

STATE-OF-THE-ART

Vertical-axis wind turbines represent a fascinating case of unsteady aerodynamics that has attracted academic attention since the 1980s. The blades of vertical-axis wind turbines undergo continuous variations in flow conditions each rotation, even in a steady free stream. These complex aerodynamics were characterised by early work, but many practical challenges remained unanswered, driving the wind industry's attention towards horizontal-axis wind turbines. Since the turn of the millennium, academic interest in developing vertical-axis wind turbines is renewed by technological advances in flow control, measurements and simulations. This chapter offers a short literature review of the advancements in the main topics this thesis tackles, depicted below.



1.1 Vertical-axis wind turbines

1.1.1 Brief history

Humankind has long-endavoured to harness wind power to facilitate work-intensive tasks. The earliest known use of wind power is the sailboat. The first windmills appeared between the fifth and ninth century in Persia [52]. These windmills had a vertical axis of rotation, featured multiple flexible blades made out of reed or wood and were used to pump water and grind grains. Since then, a wide variety of vertical-axis wind turbine designs have emerged. These designs are generally divided into two categories: lift-based and drag-based design.

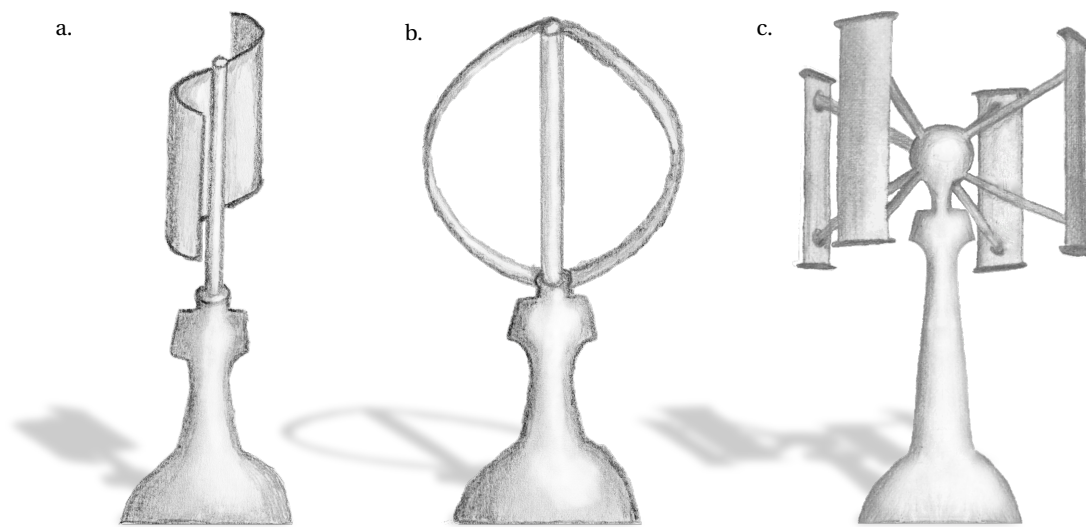


Figure 1.1: Schematic drawings of three vertical-axis wind turbine designs: a Savonius rotor (a), a Darrieus ϕ -shaped turbine (b), and an H-rotor (c).

The most notable drag-based wind turbine is the Savonius wind turbine, invented in 1922. The design is simple: two to three rounded cups are placed on a vertical axis, similar to a cup anemometer (figure 1.1 (a)). When the wind blows, the concave surface experiences a higher drag force than the the convex side. This drag differential generates a net torque that sets the turbine into motion. Savonius wind turbines are self-starting devices, but their efficiency is low.

Lift-based vertical-axis wind turbines rely on lift-producing wings to generate torque. The term *lift* is conventionally used to emphasise the opposition to the working principle of drag-based wind turbines, but it can be somewhat misleading. The aeronautical terms *lift* and *drag* typically refer to the decomposition of the aerodynamic force experienced by a wing into the directions across and along the incoming flow's direction. For wind turbine applications, we are interested in the aerodynamic force component tangential to the blade's circular path directed forwards. This propulsive force is in the opposite direction from the conventional drag force and results in net torque production.

The Darrieus wind turbine is the first lift-based vertical-axis wind turbine, patented in 1926. The original design had a ϕ -shaped rotor, characterised by its curved blades (figure 1.1 (b)). Another notable design is the H-shaped rotor, comprised of straight blades connected to a vertical axis with struts (figure 1.1 (c)). In modern wind technology history, Darrieus wind turbines are the only vertical-axis wind turbines to yield large-scale prototypes. These prototypes were primarily developed in North America in the 1970s and 1980s. FloWind achieved the most significant commercial exploitation of wind power using vertical-axis wind turbines in 1987. Over 500 ϕ -shaped Darrieus wind turbines were installed in California for a total rated capacity of 100 MW [52]. These units were efficient but suffered from early fatigue failure of the blades, which were designed to flex.

In the meantime, the European wind industry focused on developing horizontal-axis wind turbines. By 1991, Vestas sold its 1.000th wind turbine and released a 600 kW unit in 1994. Horizontal-axis wind turbines boast a simpler aeroelastic behaviour and enjoy longer fatigue lives, creating an edge over their vertical counterparts. The development of vertical-axis wind turbines suffered from a weak northern American wind energy market [36]. In contrast, horizontal-axis wind turbines reached technological maturity and prevailed as the best wind turbine design.

Modern horizontal-axis wind turbines are very efficient, with peak power coefficients close to 80 % of the theoretical Betz limit. Most research is now focused on wind farm design rather than the design of units. On the unit level, the rotor radius continues to increase to maximise wind capture area and minimise the levelised cost of energy. Largest rotor diameters exceed 150 m, pushing the limit of manufacturing and commissioning capabilities. In the race to the largest turbine diameter, horizontal-axis wind turbines sacrifice some versatility and land accessibility.

The growing demand for decentralised renewable energy systems and increased wind farm power density has driven the return of commercial vertical-axis wind turbines. Agile Wind Power, a Swiss start-up company, commissioned its second H-type 750 kW turbine prototype in Germany in June 2022. The turbine is designed to withstand a fatigue life of 25 years. Another wind power company named SeaTwirl has agreed to commission a 1 MW floating H-type turbine off the Norwegian coast by 2023. These wind turbines feature many advantages that make them excellent candidates to complement traditional wind turbines and increase the total wind energy capacity.

1.1.2 Advantages and applications

The orthogonal axis of rotation also makes wind turbines insensitive to wind direction, so a yawing mechanism is not required for the turbine to adapt to a change in wind direction. Vertical-axis wind turbines also prosper in highly sheared or even vortex-dominated flows such as those commonly encountered in an urban context [93, 104]. The versatility of these turbines enables the densification of existing wind farms, increasing their output by up to an order of magnitude [21, 93, 104]. Power density is a highly regarded attribute for renewable energy systems when compared to fossil energy.

Vertical-axis wind turbines often have structurally sound designs. A vertical axis of rotation allows the drive train to be installed near the ground. Having mechanical parts near the ground facilitates maintenance, reduces structural loads and lowers the centre of mass, enabling floating off-shore applications [13].

Typical rotational frequencies of vertical-axis wind turbine are lower than horizontal-axis turbines, yielding a much quieter turbine and reduced risk of collision with avian species [87, 100]. Current legislation for horizontal-axis turbines generally requires their installation to maintain large distances from habitable lands. Low noise emissions and versatility allow vertical-axis turbines to increase wind power accessibility and provide power to remote locations. Implementing decentralised electricity production in buildings is a crucial strategy for reaching a nearly carbon-free electrical grid by 2050 [51].

1.1.3 Basic aerodynamics

The basic aerodynamics of an H-type vertical-axis wind turbine are depicted in figure 1.2. Here, we consider six variables to characterise the flow physics of the wind turbine blades: the free stream velocity U_∞ , density ρ and kinematic viscosity μ , the turbine radius R and rotational frequency ω , and the blade's chord length c . This selection ignores the speed of sound and assumes flow compressibility effects are negligible. The influence of gravity as an external field acting on the flow is also ignored.

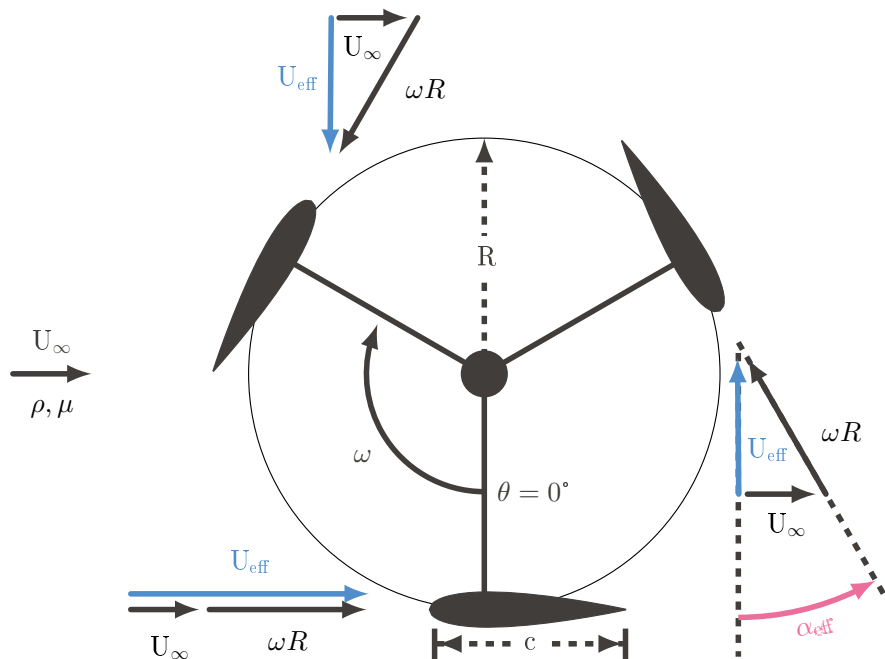


Figure 1.2: Vertical-axis wind turbine aerodynamics diagram. A fluid of density ρ and kinematic viscosity μ flows with a free stream velocity U_∞ that goes from left to right. The blade's velocity is equivalent to the rotational frequency ω times the turbine's radius R . The definitions of the blade's effective angle of attack α_{eff} and velocity U_{eff} are shown schematically.

According to the Buckingham π theorem, physically meaningful equations governing a three-dimensional problem with six variables can be written using three dimensionless parameters. Applying Buckingham π theorem requires selecting a set of three repeating variables such that all dimensions are included. There is no single solution to this step. The selection is subject to the problem's interpretation. This thesis focuses on blade-level physics, so we select the blade's rotational frequency ω and chord c as characteristic timescale and length and complete our selection with the flow density ρ . We obtain the following three dimensionless groups:

$$\Pi_1 = \frac{\rho \omega R c}{\mu} \quad \Pi_2 = \frac{\omega R}{U_\infty} \quad \Pi_3 = \frac{c}{2R} \quad (1.1)$$

The first group Π_1 is the Reynolds number Re , which represents the ratio of inertial to viscous forces within the considered flow. This parameter is one of the most common dimensionless numbers in fluid mechanics and plays an essential role in predicting the transition from laminar to turbulent flow. Using the blade velocity $U_b = \omega R$ as the problem's characteristic velocity has a significant consequence in the Reynolds number definition. Studies investigating the wake of vertical-axis wind turbines may consider using the free stream velocity and the turbine diameter as characteristic length and velocity.

The second dimensionless group Π_2 is the ratio of the blade velocity to the incoming flow velocity, known as the tip-speed ratio. This parameter is crucial in the flow physics of wind turbine blades. Assuming that the blade starts its rotation facing the wind (figure 1.2), we can derive an expression for the variation of the blade's angle of attack α_{eff} with respect to the blade's azimuthal position θ and the tip-speed ratio λ from trigonometry:

$$\alpha_{\text{eff}}(\theta) = \tan^{-1} \left(\frac{\sin(\theta)}{\lambda + \cos(\theta)} \right) . \quad (1.2)$$

The effective flow velocity U_{eff} acting on the turbine blade can also be expressed relative to the incoming wind speed with respect to the blade's azimuthal position:

$$U_{\text{eff}}(\theta) = U_\infty \sqrt{1 + 2\lambda \cos(\theta) + \lambda^2} . \quad (1.3)$$

Note that equations (1.2) and (1.3) do not consider any wake-induced effects and are derived purely from the turbine's geometry and kinematics. Without this assumption, we should account for a third velocity component induced by the presence of vorticity surrounding the turbine blade. This induced velocity is proportional to the strength of the vorticity field. There is no straightforward way to estimate the magnitude and direction of the induced velocity since it requires knowledge of the vorticity field that develops in the surrounding of the wind turbine. In the scope of this introduction, we neglect the induced velocity and show the geometric evolution of the blade's effective angle of attack and blade velocity (figure 1.3). The tip-speed ratio governs the amplitude and skewness of the variation in effective flow conditions perceived by the wind turbine blade.

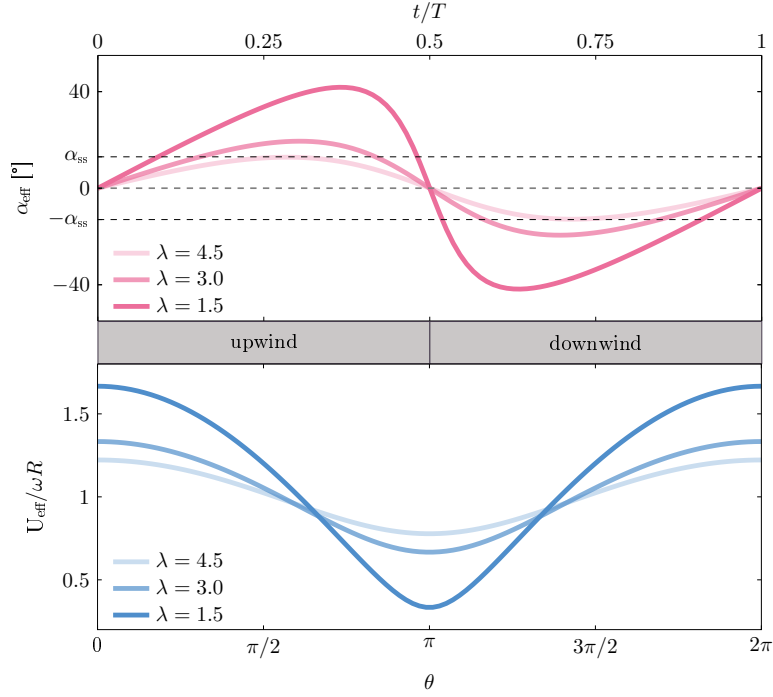


Figure 1.3: Temporal variation of the blade's effective angle of attack α_{eff} (equation (1.2)) and velocity U_{eff} (equation (1.3)) as a function of the blade's azimuthal position for three different tip-speed ratios $\lambda = \omega R/U_{\infty}$. The static stall angle α_{ss} of a NACA0018 operating at Reynolds number $\text{Re} = 50,000$ is shown for reference.

The third dimensionless group Π_3 is conventionally known as the chord-to-diameter ratio in the literature, so the turbine radius was multiplied by two in the denominator. Though this parameter is purely geometric, it is analogous to the blades' reduced frequency. High chord-to-diameter ratios lead to shorter rotation cycles in a non-dimensional form of time t . For a blade of chord length c operating in a steady free stream U_{∞} , non-dimensional time is defined as the convective time:

$$t^*(t) = \frac{U_{\infty} t}{c}. \quad (1.4)$$

A homologous parameter for a turbine blade is the unsteady convective time, commonly used for wings operating in unsteady free stream conditions. The unsteady convective time is defined as:

$$t_c(t) = \int_0^t U_{\text{eff}} / c dt. \quad (1.5)$$

Substituting the expression for the effective flow velocity (equation (1.3)), the tip-speed ratio, and the chord-to-diameter ratio (equation (1.1)) into equation (1.5), we obtain an expression for the convective time in terms of the blade's azimuthal position:

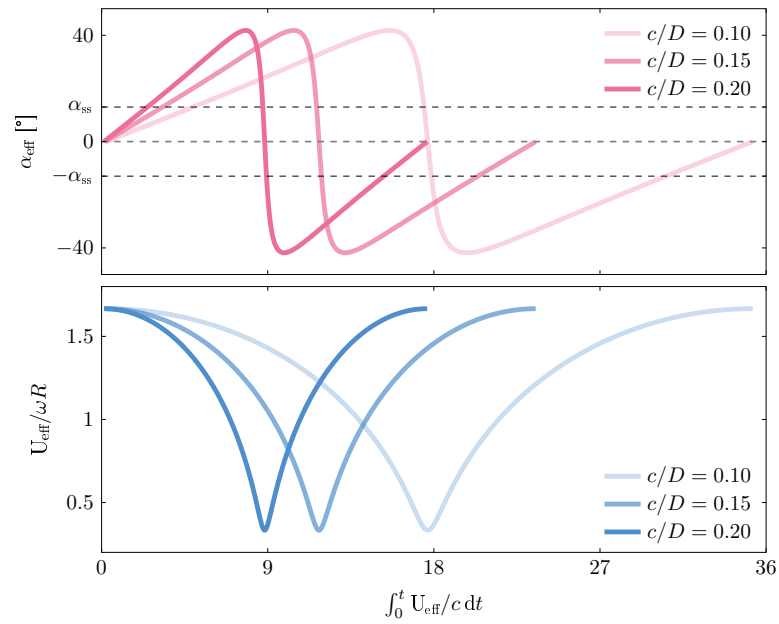


Figure 1.4: Temporal variation of the blade's effective angle of attack α_{eff} (equation (1.2)) and velocity U_{eff} (equation (1.3)) as a function of the blade's azimuthal position for three different chord-to-diameter ratios c/D . The static stall angle α_{ss} of a NACA0018 operating at Reynolds number $\text{Re} = 50,000$ is shown for reference.

$$t_c(\theta) = \frac{1}{\lambda c/R} \int_0^\theta \sqrt{1 + 2\lambda \cos(\theta) + \lambda^2} d\theta. \quad (1.6)$$

The convective time is proportional to the reciprocal of the chord-to-diameter ratio. We show the effective angle of attack and velocity against the convective time for three different chord-to-diameter ratios in figure 1.4. High chord-to-diameter ratios shorten the convective time available for flow development within a single rotation cycle of the turbine and increase the likelihood of blade-wake interaction, even for a single-bladed wind turbine interacting with its own wake in the downwind half of its rotation.

For low tip-speed ratios, typically $\lambda < 3$, the turbine blade's effective angle of attack exceeds the static stall angle while undergoing a dynamic motion, which can lead to the occurrence of flow separation and dynamic stall.

1.2 Dynamic stall

Dynamic stall is a commonly encountered unsteady aerodynamic phenomenon. Literature regarding dynamic stall was initially motivated by helicopter rotor aerodynamics and flutter [15, 71, 99] and received renewed interest due to problems related to gust interactions [37, 53]. Dynamic stall occurs when the angle of attack of an airfoil exceeds its critical angle while undergoing a dynamic motion. Past this angle, the shear layer on the surface of the airfoil rolls up and forms a leading-edge vortex. The shear layer at the leading edge feeds vorticity into the vortex. The vortex grows to a critical size, generally the blade's chord length. The

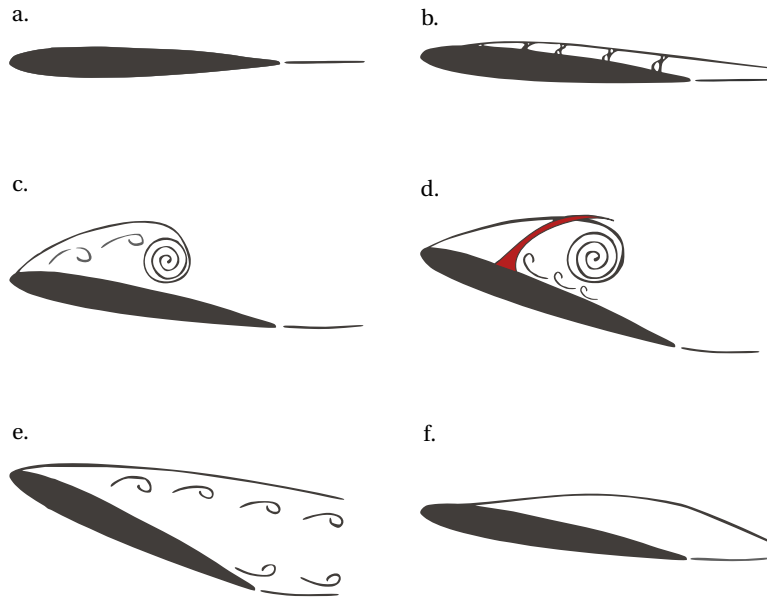


Figure 1.5: Schematic representation of the characteristic stages occurring during dynamic stall, modified from Carr, Mcalister, and Mccroskey [15] and Mulleners and Raffel [77]. The stages are named (a) attached flow, (b) flow reversal, (c) shear layer roll-up, (d) stall onset, (e) full stall, and (f) flow reattachment.

growing leading-edge vortex typically entrains counter-rotating vorticity generated at the airfoil’s trailing edge. The counter-rotating vorticity travels upstream on the blade’s surface until reaching the leading edge and interrupts the shear layer from feeding vorticity to the dynamic stall vortex. The vortex lifts off the blade and is shed into the wake, leaving a fully separated flow behind [15]. The flow stages experienced by a blade undergoing dynamic stall are shown in figure 1.5.

For pitching airfoils in a steady free stream, the main parameter governing flow unsteadiness related to the kinematics is the reduced pitch rate k defined as:

$$k = \frac{c\dot{\alpha}}{2U_{\infty}} \quad , \quad (1.7)$$

where c is the airfoil chord, $\dot{\alpha}$ is the pitch rate in radians per second, and U_{∞} is the free stream velocity. This parameter represents the ratio of the kinematic to the convective timescales of the flow. Pitching kinematics are roughly categorised as either static or dynamic depending on their reduced pitch rate. The lift response of a blade undergoing a static or dynamic pitching manoeuvres vastly differ.

The lift coefficient’s response to a change in angle of attack for a blade undergoing static and dynamic stall are compared in figure 1.6, reproduced with modifications from Mulleners and Raffel [77]. The dynamic motion was a high-frequency sinusoidal oscillation about the blade’s quarter-chord. For the static data, the blade is successively pitched by discrete angle of attack intervals and forces are recorded statically once the flow has reached steady-state. The dynamic and static lift coefficient responses to an increase in the angle of attack show an almost identical linear increase from the attached flow region (figure 1.6 (a)) up to the

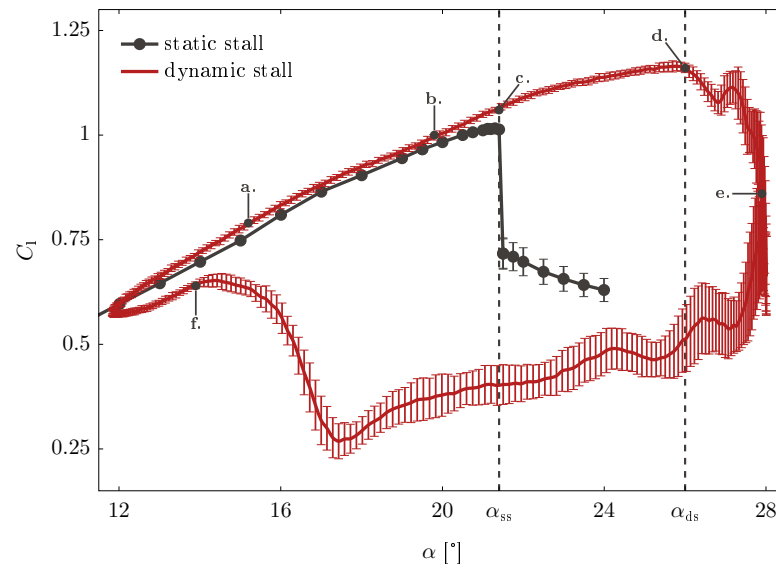


Figure 1.6: Phase-averaged lift coefficient as a function of angle of attack for a blade undergoing static and dynamic stall. The labelled nodes correspond to the stall stages depicted in figure 1.5. The error bars correspond to the standard deviation across multiple pitching cycles. The static stall angle of attack is noted as α_{ss} . Here, dynamic stall is assumed to occur at the lift coefficient maximum at an angle of attack noted as α_{ds} . This figure is reproduced with modification from Mulleners and Raffel [77].

moment when the blade exceeds its static stall angle α_{ss} . Past this moment, flow separation on the dynamically pitching blade is delayed to higher angles of attack, which leads to a lift overshoot compared to the static response (figure 1.6 (c-d)). The additional lift is attributed to the formation of a large-scale dynamic stall vortex [15, 69]. Although these attributes appear beneficial, dynamic stall is generally not considered desirable. The shedding of large-scale vortices is generally followed by a dramatic loss in lift production and highly unsteady loads (figure 1.6 (e-f.)) [72, 77]. The unsteady loads vary from cycle to cycle, as demonstrated by the increase in standard deviation across multiple pitching cycles in the post-stall region. The lift coefficient also displays a hysteretic behaviour during the pitch-down manoeuvre. The blade undergoing dynamic oscillations only recovers pre-stall lift performance after full flow reattachment (figure 1.6 (f)).

For vertical-axis wind turbines, large unsteady excursions of the effective angle of attack beyond its static stall angle α_{ss} and the varying inflow velocity can lead to dynamic stall [14, 40, 97]. Early experimental studies revealed that dynamic stall occurs for tip-speed ratio $\lambda < 4$ for a chord-to-diameter ratio $c/D = 0.1$ and transitions from light stall to deep stall as the tip-speed ratio decreases [58].

Among the first flow measurements of dynamic stall on vertical-axis wind turbines were performed by Simão Ferreira et al. [97] (figure 1.7). In the upwind half of the rotation, the effective angle of attack exceeds the blade's critical stall angle and stall vortices form on the inboard side of the blade. When these vortices shed, they convect downstream and interact with the blade for an extended period of time throughout the downwind half of the blade's rotation ($\pi \leq \theta < 2\pi$) [23, 96, 97]. Blade-vortex interaction and post-stall vortex shedding cause highly transient and heavy load fluctuations that jeopardise the turbine's structural integrity and

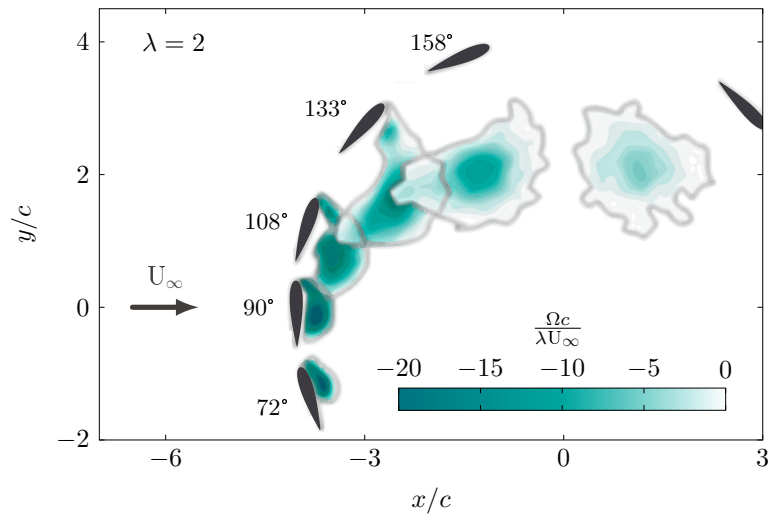


Figure 1.7: Negative vorticity field around a vertical-axis wind turbine blade undergoing dynamic stall. The turbine is operating at tip-speed ratio $\lambda = 2$, chord-to-diameter 0.125, and Reynolds number $Re = 5 \times 10^5$. This figure is reproduced with modification from Simão Ferreira et al. [97].

often lead to premature fatigue failure [24, 30, 79]. Low tip-speed ratios are associated with high variations in the angle of attack, dynamic stall, and extended periods of time during which the flow is massively separated, compared to higher tip-speed ratio operation.

For pitching wings in a steady free stream, the temporal occurrence and landmark stages characterising dynamic stall on two-dimensional pitching airfoils in a steady free-stream flow are well documented [15, 25, 77], and their load responses are well modelled [5, 44, 63]. For a rotating wind turbine blade, the occurrence of dynamic stall is affected by the circularity of the blade's path in several ways. The unsteady aerodynamics of wind turbine blades challenge our conventional understanding of dynamic stall.

1.3 Rotational effects

Following a circular path affects the blade's aerodynamics on three aspects: blade-wake interactions, flow curvature and wake deflection. Turbine blades cross the same stream tube twice, leading to repeated blade-wake interactions even for a single-blade configuration [40, 80]. In the occurrence of dynamic stall, once the vortex lifts off from a wind turbine blade, it convects downstream along the blade's path rather than shedding into the blade's wake. The flow topology is dominated by the extended presence of a dissipating dynamic stall vortex at the overlap between the upwind and downwind halves of the blade rotation around $t/T = 0.5$ when the effective velocity is at its lowest (figure 1.7).

The flow curvature also influence the effective flow acting on a vertical-axis wind turbine blade. Using conformal mapping techniques, the turbine blade may be transformed to an equivalent virtual blade in a rectilinear flow to account for flow curvature [9, 74]. This transformation yields a cambered airfoil that preserves local velocities and angles of attack. The transformed airfoil in the rectilinear flow exhibits the aerodynamic behavior of the geometric airfoil in

1.4 Influence of governing parameters on turbine power performance

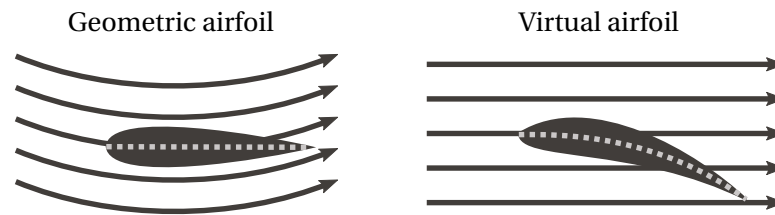


Figure 1.8: Schematic illustration of the conformal transformation from a symmetric airfoil in a curved flow to a cambered airfoil in a rectilinear flow. This figure is reproduced from Migliore, Wolfe, and Fanucci [74].

rotation (figure 1.8). On the geometric airfoil, the effective angle of attack and velocity varies along the blade surface, challenging the usual description of effective flow conditions given by equations (1.2) and (1.3). Lastly, the circulation related to the presence of a rotating turbine in the free stream deflects the wake away from the direction parallel to the free stream. Both rotational effects and dynamic stall play a central role in the power performance of vertical-axis wind turbines.

1.4 Influence of governing parameters on turbine power performance

The power performance of vertical-axis wind turbine blades varies greatly across operating conditions, which are parametrised by the Reynolds number, the tip-speed ratio λ and the chord-to-diameter ratio (equation (1.1)).

1.4.1 Reynolds number influence

The power performance of vertical-axis wind turbines is highly sensitive to flow separation. Flow separation is inherently a viscous phenomenon. Consider the flow around a curved, lift-generating surface. For an inviscid fluid, the flow would accelerate, and the pressure would drop as the flow travels to the curvature climax, followed by deceleration and return to the upstream pressure and velocity as the flow leaves the surface. It is a balanced and reversible exchange between kinetic energy (velocity) and potential energy (pressure). In an actual viscous flow, some kinetic energy is dissipated in the viscous shear layer near the surface. The dissipation rate is more significant for large curvatures. When the flow is expected to return kinetic energy to potential energy downstream of the surface climax, the loss in kinetic energy yields an adverse pressure gradient. The adverse pressure gradient ultimately leads to flow separation.

We expect the Reynolds number to play an important role in the development of separated flow structures. This parameter quantifies the importance of viscosity in the transport and dissipation of kinetic energy transported by the flow. Though the Reynolds number plays a crucial role in laminar or transitional flows, investigations on the influence of the Reynolds number on vortex-dominated flows do not report a significant impact of the variation of this parameter for moderate to high Reynolds number [15]. An increase in Reynolds number will delay the occurrence of flow reversal and encourage flow reattachment. The sequence of characteristic events in dynamic stall, including shear layer roll-up, stall onset, and vortex

shedding, remains the same across Reynolds numbers [15]. The timescales of these events are also independent of Reynolds number [5].

Vertical-axis wind turbine experiments at full dynamic similarity were performed by Miller et al. [75]. The power coefficient was measured for a geometrically scaled turbine model operating at tip-speed ratios $\lambda \in [0.9 - 1.6]$ and chord-based Reynolds numbers $Re_c \in [5 \times 10^5 - 5 \times 10^6]$. Turbine performance improves for Reynolds number increasing up to $Re = 1.5 \times 10^6$, after which the power performance is independent of the Reynolds number. This trend is self-similar across all tested tip-speed ratios. The power performance improvement of turbines at low tip-speed ratios with increasing Reynolds number is arguably due to the reduced role of flow separation and dynamic stall.

Flow structures forming around wind turbines are not sensitive to a change in Reynolds number. The turbine's wake maintains the same structure for a scaled-down, three-bladed wind turbine model operating at $Re = [6 \times 10^4, 1.2 \times 10^5, 1.8 \times 10^5]$ in a study by Parker and Leftwich [84]. Dynamic stall vortex timing and topology are not sensitive to a change in Reynolds number [14, 97]. The variation of the power coefficient with the tip-speed ratio features the same profile and conserves the same maximum across tip-speed ratios [7]. Therefore, it is pertinent to investigate blade-level wind turbine flow physics at intermediate Reynolds numbers $Re \mathcal{O}(10^5)$.

1.4.2 Chord-to-diameter influence

The chord-to-diameter ratio governs the frequency of the variation in effective flow conditions perceived by the blade (figure 1.4). For unit-level investigations, this ratio is generally multiplied by the number of blades to yield the turbine solidity σ . Solidity strongly influences the power coefficient profile for changing tip-speed ratios. Decreasing turbine solidity typically reduces the peak power coefficient achieved at the optimal tip-speed ratio but also widens the range of high-performing tip-speed ratios [26, 52] (figure 1.9).

Low turbine solidities flatten the turbine's power curve across tip-speed ratios and reach their optimal power coefficients at high tip-speed ratios. Low tip-speed ratios are related to the occurrence of dynamic stall. For low solidity and chord-to-diameter ratios, the blades spend a prohibitively long period of time beyond the blade's static stall angle (figure 1.4), extending the timespan where the flow is fully separated from the blade's surface. Post-stall conditions are detrimental to turbine performance. Low turbine solidities are undesirable as they suffer most from flow separation.

High turbine solidities are characterised by a low standard deviation and high maximum power coefficients. The low spread of high-performing tip-speed ratios is arguably related to rotational effects affecting the turbine blades (section 1.3). Increasing turbine solidity amplifies rotational effects, particularly the likelihood of blade-wake interactions. At the optimal tip-speed ratio $\lambda \approx 3$, the turbine blade will shed vorticity at the right time intervals to avoid excessive blade-wake interactions. Turbine blades operating at tip-speed ratios below 3 will shed large-scale vortices that interact with all blades and cause a loss in efficiency. Turbine

1.4 Influence of governing parameters on turbine power performance

blades operating at tip-speed ratios above 3 will suffer from extended interaction with the wake of the other blades.

Intermediate solidities around $\sigma = 0.2$ offer a desirable compromise between operational versatility and resilience to blade-wake interactions (figure 1.4). Although turbine power performance is greatly influenced by the chord-to-diameter ratio, the development of dynamic stall is independent of this parameter within the design range of actual wind turbines ($c/D \in [0.1-0.2]$). Temporal scaling of the dynamic stall vortex strength was investigated by Buchner et al. [14]. They performed spatially resolved stereoscopic particle-image velocimetry for a scaled wind turbine operating at tip-speed ratio $\lambda \in [1-5]$, Reynolds number $Re \in [50\,000-140\,000]$ and chord-to-diameter ratio $c/D \in [0.1-0.2]$. The evolution of the vortex strengths for different chord-to-diameter ratios collapses when presented as a function of the convective time post-stall (equation (1.6)). This collapse suggests that vortex formation is self-similar across reduced frequencies and that vortex strength is governed only by the tip-speed ratio. Actual wind turbine blades undergo sufficiently high reduced frequencies that the timescales of dynamic stall are no longer a function of reduced frequency. The relationship between stall timescales and reduced frequency are further discussed in chapter 2.

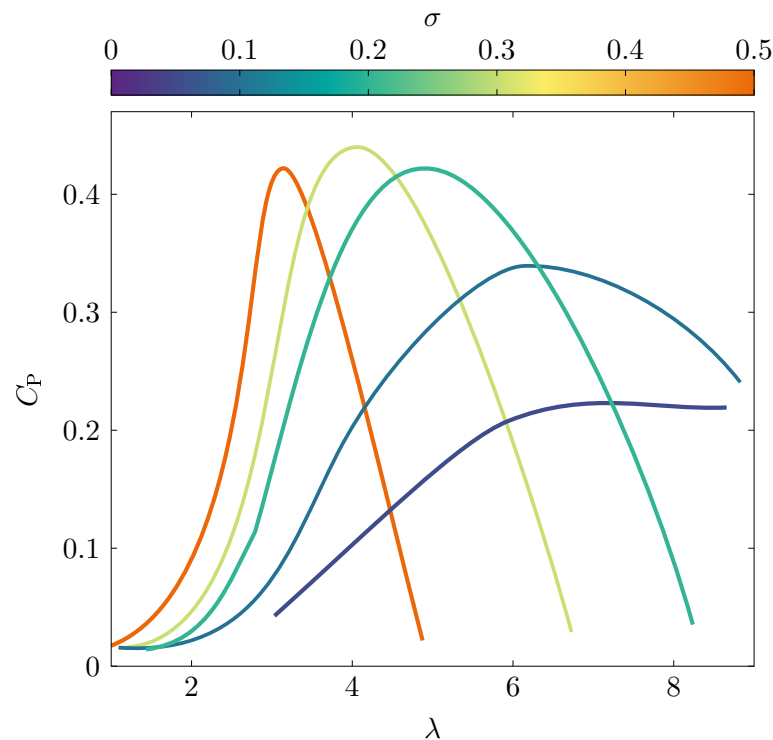


Figure 1.9: Parametric evolution of turbine power coefficient against tip-speed ratio λ for various turbine solidities σ . This figure is reproduced with modification from Jamieson [52].

1.4.3 Tip-speed ratio influence

The tip-speed ratio plays a crucial role in predicting wind turbine efficiency (figure 1.9). Wind turbine blades operating at high tip-speed ratios do not perceive sufficient variations in the angle of attack to yield significant power production (figure 1.3). High tip-speed ratios also promote interactions between the different turbine blades and their wakes. Low tip-speed ratios are characterised by the occurrence of dynamic stall, previously discussed in section 1.2. Decreasing the tip-speed ratio yield larger and stronger dynamic stall vortices [40, 97]. The shedding of these large coherent structures is related to a loss in torque production and heavy post-stall load fluctuations, which can lead to turbine failure [16, 24]. Unsteady wind conditions can lead to a sudden drop or surge in tip-speed ratio. Active flow control is a desirable strategy to ensure vertical-axis wind turbines maintain high power performance and enjoy safe operation across tip-speed ratios.

1.5 Blade pitch control

The development of vertical-axis wind turbines suffered from complex unsteady aerodynamics. Particularly at low tip-speed ratios, wind turbines undergo flow separation and potentially dynamic stall. Large-scale dynamic stall vortices threaten the structural integrity of wind turbines. Avian species have learned to harness the lift-enhancing properties of leading-edge vortices rather than avoiding their formation [32, 34]. Bio-inspired flow control strategies can lead to significant performance improvements in wings interacting with vortical structures, such as flapping wings [41] and oscillating airfoils [55]. Controlled vortex formation can help wind turbines maintain high efficiency and structural integrity across tip-speed ratios. Successful control strategies will most likely keep vortical structures attached to the blade's leading edge for extended periods of time and encourage vortex shedding halfway through the blade's rotation, avoiding prolonged blade-vortex interactions.

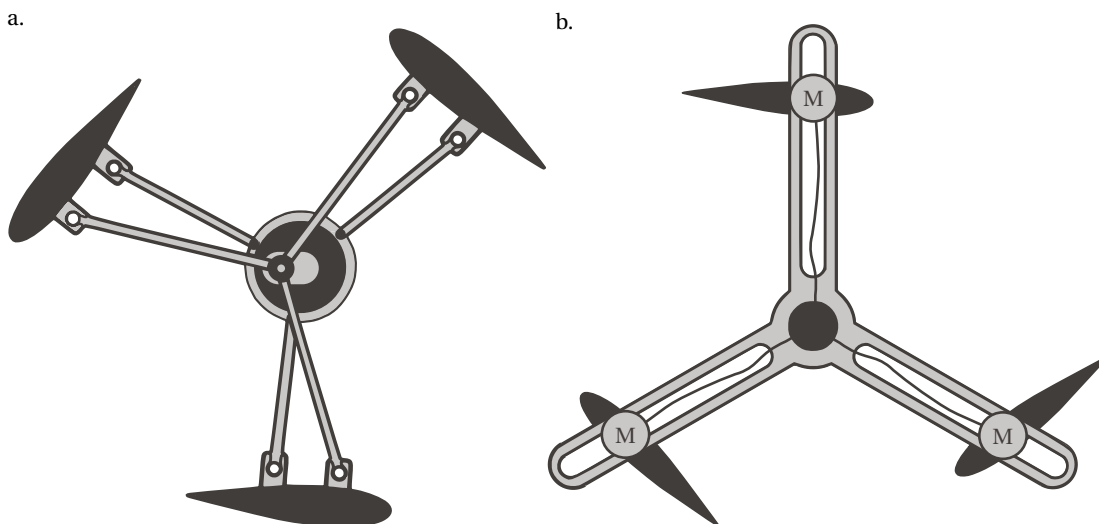


Figure 1.10: Schematic drawings of synchronous blade pitching mechanism inspired by Kiwata et al. [57] (a), and an active blade pitching mechanism (b).

Flow control strategies for vertical-axis wind turbines aim at influencing the angle of attack experienced by the blade. This influence is achieved by altering the blade kinematics or implementing surface flow control devices, such as plasma actuators or suction slots [88]. Blade surface flow control demonstrated the ability to delay flow separation and influence vortex formation, but their cost and implementation challenge the commercial viability of these actuators.

Here, we focus on changing the blade kinematics by actuating the blade's pitch angle α_{pitch} , or the angle between the blade's chord and the tangent line to the blade's path (figure 1.2). Changing the blade's pitch angle can be done statically, synchronously or dynamically (figure 1.10). A simple 2° static angle of attack offset on the wind turbine blade yields a 6.6 % increase in power coefficient at a tip-speed ratio of 4 [87].

Synchronous blade pitching involves a mechanism, typically a crankshaft, that will change the blade's pitch angle throughout the blade's rotation. At a given tip-speed ratio, synchronous blade pitching can boost the power coefficient by over 50 %, enabling vertical-axis wind turbines to reach power coefficients up to 0.38 [33]. The mechanical complexity of synchronous blade pitching limits its commercial application. The pitching kinematics are also limited by the mechanism and do not adapt to changing wind conditions, potentially becoming detrimental to turbine operation at off-design tip-speed ratios. Dynamical blade pitching involves a direct blade-motor drive, allowing complete independence between the blade's pitch angle and the turbine's rotation. This added versatility makes dynamic blade pitching the optimal solution to adapt to rapidly changing weather conditions while maintaining a constant angular velocity and high power coefficient. Performance stability is desirable for renewable energy systems aspiring to integrate the electrical grid.

Few studies have investigated dynamic blade pitching for vertical-axis wind turbines. A low-order model of turbine blade performance was coupled with a genetic algorithm optimiser to maximise power performance, demonstrating a 30 % increase in the annual energy production [82]. A numerical optimisation based on computational fluid dynamics (CFD) simulations achieved power coefficients of 0.64 and 0.72 at tip-speed ratios 4.5 and 3.4 [65]. CFD turbulence models that are computationally affordable enough to simulate sufficient conditions to perform optimization do not accurately capture the development of turbulent separated boundary layers. Both low-order models and CFD turbulence models struggle to resolve the flow physics of highly separated flows, such as those encountered by wind turbines operating at low tip-speed ratios. In the final part of this thesis, we experimentally investigate the potential of dynamic blade pitching to enhance the power performance of vertical-axis wind turbines and reduce the unsteady load fluctuations related to flow separation.

THE DYNAMICS OF STATIC STALL

Vertical-axis wind turbine blades undergo complex and unsteady kinematics. The kinematics combine a continuous variation in the angle of attack and incoming flow velocity while following a curved path. The combination of pitching, surging and rotation, and higher order term derivative of these, likely affect the flow structure development and their timescales. Fundamental work on the role of kinematic in the development of aerodynamic loads and flow structures has been an active field of research since the first half of the twentieth century (chapter 1). The distinctive line between *static* and *dynamic* motions remains undefined. This chapter presents findings on the influence of the reduced pitch rate for extremely slow motions. The objective is to characterise the behaviour of stall timescales for a wide range of pitch rates in preparation for analysing wind turbine data. Incidentally, this study also kept the author busy while deprived of his laboratory during the long months at the beginning of the coronavirus pandemic.

The work presented here was published in the Journal of Fluids and Structures [60].

CHAPTER HIGHLIGHTS

- ⊙ Pitching can be considered slow for reduced frequencies $k \approx 1 \times 10^{-4}$, below which stall timescales are no longer affected by a further reduction in frequency.
- ⊙ A universal power law describing the evolution of the stall delay against reduced frequency. This law was validated for three wings undergoing different kinematics and operating at $Re \in [75'000 - 920'000]$ and $k \in [1 \times 10^{-4} - 0.14]$.
- ⊙ For reduced frequencies greater than $k \approx 0.04$ the stall delay becomes independent from pitch rate and tends to optimal vortex formation, around 4 convective times.

2.1 Introduction

Flow separation and stall play a central role in the design of lifting surfaces for a wide range of applications such as rotary and fixed wing aircraft, wind turbines, etc. [64, 70, 73]. Stall is a commonly encountered, mostly undesired, condition that occurs when the angle of attack of an airfoil exceeds a critical angle. We typically distinguish between static and dynamic stall based on the rate of change of the airfoil's angle of attack [35]. The distinction is rather qualitative, as there is no universal criterion to assess whether a motion can be considered either static or dynamic. The denotation of static stall is highly misleading for two reasons: (i) an airfoil can not stall unless it moves past its critical stall angle and (ii) the flow and force development during the transition from an attached to a separated flow state are inherently unsteady. The temporal evolution of aerodynamic loads acting on an airfoil undergoing stall at extremely low pitch rate is often overlooked, as most attention is devoted to dynamic motions.

The main parameter governing flow unsteadiness related to the kinematics of a pitching airfoil is the reduced pitch rate k defined as:

$$k = \frac{c\dot{\alpha}}{2U_{\infty}} \quad , \quad (2.1)$$

where c is the airfoil chord, $\dot{\alpha}$ is the pitch rate, and U_{∞} is the free stream velocity. For high enough pitch rates, stall onset is delayed to an angle of attack beyond the critical stall angle [15, 69]. The angular delay of flow separation is considered one of the classical hallmarks of dynamic stall [71]. From a timing perspective however, high pitch rates promote flow separation and reduce the blade's reaction time relative to the static case [56, 78].

The reaction time is a measure of the time the blade takes to stall after its angle of attack exceeds the critical stall angle. This timespan follows a power law decay for increasing reduced pitch rates, reaching a plateau for reduced pitch rates above 0.04 [27, 32]. The minimum value for reaction time is attributed to the vortex formation time. The dynamic stall vortex requires a certain convective time to form before massive flow separation can occur, typically between 3 and 5 convective times for pitching airfoils [20, 42]. For extremely low pitch rate values, blade kinematics cease to promote flow separation and the reaction time is expected to reach a maximum value which is not yet well defined. The key differences in the temporal evolution of static and dynamic aerodynamic loads remain to be formulated, and arguably static stall should be regarded as a general case of stall for extremely low values of the pitch rate.

Conventionally, we consider stall to be static when the airfoil's kinematics are slow enough to avoid delaying full flow detachment past the airfoil's critical stall angle. This angle is measured by making sub-degree angle of attack increments, allowing the flow around the airfoil to fully develop before further motion is imposed. The last angular position before a loss in lift is observed is considered the critical stall angle. This value plays a crucial role in characterising the airfoil's performance for dynamic motions and is a key parameter in semi-empirical models for dynamic stall [63, 95]. Guidelines that characterise the relationship between reduced pitch rate and the temporal occurrence of stall are relevant to accurately determine the critical stall angle of a given airfoil.

In this chapter, we experimentally investigate the transient development of aerodynamic forces during what is typically considered as conventional static stall. We approach the static stall limit in two different ways: by increasing the angle of attack in small discrete steps and by slowly but continuously increasing the angle of attack. The systematic acceleration and deceleration related to the stepwise increase of the angle of attack is more likely to disturb the flow than a continuous, extremely slow ramp-up. The time resolved lift response to the two types of quasi-steady motions is compared. Specific focus is directed towards the identification of successive stages in the flow development and the statistical analysis of the timescales associated with the different flow development stages. We quantify the reaction delay between the time when the blade exceeds its static stall angle and the occurrence of stall, determine the limiting values for extremely low and high pitch rates, and compare the results with the stall delays measured for various dynamic motions. The main objective is to characterise the influence of the reduced pitch rate on the characteristic timescales of an airfoil undergoing stall, and identify qualitative properties that help qualify a motion to be static or dynamic.

2.2 Experimental setup

A NACA0018 profile is vertically suspended in a recirculating water channel with fully-transparent acrylic windows and a test section with dimensions $0.6 \text{ m} \times 0.6 \text{ m} \times 3 \text{ m}$, illustrated in figure 2.1. The airfoil's chord is $c = 0.15 \text{ m}$ and the span is close to the height of the test section: $S = 0.58 \text{ m}$. The bottom of the profile is flush with the bottom transparent wall, and a splitter plate is mounted on the top to reduce free surface effects on the airfoil. The blade was 3D printed as a single piece using PLA, sanded with ultra-fine 1000-grit paper, and covered with a thin layer of epoxy resin to rigidify the blade and ensure it is watertight. The rotation happens about the quarter-chord axis, and it is driven by a 10 mm square-sectioned stainless steel shaft that is tightly inserted through the blade's span. The incoming flow is set at $U_\infty = 0.50 \text{ m/s}$, resulting in a Reynolds number of $Re = 7.5 \times 10^5$.

Forces are measured with a six degrees of freedom load cell (ATI Nano 25) placed at the interface between the shaft of the airfoil and the motor shaft. Force data were recorded with a sampling frequency of 1000 Hz, a sensing range of 125 N and a resolution of 0.02 N. Output from the load cell was transmitted to a computer using a data acquisition system (National Instruments). Buoyancy forces and load cell factory offset were measured in the water channel without flow for the whole range of angles of attack investigated. These forces were subtracted from the force data to obtain the aerodynamic loads. The force data was filtered using a second-order low-pass filter with the cut-off frequency of 30 Hz. This frequency is multiple orders of magnitude larger than the pitching frequency and 48 times larger than the expected post-stall vortex shedding frequency based on a chord-based Strouhal number of 0.2 [63].

Two quasi-steady manoeuvres that lead to the occurrence of what can be considered conventional static stall are investigated: a slow continuous ramp-up motion and a step-wise increase. For the first type of manoeuvre, we continuously increased the angle of attack from $\alpha = 8^\circ$ up to $\alpha = 18^\circ$ with a constant pitch rate of $0.05^\circ/\text{s}$, which corresponds to a reduced pitch rate

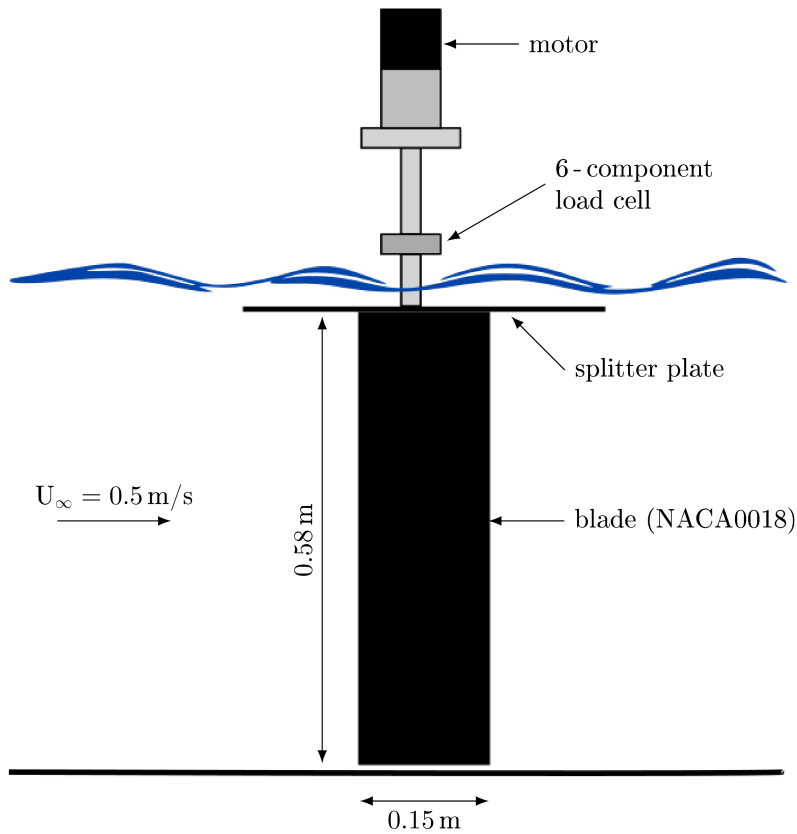


Figure 2.1: Schematic representation of the two-dimensional NACA0018 blade mounted vertically in a free surface recirculating water channel with a cross section of $0.6 \text{ m} \times 0.6 \text{ m}$.

of 1.3×10^{-4} . For the second type of manoeuvre, we performed a step-wise increase in the angle of attack from 14.2° to 14.8° within 0.04 convective times at $50^\circ/\text{s}$, which corresponds to a reduced pitch rate of $k = 1.3$. The airfoil was rotated around its quarter-chord axis using a stepper motor with a 1.8° step angle and $1 : 25$ planetary gearbox reduction, resulting in a position accuracy of 0.072° . The initial blade position was calibrated using a small angle of attack sweep between -5° and 5° to find the angle that resulted in zero net lift. The pitch rate for the continuous ramp-up motion was selected by progressively reducing the pitch rate until we systematically measured no significant lift overshoot at the onset of stall. Each motion was repeated for approximately 100 runs to allow for a statistical analysis of the transient aerodynamic load fluctuations occurring during stall development. For the step-wise, full flow reattachment was insured between runs by returning the blade to $\alpha = 8^\circ$ and pitching up to its starting position at $\alpha = 14.2^\circ$ with the same slow pitch rate used for the continuous ramp-up motion. The stall angle was determined based on the data collected with the ramp-up motion and found to be $\alpha_{ss} = 14.2^\circ$. This information was used to select the start angle for the step-wise motion.

Ramp-up motions with higher pitch rates ranging from $0.3^\circ/\text{s}$ to $53.3^\circ/\text{s}$, corresponding to reduced pitch rates ranging from 1×10^{-3} to 1.4×10^{-1} , were performed to obtain an overview of the influence of the pitch rate on the delay of stall with respect to the static case. For

all experiments, we recorded loads for 5 s or 16.7 convective times prior to the start of the manoeuvre, continuously during the manoeuvre, and for another 5 s after the manoeuvre was completed. The load cell recorded all three components of the force and the moments around all three spatial axes, but we will focus our analysis and discussion on the lift measurements. In most practical applications, the loss of lift due to a transition from attached to fully separated flow raises the most immediate concern. The characteristic timescales that we extract based on the lift response are the result of changes in the flow development which would equally affect other forces and moments, such as the drag or the pitching moment.

2.3 Results

The temporal evolution of the lift coefficient in response to the slow continuous ramp-up and the step manoeuvre are shown in figure 2.2. The timing is indicated in terms of convective time defined as $t_c = tU_\infty/c$, relative to $t_c = 0$ when the blade's angle of attack exceeds 14.2° . The value of 14.2° is considered the critical angle of attack above which the blade will always stall even if no further motion is imposed. Across the entire range of experiments conducted with this blade under the given flow conditions, 14.2° was the lower bound at which stall would consistently occur. Results are insensitive to the exact choice of critical angle, as moving it up or down one sub-degree would result in a homogeneous shift in timing for all experimental runs. A close-up view of the lift drop during stall for the continuous ramp-up in figure 2.2d facilitates the comparison between the continuous ramp-up and the step manoeuvre. Each line in figure 2.2b,d,f represents a different run. A single run is highlighted in black for both experiments to show the characteristics of the response.

In the continuous ramp-up experiment (figure 2.2a-d), the lift does not immediately drop once the blade exceeds the critical angle and remains at an approximately constant value for a certain time before dropping. The time delay between the moment at which the critical angle is exceeded and the moment at which the lift starts to drop differs for each run. We call this time delay the reaction delay and refer to the period covering the reaction delay as the holding stage. Although the blade's angle of attack can increase by as much as 0.6° during the holding stage for some runs, the blade does not produce additional circulation and the lift coefficient fluctuates steadily around 1 during this stage. For the highlighted run, the holding stage lasts about 33 convective times, followed by the drop stage where the lift coefficient falls from $C_L = 1.05$ to 0.6 in 9 convective times. A third characteristic time instant is identified as the first local lift minimum below the average post-stall level. At this point, the flow is considered to be in a fully developed stalled state. The fully developed post-stall stage is dominated by periodic load fluctuations due to characteristic bluff-body-like vortex-shedding [48, 49].

For the step-wise increase in angle of attack (figure 2.2e,f), the blade is static for the first 5 s or 16.7 convective times of the load recording during which the lift coefficient fluctuates around 1.05. The blade is then subjected to a step-wise increase of 0.6° beyond the critical angle of attack. The origin on the convective timescale marks again the time at which the blade exceeds the critical stall angle. The loads for all runs show a highly repeatable inertial response to the step manoeuvre characterised by lift fluctuations at 4 Hz over 5.5 convective

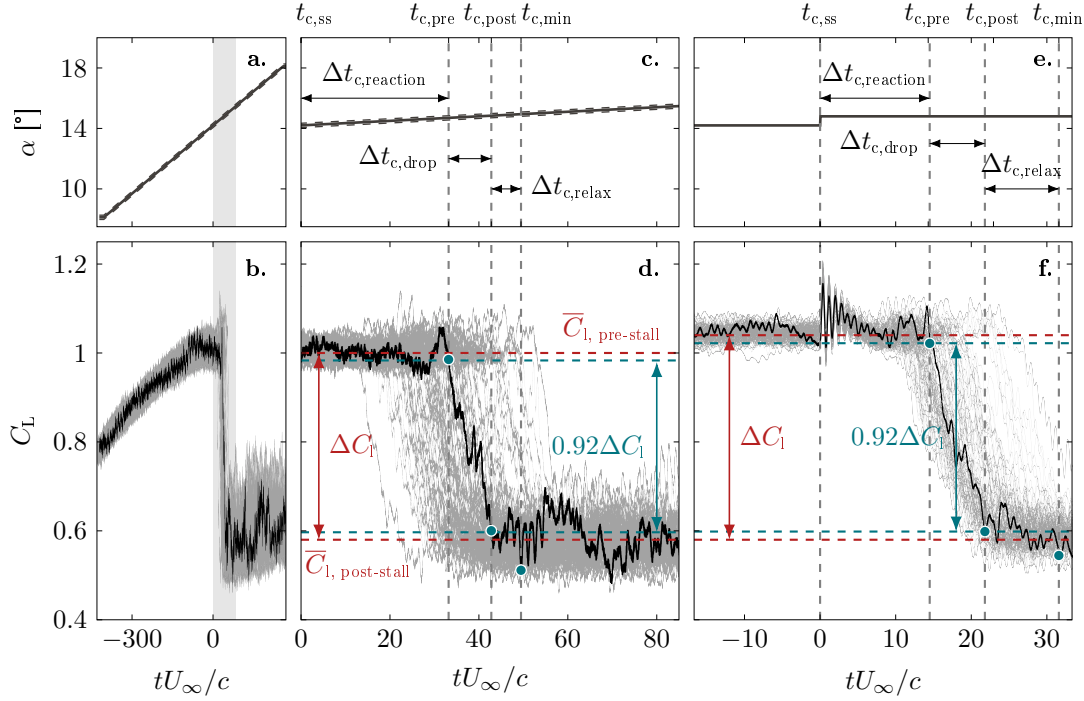


Figure 2.2: (a) Variation of the angle of attack during the continuous ramp-up manoeuvre. (b) The corresponding lift responses for 94 repetitions. (c,d) Close up views of the transient region corresponding to the shaded areas in the left plots. (e) Variation of the angle of attack during the step manoeuvre. (f) The lift response to the step-wise increase in the angle of attack for 100 repetitions. Convective time $tU_\infty/c = 0$ corresponds to the time when the airfoil's angle of attack exceeds the critical angle of 14.2° . The thicker black lines in the bottom row show the lift coefficient for a single run to highlight the characteristics of the individual responses. Pre-stall and post-stall reference levels are indicated by the red dashed lines. The green dashed lines indicate the upper and lower threshold values used to identify the timing of the stall stage. The start of the lift drop is $t_{c,pre}$ is defined as the time at which the lift has dropped more than 4 % of the total lift drop ΔC_l . The end of the lift drop is $t_{c,post}$ is defined as the time at which the lift has dropped more than 96 % of the total lift drop.

times. The fluctuations progressively decay and the lift returns to the same level as before the step manoeuvre. Similarly to the response to the continuous ramp-up motion, the lift does not collapse immediately after the angle is increased beyond the critical angle but remains at its pre-stall value for a time duration that varies for all runs. For the highlighted run, the lift coefficient has a last local peak above the pre-stall level around 14 convective times after the blade manoeuvre is conducted, followed by a drop from 1.05 to 0.6 in 9 convective times. About 32 convective time after the step manoeuvre, the flow reaches a post-stall stage dominated by large periodic load fluctuations.

For both manoeuvres, we distinguish three flow stages that characterise the transient flow development from fully attached to a fully stalled condition: a holding stage, a drop stage, and a relaxation stage. The time delays associated with these stages are indicated in figure 2.2 and are defined as follows:

1. the reaction delay defined as $\Delta t_{c,reaction} = t_{c,pre} - t_{c,ss}$, where $t_{c,pre}$ is the time when the lift drops below an upper threshold limit, and $t_{c,ss}$ is when the blade exceeds its critical stall angle of 14.2° ,

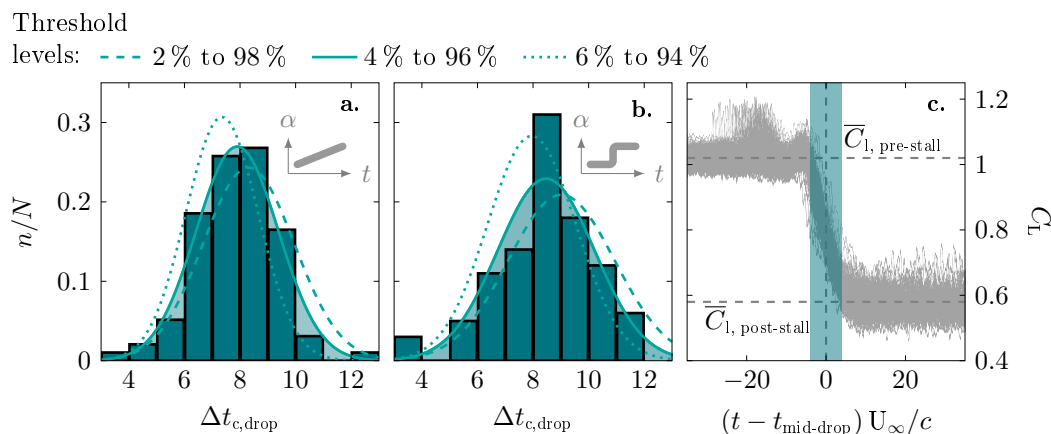


Figure 2.3: Drop time $\Delta t_{c,drop}$ occurrence histogram for all runs of (a) the slow continuous ramp-up and (b) the step manoeuvre based on threshold levels of 4 % and 96 % to identify the start and end of the lift drop. The solid line represents the fitted normal distribution corresponding to the histogram. The dashed and dotted lines indicate how the normal distributions shift when varying the threshold values. (c) Temporal evolution of the lift coefficient for all the runs of both the slow ramp-up and step-wise experiment shifted along the time axis with respect to the middle of the drop delay. The shaded area indicates the overall average drop delay of 8 convective times.

2. the drop time delay $\Delta t_{c,drop} = t_{c,\text{post}} - t_{c,\text{pre}}$ where $t_{c,\text{post}}$ is the time when the lift coefficient drops below a lower threshold limit,
3. the relaxation delay $\Delta t_{c,\text{relax}} = t_{c,\text{min}} - t_{c,\text{post}}$, where $t_{c,\text{min}}$ is the time when the lift reaches its first local post-stall minimum.

The upper and lower threshold levels are reference values that are determined with respect to the average pre-stall and post-stall limits and are fractions of total lift drop. Using thresholds at each boundary of the drop section, instead of using local extrema values, reduces the sensitivity of timescales to the large fluctuations occurring in the reaction and relaxation stages. Here, the upper threshold level was set 4 % of the total lift drop ΔC_l below the average pre-stall value $\bar{C}_{l,\text{pre-stall}}$. The lower threshold level was set 96 % of the total lift drop below the average pre-stall value $\bar{C}_{l,\text{pre-stall}}$ or 4 % of the total lift drop above the average post-stall value $\bar{C}_{l,\text{post-stall}}$. The percentages of the lift drop for the threshold limits were selected following an iterative procedure that aimed at maximising the drop stage length while avoiding outliers issuing from fluctuations at the edges of the drop stage. The drop stage analysis was completed following the IEEE standards of a negative-going transition [50]. A general idea of the influence of the choice of the threshold values on the results is provided by displaying results obtained with lower and higher threshold limits in the following figures.

The distributions of the extracted drop times $\Delta t_{c,drop}$ for both manoeuvres are compared in figure 2.3a,b. Both cases display a normal distribution centred around 8 convective times. The lift drop rate is constant for both experiments and yields a highly repeatable portion of the stall transient. The selected upper limit end lower limit threshold values represent a trade off between spanning the largest possible region for the drop stage, while limiting the spread of the reaction time occurrence histograms. Narrowing the threshold percentages (6 % to 94 %) reduces the spread but will artificial increase the repeatability of the reaction

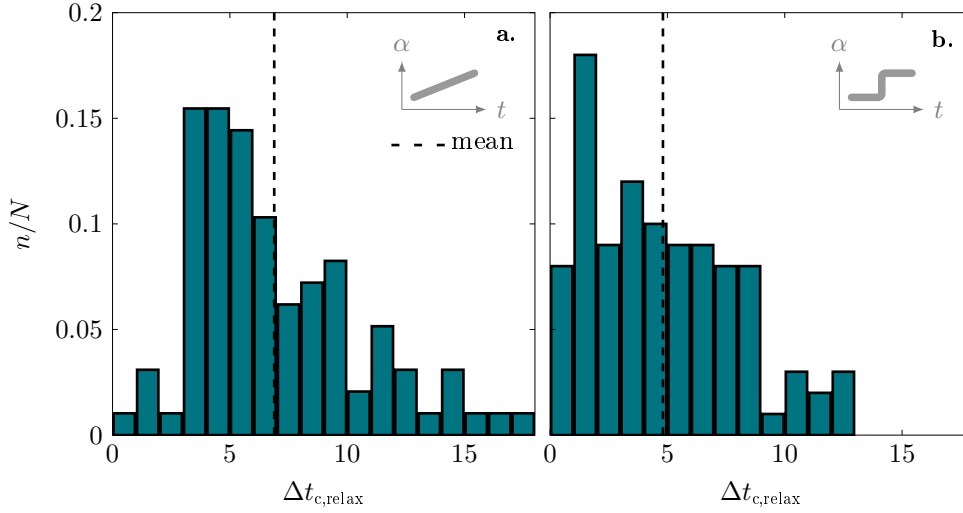


Figure 2.4: Relaxation delay $\Delta t_{c,relax}$ occurrence histogram for all runs of (a) the slow continuous ramp-up and (b) the step manoeuvre.

and relaxation stages by accounting for a greater portion of the repeatable drop stage in the neighbouring stages. Widening the threshold percentages (2 % to 98 %) increases the sensitivity of the drop stage duration to fluctuations occurring during the end of the reaction and the beginning of the relaxation stage, resulting in an increased standard deviation of the distribution. The numerical values depend slightly on the selected thresholds for the identification of the lift drop start and end, but the distributions of the drop times consistently show a normal distribution and the lift evolution during the drop stage is highly repeatable across all repetitions. The self-similarity of the lift response during the drop time is clearly visualised in figure 2.3 where all the lift responses for both cases are shown on top of each other shifted in time with respect to the middle of the drop time.

The distributions of the relaxation times $\Delta t_{c,relax}$ are compared for both manoeuvres in figure 2.4. The relaxation time $\Delta t_{c,relax}$ shows similar characteristics for both motions investigated: a skewed distribution with a mean value around 5. The lift coefficient has a standard deviation close to 10 % of its mean value in the post-stall stage. These significant fluctuations complicate the identification of the actual relaxation time, as several local minima could be considered as the first post-stall minimum. Further analysis of the influence of fluctuations on flow detachment will clarify the role that instabilities play in post-stall relaxation.

The distributions of the reaction times $\Delta t_{c,reaction}$ are compared for both manoeuvres in figure 2.5. The reaction time follows a standard normal distribution with an average of 32 convective times and a standard deviation of 8 convective times for the slow continuous ramp-up manoeuvre (figure 2.5a). Periodic peaks spaced by approximately 4 to 5 convective times suggest that pre-stall fluctuations cause periodically returning conditions that are favourable for the boundary layer to start separating. The reaction time for the step manoeuvre (figure 2.5b) follows a skewed normal distribution with a mean value of 14 convective times and a standard deviation of 4 convective times. The skewness, shorter time delay, and narrow spread relative to the continuous ramp up motion are attributed to the step angle of attack increase

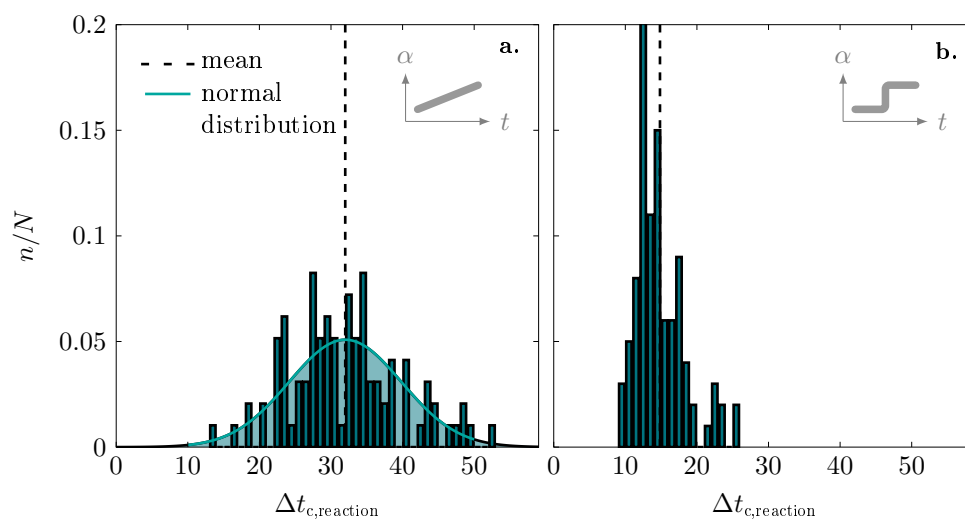


Figure 2.5: Reaction delay $\Delta t_{c, \text{reaction}}$ occurrence histogram for all runs of (a) the slow continuous ramp-up and (b) the step manoeuvre.

to beyond the static stall angle. The sudden and fast motion disturbs the surrounding flow, yielding increased load fluctuations compared to the slow continuous ramp-up manoeuvre. This unsteadiness promotes full flow detachment and creates a bias in the reaction time occurrence, increasing the repeatability between runs.

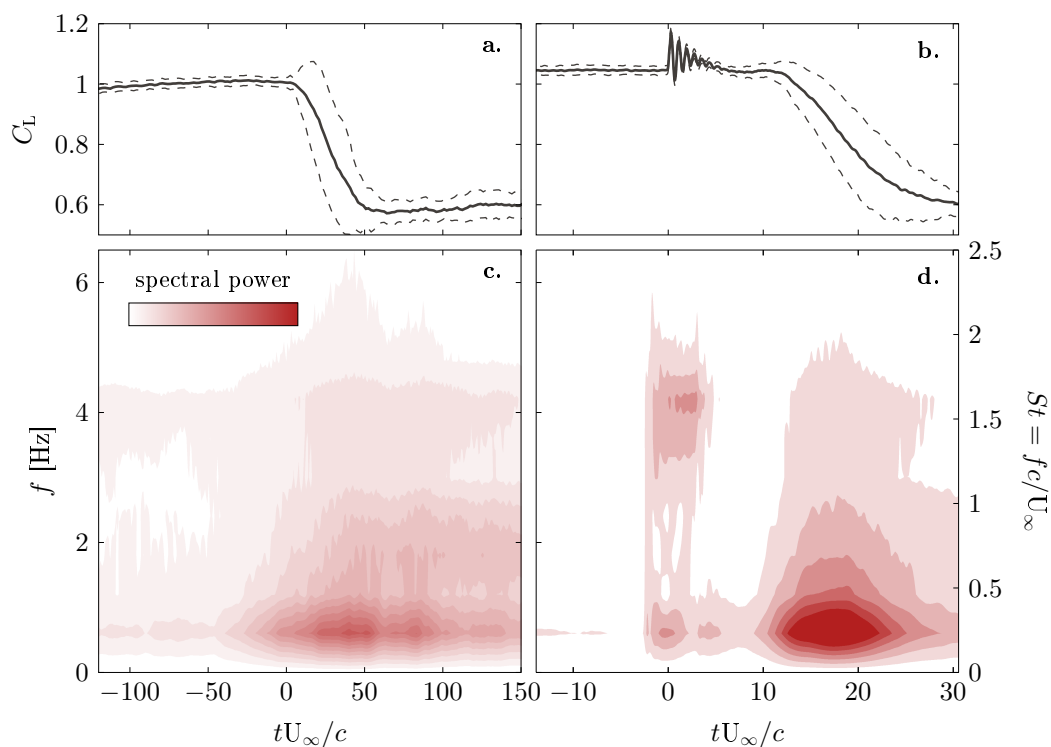


Figure 2.6: Ensemble-averaged temporal evolution of lift (top) and of the amplitude spectrum of lift (bottom) for (a,c) the transient portion of the slow continuous ramp-up manoeuvre and (b,d) the step manoeuvre.

To estimate the dominant frequencies of instabilities and assess their role in the occurrence of stall, we calculated a time-frequency plot for both manoeuvres. The dominating frequencies of the load fluctuations were quantified by completing a fast Fourier transform (FFT) on the load coefficient. The FFT was calculated using a sliding time window over the whole time domain for each individual repetition of both manoeuvres. The window width was set to 5.5 convective times, which corresponds to the time duration of the load transient that followed the step manoeuvre. The ensemble-averaged temporal evolution of the amplitude spectra are presented in figure 2.6 for both manoeuvres. The ensemble-averaged temporal evolution of lift was included to facilitate the comparison between time-scales, load fluctuations, and dominant frequencies. The timing is indicated in terms of convective time relative to $t_c = 0$ when the blade's angle of attack exceeds 14.2° . The blade undergoes load fluctuations with a frequency of 4.2 Hz immediately after the step around $t_c = 0$, as highlighted in figure 2.6b. This response to a single-point excitation on the blade apparatus is equivalent to a modal test. The highest energy peak in the amplitude spectrum, around 4.2 Hz, corresponds to the natural frequency of the system. Further peaks in the vicinity of 4.2 Hz are assumed to correspond to structural vibrations.

High energy peaks are observed around 0.65 Hz in the transient lift drop region at the time when lift peaks for both manoeuvres: near 32 convective times for the slow continuous ramp-up and near 18 convective times for the step manoeuvre. The expected vortex shedding frequency is calculated based on a Strouhal number $St = 0.20$ found experimentally for a NACA0018 operating at a Reynolds number of $Re = 7.5 \times 10^5$ [105]. The chord was chosen as characteristic length scale for vortex shedding. The projected chord length is more significant to characterise the interplay between vortices in a fully developed wake. The formation of stall vortices was found to occur much closer to the blade in the early stages of wake development. Additionally, our experiment is at a relatively low Reynolds number, so viscosity plays a more important role, reducing vortex formation length to near the blade [2, 76]. Following this argumentation, the expected vortex shedding frequency f_s is:

$$f_s = \frac{U_\infty St}{c} = 0.67 \text{ Hz} \quad . \quad (2.2)$$

This frequency corresponds to the dominating load fluctuation frequencies observed around 0.65 Hz in the stall transient and post-stall stages for both manoeuvres figure 2.6. A load fluctuation frequency of 0.65 Hz corresponds to temporally spaced lift peaks of about 5 convective times. This value also corresponds to the spread in the drop time histogram (figure 2.3). The temporal spacing between the peaks of the reaction time histogram for the slow continuous ramp-up manoeuvre (figure 2.5a) was also around around 5 convective times. The onset of stall occurs at periodically returning conditions after a randomly distributed number of cycles when the flow is no longer influenced by the blade kinematics. The amplitude peaks around 4.2 Hz in the stall transient and post-stall stages highlight structural vibrations. This analysis highlights the fact that flow unsteadiness plays a central role in the timing of the transient lift drop at stall. The frequency of load fluctuations explains the periodicity of the reaction time distribution and confirms the high repeatability of the drop time.

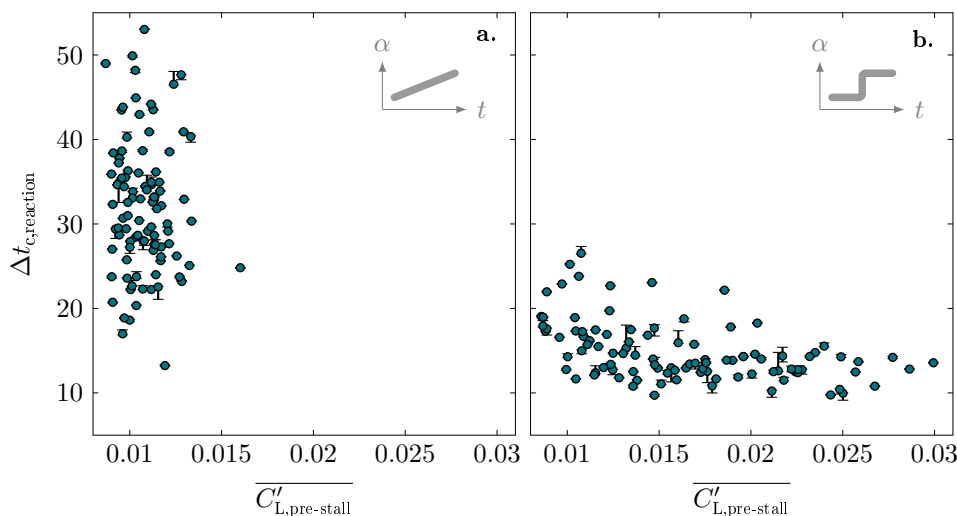


Figure 2.7: Reaction time $\Delta t_{c,\text{reaction}}$ against load fluctuations for all runs of (a) the slow continuous ramp-up manoeuvre and (b) the step manoeuvre. Error bars represent the difference between results obtained with threshold levels 6 % to 94 % and 2 % to 98 % to identify the start and end of the drop stage.

The reaction and relaxation delays varied significantly between individual runs for both manoeuvres. To assess the correlation between load fluctuation and the reaction and relaxation times, the magnitude of the load fluctuations was quantified. To obtain the magnitude of load fluctuations, the mean lift coefficient was computed on a sliding window with a 5 convective time width over the full time domain. The standard deviation was systematically calculated relative to the local mean $\overline{C_L}$. The lift fluctuation magnitude in the holding stage $\overline{C'_{L,\text{pre-stall}}}$ is computed as the average of the local standard deviations:

$$\overline{C'_{L,\text{pre-stall}}} = \frac{1}{N_{\text{pre-stall}}} \sum_{n=1}^N (C_{L,n} - \overline{C_{L,n}})^2 \quad (2.3)$$

where N is the number of points in the holding stage, $C_{L,n}$ is the local lift coefficient and $\overline{C_{L,n}}$ is the mean lift coefficient across the local window. The lift fluctuation magnitude during the drop stage $\overline{C'_{L,\text{drop}}}$ was calculated with an analogous expression, replacing $N_{\text{pre-stall}}$ by N_{drop} .

The reaction delay $\Delta t_{c,\text{reaction}}$ is presented against load fluctuations in the holding stage for both manoeuvres in figure 2.7. Load fluctuations for the slow continuous ramp-up manoeuvre are confined between 0.09 and 0.013, which is around 1 % of the local mean lift coefficient. There is no apparent correlation between the stall onset timing and the load fluctuation for the low levels of unsteadiness in the slow continuous ramp-up manoeuvre, suggesting that the motion is truly quasi-steady and does not influence the onset of flow detachment. The mean reaction time of 32 convective times observed for this manoeuvre can be considered to be a lower bound for the waiting time between subsequent angle of attack steps in static stall measurements. For the step manoeuvre, we observe a wider range of fluctuation levels in the holding stage, reaching up to 3 % of local mean lift coefficient (figure 2.7b). The reaction time linearly decays with load fluctuations, supporting the fact that flow unsteadiness promotes the onset of stall. The error bars represent the difference between results obtained with the

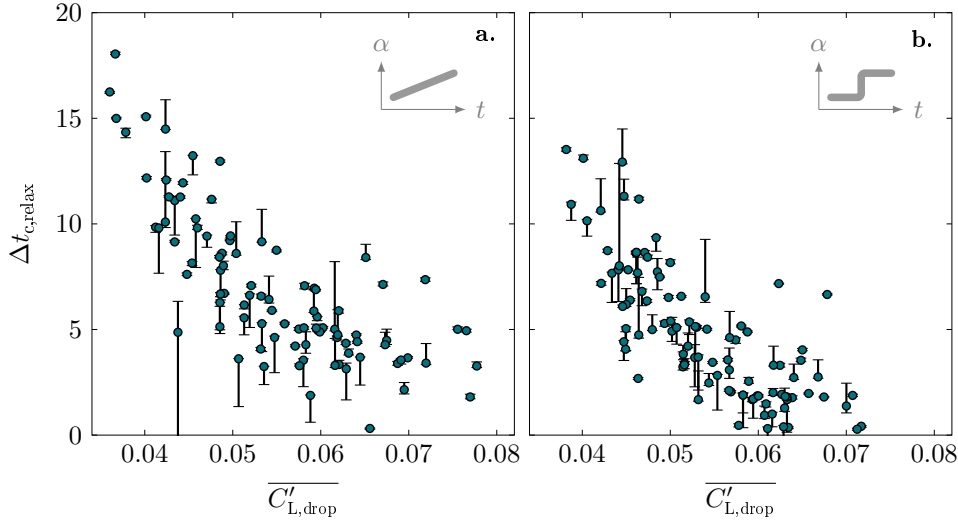


Figure 2.8: Relaxation time $\Delta t_{c,relax}$ against load fluctuations for all runs of (a) the slow continuous ramp-up manoeuvre and (b) the step manoeuvre. Error bars represent the difference between results obtained with threshold levels 6 % to 94 % and 2 % to 98 % to identify the start and end of the drop stage.

narrower (6 % to 94 %) and the wider threshold limits (2 % to 98 %) identifying the start and end of the drop stages. The error bars are small and indicate that these observations are not sensitive to the drop stage threshold selection for either kinematic.

The relaxation time $\Delta t_{c,relax}$ is compared to the load fluctuations in the drop stage in figure 2.8. Both experiments show similar fluctuation levels and a clear decreasing linear trend suggesting load fluctuations occurring during the lift drop promote full flow detachment. The decrease happens at the same rate for both manoeuvres. This suggests that the onset of vortex shedding is independent of kinematics for static motions. This timescale shows a much greater sensitivity to the drop stage threshold selection for some cases. The increased sensitivity is due to the greater fluctuations that occur in the post-stall regime compared to the pre-stall regime. The decay in relaxation time with increasing load fluctuations in the drop stage is nevertheless apparent.

The influence of pitch rate on the reaction time was investigated by comparing results of the slow continuous ramp-up manoeuvre with higher constant pitch rate manoeuvres. Data was collected for reduced pitch rates ranging from 1×10^{-4} to 0.14 with 5 repetitions for each pitch rate. We systematically compute the reaction time $\Delta t_{c,reaction} = t_{c,pre} - t_{c,ss}$, where $t_{c,pre}$ is the time where the lift coefficient starts to drop and $t_{c,ss}$ is when the blade exceeds its critical stall angle of 14.2° . The average reaction time calculated over the 5 repetitions is presented against reduced pitch rate in figure 2.9. The error bars show the standard deviation and indicate the spread or the width of the distribution of the measured reaction times at a given reduced pitch rate.

The stall delay or reaction time decreases with increasing pitch rate following a power law decrease. The additional unsteadiness added to the flow at higher pitch rates promotes flow detachment and the onset of stall. The reaction time decreases rapidly for reduced pitch rates

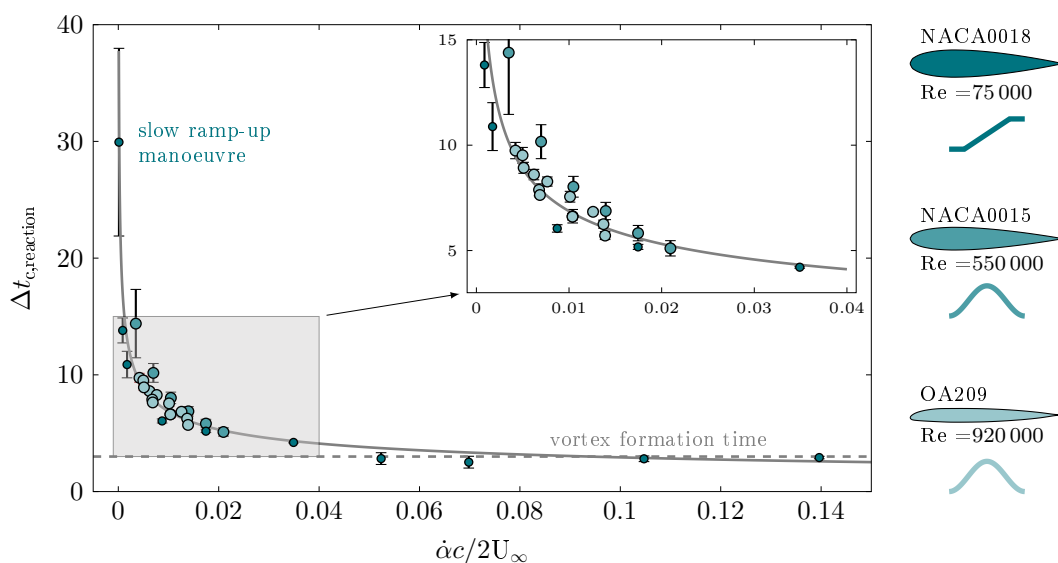


Figure 2.9: Average reaction time delay $\Delta t_{c,\text{reaction}}$ as a function of reduced pitch rate for three different airfoils. Results from the continuous ramp-up motion of our NACA0018 are compared with previous results from a sinusoidally pitching OA209 airfoil at $\text{Re}=9.2 \times 10^5$ [78] and a sinusoidally pitching NACA0015 airfoil at $\text{Re}=9.2 \times 10^5$ [46].

below 0.01 and reaches a plateau at 4 convective times for reduced pitch rates above 0.04. This lower limit is of the order of the vortex formation time of the dynamic stall vortex, which is a classical hallmark of the transition from an attached to a massively separated flow [32, 77]. The plateau represents a minimum timescale the blade requires to form a leading edge vortex and reach a fully separated flow condition [20]. Stall onset and vortex formation are characterised by the reaction time and it is the main difference used to distinguish static from dynamic stall [32, 78]. The coherent transition between the lowest and higher pitch rates support our hypothesis that the static and dynamic stall responses are phenomenologically the same and their timescales vary continuously as a function of the pitch rate of the underlying motion kinematics.

The standard deviation also decreases rapidly with increasing reduced pitch rate. The airfoil kinematics play a lesser role in the flow development at extremely low pitch rates and no longer promote the occurrence of stall, resulting in an increasingly random and wide distribution of the reaction time delays. The reaction time histogram for the lowest pitch rate (figure 2.5) followed a perfect normal distribution, suggesting this motion can be considered as truly quasi-static.

The universality of these results is challenged by comparing them with measurement from different airfoil geometries, kinematics, and Reynolds number. The timescales of the NACA0018 are compared with those obtained for an OA209 airfoil [78] and for a NACA0015 [46] undergoing sinusoidal pitching motions. As the pitch rate varies continuously for a sinusoidal motion, we use the instantaneous pitch rate at the time the static stall angle is exceeded as the representative effective pitch rate for the sinusoidal motions [27, 56, 78]. The effective pitch rates for the sinusoidal motions vary between 0.0035 and 0.02. The measured stall delays or

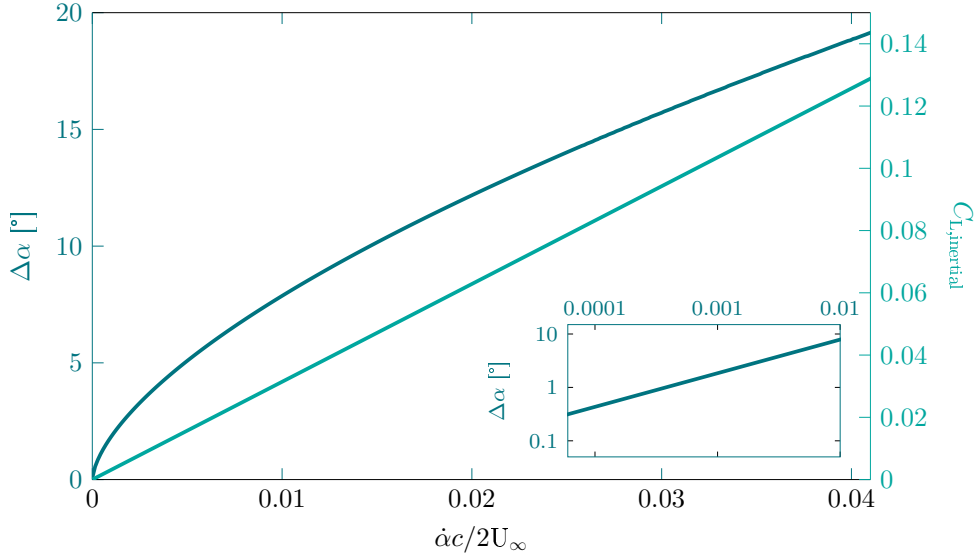


Figure 2.10: Estimated static stall accuracy $\Delta\alpha$ and inertial component of the lift coefficient $C_{L,inertial}$ against reduced frequency for static stall measurements performed with a continuous and uniform ramp-up motion.

reaction times for the three different airfoils, subjected to different kinematics, at different Reynolds numbers all collapse onto the same power law decay. This suggest that stall onset timescales are universal for airfoils undergoing stall at moderate to high Reynolds number where trailing edge stall is most common. Further investigations are desirable to explore the ranges of validity of this seemingly universal behaviour in terms of Reynolds number and variety of airfoil geometry.

The generality of the variation of the stall onset timescales as a function of the unsteadiness of the pitching motion presented in figure 2.9 can be used to lay out guidelines for reliably measuring the static stall angle and lift and drag polars. The systematic acceleration and deceleration related to a stepwise increase of the angle of attack is more likely to disturb the flow than a continuous motion. A continuous ramp-up motion with slow uniform pitch rate is thus preferred but how slow is slow enough? To answer that, we first fit a generalised power law decay to our experimental data yielding the following expression:

$$\Delta t_{c,reaction} = 1.25 \left(\frac{\dot{\alpha}c}{2U_\infty} \right)^{-0.37} . \quad (2.4)$$

This expression is used to determine the angular accuracy for the measurement of the static stall angle for a given pitch rate determined by the angular increase that occurs during expected stall reaction time:

$$\Delta\alpha = \frac{\dot{\alpha}c}{2U_\infty} 2\Delta t_{c,reaction} = 2.50 \left(\frac{\dot{\alpha}c}{2U_\infty} \right)^{0.63} . \quad (2.5)$$

The motion should be slow enough to minimise $\Delta\alpha$. In addition, we want to limit the inertial lift contributions associated with a dynamic motion. The inertial contribution to the lift coefficient for a continuous ramp-up motion can be estimated based on Theodorsen's theory

[102] as:

$$C_{l,\text{inertial}} = \frac{\pi \dot{\alpha} c}{2U_\infty} . \quad (2.6)$$

The evolution of both the static stall angular accuracy $\Delta\alpha$ and the inertial component of the lift coefficient $C_{l,\text{inertial}}$ as a function of the reduced pitch rate are presented in figure 2.10. Overall, the quasi-steady inertial lift contributions are a lesser issue than the stall angle increases. Reduced frequencies of the order of 1×10^{-4} yield a static stall angle accuracy of $\Delta\alpha < 1^\circ$. The quasi-steady inertial contribution for these pitch rates are negligible. When measuring a static lift response using a continuous slow ramp-up motion, the lift response can be considered a conventional static force response, free of unsteady and quasi-steady influences, and providing a reliable estimate of the critical static stall angle for $(\dot{\alpha}c)/(2U_\infty) < 1 \times 10^{-4}$.

2.4 Conclusion

We investigated the dynamic load variations and timescales of static stall by measuring loads acting on a blade undergoing two quasi-steady manoeuvres: (i) a slow continuous ramp-up motion from angles of attack 8° to 18° at a constant reduced pitch rate of 1.3×10^{-4} and (ii) a step-wise increase in angle of attack from 14.2° to 14.8° within 0.04 convective times. We defined three characteristic time delays associated with the transient flow development from attached to fully separated in response to the two types of manoeuvres: a reaction delay, a drop delay, and a relaxation delay.

The reaction delay is the time delay between the moment when the blade exceeds its stall angle of 14.2° and the moment when the lift collapses. This timescale characterises the duration of stall onset, which plays a central role in the distinction between static and dynamic stall. The reaction time is not influenced by pre-stall fluctuations for the slowest continuous ramp-up motion, and its occurrence histogram follows a normal distribution centred around 32 convective times. The unsteadiness induced by the step manoeuvre leads to pre-stall load fluctuations that are three times larger than those induced by the slow continuous ramp-up manoeuvre and do promote the onset of stall. The reaction delay linearly decreases with increasing fluctuations in the step manoeuvre.

The results for the reaction delay from the slow continuous ramp-up motion were compared with results from dynamic ramp-up manoeuvres with reduced pitch rates ranging from 1.3×10^{-4} to 0.14 and with previously obtained results from dynamic sinusoidal pitching motions with different airfoil geometries at different Reynolds numbers. This comparison revealed a universal power law decay of the stall delays from 32 convective times for the lowest pitch rates to a plateau around 4 convective times for reduced pitch rates above 0.04. The plateau level matches the vortex formation time, which is the minimum time interval required for the boundary layer to roll-up into a coherent stall vortex and separate from the airfoil. The standard deviation of the observed stall delays across multiple repetitions also rapidly decreased with increasing pitch rate which aids in promoting the occurrence of stall. Static stall is not phenomenologically different than dynamic stall and is merely a typical case of stall for low pitch rates where the onset of flow separation is not promoted by the blade kinematics.

Chapter 2. The dynamics of static stall

Based on the results, we propose that conventional static stall polars should be measured using a continuous and uniform ramp-up at a reduced frequency $< 1 \times 10^{-4}$ to minimise the angle of attack variation during the stall delay. The inertial lift contributions at these pitch rates are negligible. A continuous motion is preferred to a stepwise increase as the systematic acceleration and deceleration of a step motion is more likely to cause an unsteady flow response. If a step-wise motion is selected, it is advised to wait at least 30 convective times between the end of the step and the start of the measurements to allow for the flow to respond to the change in the angle of attack.

Findings from this chapter are central to this thesis' analysis of dynamic stall on vertical-axis wind turbines. The reaction delay $\Delta t_{c, \text{reaction}}$ for a wind turbine blade is shown to follow the same universal trend for increasing reduced frequencies observed for pitching wings in chapter 4. The fitted reaction delay power law is used as a criterion to compute a theoretical parametric map that predicts the occurrence and type of dynamic stall, either light or deep, on a wind turbine blade based on the chord-to-diameter and tip-speed ratios. The next chapter introduces the experimental apparatuses that were conceived throughout this thesis to perform wind turbine experiments.

3

EXPERIMENTAL APPARATUS: DESIGN AND VALIDATION

This is the last chapter from part I, covering the experimental apparatuses conceived as part of this thesis to investigate the flow physics of vertical-axis wind turbine blades. We present the nitty-gritty details about data validation and processing for completeness. Further chapters will mention the use of apparatus and methods but not repeat details related to data validation or limitation.

CHAPTER HIGHLIGHTS

- ⊙ Design of a modular, scaled-down Darrieus vertical-axis wind turbine with active blade pitching capabilities.
- ⊙ Instrumentation of the blade shaft to measure forces acting on the wind turbine blade.
- ⊙ Isolation of aerodynamic forces on the wind turbine blade by measuring and modelling other forces acting on the turbine blade.
- ⊙ Design of a rotating mirror apparatus for temporally and spatially resolved particle image velocimetry on the wind turbine blade.
- ⊙ Experimental methodology of time-resolved force and flow measurements and processing.

3.1 Design of a modular H-Darrieus wind turbine

The main challenge when designing a scaled model of an H-type Darrieus wind turbine is reaching the requirements of full geometric and dynamic similarity with commercial scale turbines [75]. Geometric similarity requires the model's shape to be preserved and the dimension to be scaled by a constant factor. Dynamic similarity requires the proportionality of forces and kinematics. For H-type Darrieus wind turbines, three governing parameters should be met to conserve geometric and dynamic similarity of flow phenomena occurring on the turbine's blades: the Reynolds number Re , the chord-to-diameter ratio and the tip-speed ratio λ . The definition and relevance of these parameters are discussed in section 1.1.3, and their influence in turbine flow physics is discussed in section 1.4.

Typical values for actual vertical-axes wind turbines for each of the three governing parameters are $Re_c \approx \mathcal{O}(10^6)$, $c/D \in [0.1 - 0.2]$ and $\lambda \in [1 - 6]$. We performed an iterative process to design a scaled wind turbine model that could cover this parameter space as broadly as possible, given the physical constraints of the test section in which the turbine is meant to operate.

We present the scaled-down model of a three-bladed H-type Darrieus wind turbine with active blade pitching in figure 3.1. The model was designed for use in a recirculating water channel with a test section of $0.6 \text{ m} \times 0.6 \text{ m} \times 3 \text{ m}$ and a maximum flow velocity of 1 m/s . By conducting measurements in water, we can reach higher Reynolds numbers for equivalent characteristic physical frequencies than by conducting experiments in air.

The central rotor axis is driven by a stepper motor that allows for a continuous variation of the rotational velocity from 0 Hz to 5 Hz with an encoder azimuthal resolution of 0.018° . These values yield turbine tip-speed ratios $\lambda \in [1 - 6]$ and Reynolds numbers $Re \in [2 \times 10^4 - 2 \times 10^5]$. The maximum Reynolds number is an order of magnitude below those encountered in large-scale applications. The effect of Reynolds number on flow separation and dynamic stall is relatively minor (section 1.4). Operating at low Reynolds numbers is not a limitation for investigating flow phenomena on an H-type Darrieus wind turbine blade [14].

A rotor with three arms is connected to the main shaft. Model turbine blades can be mounted on each of the arms, and the rotor can be operated with up to three blades. The arms are designed such that the blades can be positioned at different radial distances from the central rotor axis, resulting in a variable rotor diameter from 12 cm to 36 cm . The turbine blade was 3D printed using photosensitive polymer resin (Formlabs Form 2 stereolithography), sanded with very fine P180 grit paper and covered with matte black paint. The blade has a NACA0018 profile with a span of $s = 15 \text{ cm}$ and a chord of $c = 6 \text{ cm}$, so the chord-to-diameter ratio can take any value from 0.15 to 0.5 . The blades are mounted with splitter plates with a diameter equal to two chord lengths on each end. The splitter plates mitigate the blade tip effect and remove surface reflections from flow measurement images.

The turbine's compact geometry enables a relatively small blockage ratio of 12.5% , based on the ratio of the blade's frontal swept area and the water channel's cross-section. The blade is held by a cantilevered shaft, so there is no central strut interference with the flow. At low tip-speed ratios ($\lambda < 4$), the effective blockage is closer to 2.5% , which is the blockage ratio

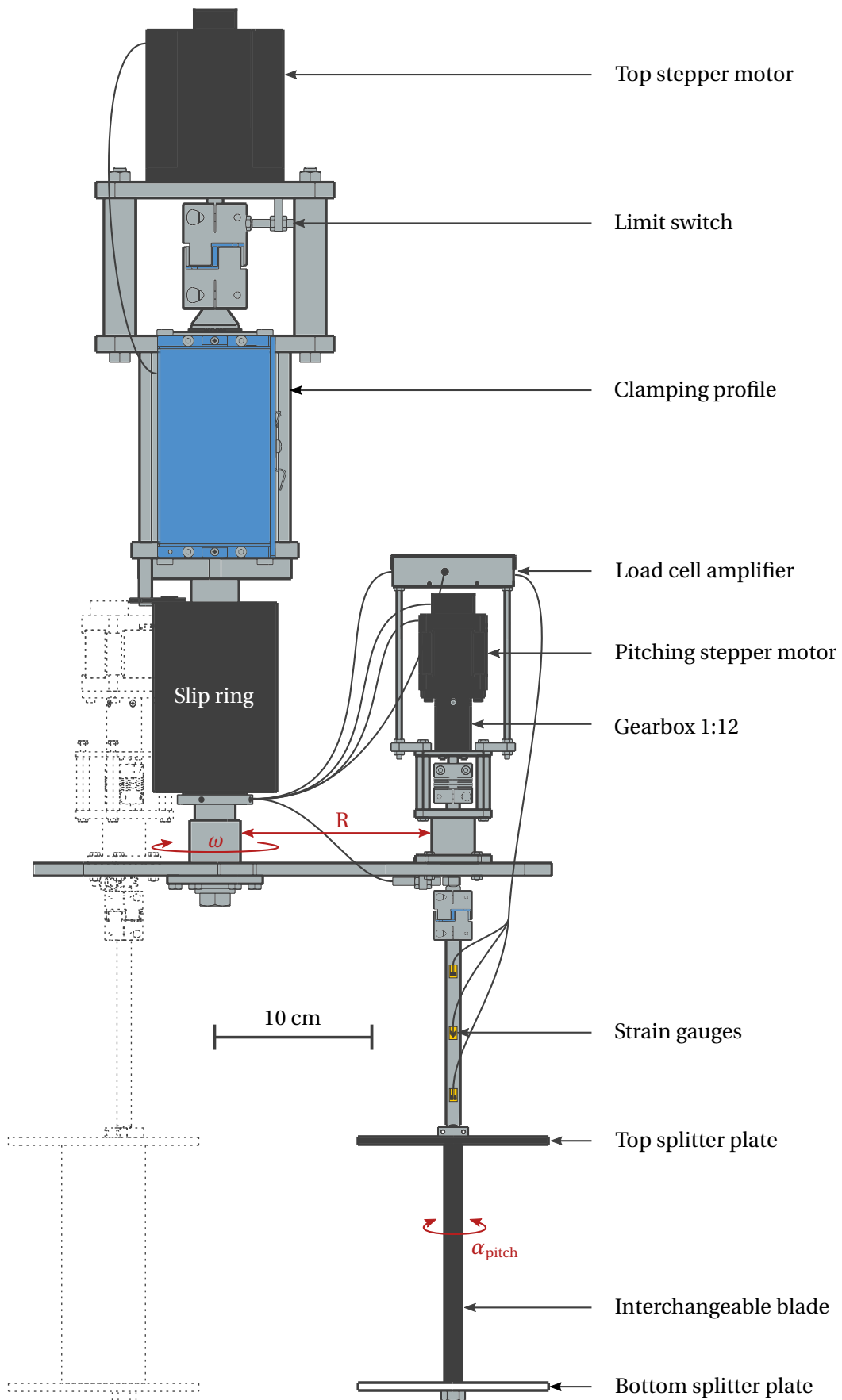


Figure 3.1: Schematic representation of the scaled-down H-type Darrieus wind turbine model with an instrumented shaft and active individual blade pitching. The dashed lines represented additional blade assemblies that can be added to the other two rotor arms. The red arrows represent modular degrees of freedom.

calculated based on the ratio of the blade area to the cross-sectional area. Additionally, a 2.5 chord length distance to the water channel's side walls is respected at all positions. Based on these observations, we consider the blockage and confinement effects small, and no correction to force measurements are applied [83, 92]. This assumption is supported by a numerical simulation of a single-bladed wind turbine with a 32 % blockage ratio [97].

Each turbine blade is connected to a separate direct-drive stepper motor with a 1 : 12 gear reduction yielding a high torque mechanism with a 0.0015° angular resolution. All motors are individually controlled and synchronised with the main rotor rotation using an eight-thread motion controller (GALIL-4080). Each motor was equipped with a limit switch. The absolute position of all motors relative to their limit switch was calibrated using a high-precision distance sensor. A homing procedure was designed such that all motors find their limit switch and move to their home position at the beginning of every experiment.

The blade shaft was instrumented using strain gauges to obtain time-resolved forces acting on the wind turbine blade. The strain gauges are powered and their output signal is amplified using an instrumentation amplifier with precision voltage reference placed on a printed circuit board mounted directly on the rotor arm. Implementing a built-in load cell yields a higher measurement accuracy, improved noise-to-signal ratio and less intrusive design than installing an industrial load cell. Our force sensor was calibrated *in-situ*, so it inherently accounts for structural properties of the turbine model, such as the rotor rigidity. The strain gauge signals are amplified onboard, so they do not accumulate noise by extensively travelling through wire and electronic components pre-amplification. The conception, calibration and validation of our in-house load cell are detailed hereafter.

3.2 Instrumentation of the blade shaft

3.2.1 Load cell conception

The in-house load cell was conceived using eight double bending strain gauges and two double torsion strain gauges. Each pair of strain gauges form a full Wheatstone bridge. Full Wheatstone bridges are twice as sensitive as half-bridges and compensate for temperature variations, e.g. from the heating up electronics. A schematic front view of the load cell shows the positions of the Wheatstone bridges W in figure 3.2. The bridges W_R and W_θ respond to forces in the R and θ directions, and W_z to moments about the z direction.

An example load distribution $P(z)$ of the flow acting on the turbine blade is shown in figure 3.2. In this example, we want to divide the loading $P(z)$ into the resulting shear force F_R and the moment M_θ about the centre of the blade, to be able to isolate the relevant aerodynamic forces. This decoupling is achieved by installing the bridge pairs $(W_{R,1}, W_{R,2})$ and $(W_{\theta,1}, W_{\theta,2})$ 50 mm apart along the shaft, as indicated in the figure. With this configuration, the bending moment BM in each direction is measured at two positions along the shaft, allowing to solve the equation $BM = Fl_z + M$ for the shear force F and moment M , where l_z is the distance from the blade's midspan location z_0 .

The load cell measures the voltages from the five Wheatstone bridges, which are converted into actual forces and moments with the calibration matrix R , following:

$$F = R \cdot V, \text{ or}$$

$$\begin{bmatrix} F_\theta \\ F_R \\ M_\theta \\ M_R \\ M_z \end{bmatrix} = \begin{bmatrix} R_{11} & R_{12} & \cdots & R_{15} \\ R_{21} & R_{22} & \cdots & R_{25} \\ \vdots & \vdots & \ddots & \vdots \\ R_{51} & R_{52} & \cdots & R_{55} \end{bmatrix} \cdot \begin{bmatrix} V_1 \\ V_2 \\ V_3 \\ V_4 \\ V_5 \end{bmatrix} \quad (3.1)$$

where $F_{\theta/R}$ are the forces in the blade's tangential and radial directions, $M_{\theta/R/z}$ are the moments acting at the blade's half span, quarter-chord position about the tangential, radial, and

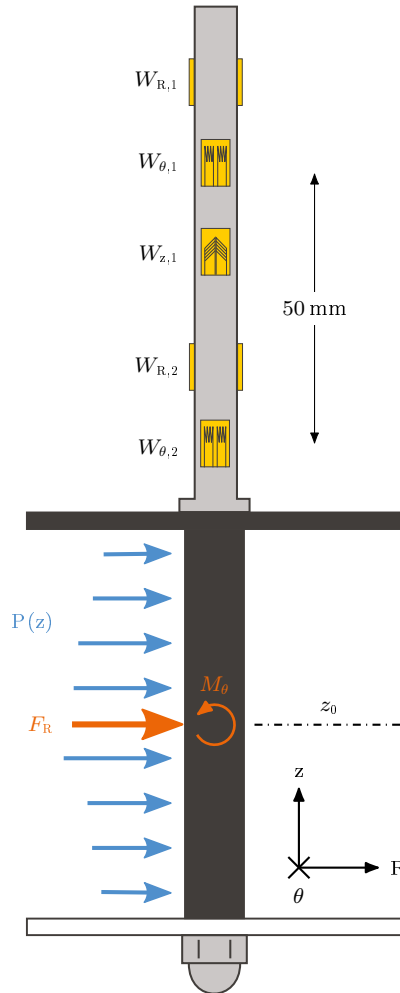


Figure 3.2: Load cell design diagram. Each Wheatstone bridge compose of a pair of strain gauges is indicated by a W_x where x represents the direction of the measured force or moment axis in the case of W_z . The force distribution exerted by the flow on the wind turbine blade is represented as $P(z)$. In this orientation, the load distribution results in a shear force F_R and a bending moment M_θ . The diagram is not to scale.

Chapter 3. Experimental apparatus: design and validation

spanwise axes, V_i are the voltages obtained from the i^{th} Wheatstone bridge and R_{ij} are the calibration matrix coefficients obtained from the linear regression. For studies covered in this thesis, M_θ and M_R are not needed.

3.2.2 Load cell calibration

To obtain the calibration matrix R , we apply known forces and moments F^{calib} and measure the corresponding output voltages V^{calib} . It is then possible to determine the inverse of the calibration matrix with

$$V^{\text{calib}} = R^{-1} \cdot F^{\text{calib}}. \quad (3.2)$$

The matrix R^{-1} is computed by solving equation (3.2) with a least-squares fit, and the calibration matrix R is simply obtained by inverting R^{-1} .

The wind turbine is mounted on a fully-orthogonal test rig to perform the calibration procedure. Loads are applied on the load cell using a v-groove ball bearing or a frictionless pulley, a wire, and a crossbeam mounted on the blade shaft instead of the turbine blade. The calibration rig is shown in figure 3.3. Loads and moments acting in the desired direction are generated by changing the crossbeam orientation relative to the bearing and the force application point in the crossbeam. We apply weights statically using the wire and ball bearing and acquire measurements for 10 s to get the mean voltage and standard deviation.

We apply nine loading conditions consecutively for each of the five relevant positions on the crossbeam. The vertical positions apply to the calibration of shear forces $F_{\theta/R}$, while the horizontal positions were used to calibrate the axial moment M_z . The nine loading conditions are multiples of a unit weight $W \approx 300$ g selected to properly discretise the expected range of forces to be measured by the wind turbine model. The loading routine was as follows: $0W$, $1W$, $2W$, $3W$, $4W$, $3W$, $2W$, $1W$, $0W$. This routine also enables us to determine the error related to loading hysteresis. In total, 1350 static measurements are performed to generate the calibration data used in equation (3.2). The calibration procedure demonstrated very satisfactory linearity between measured voltage and applied force and very low hysteresis ($< 1\%$).

3.2.3 Load cell uncertainty quantification

The load cell uncertainty U_{lc} is important to estimate the level of trust we can attribute to the measured forces. This uncertainty combines both the load cell's precision and accuracy. The precision is given by the disagreement between repeated measures of the same reference loading condition and is quantified by the standard deviation σ of these measurements. The accuracy defines the error e between the experimental values and the true reference. The experimental value is determined as the average of the repetitions for a single loading condition. The combination of the error and the standard deviation yields the uncertainty:

$$U_{lc} = \sqrt{\sigma^2 + e^2}. \quad (3.3)$$

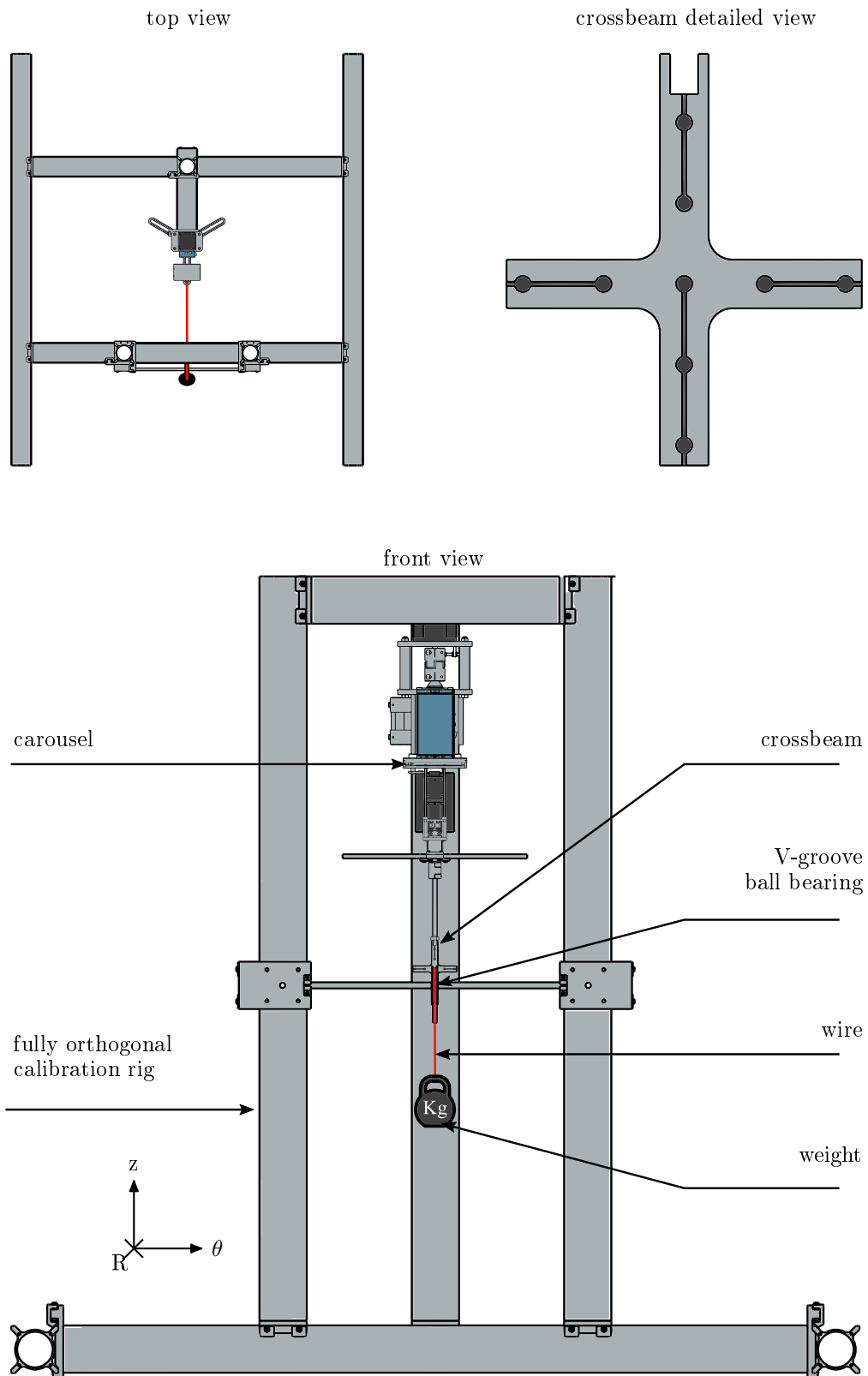


Figure 3.3: Orthogonal calibration rig for the wind turbine's load cell .

Chapter 3. Experimental apparatus: design and validation

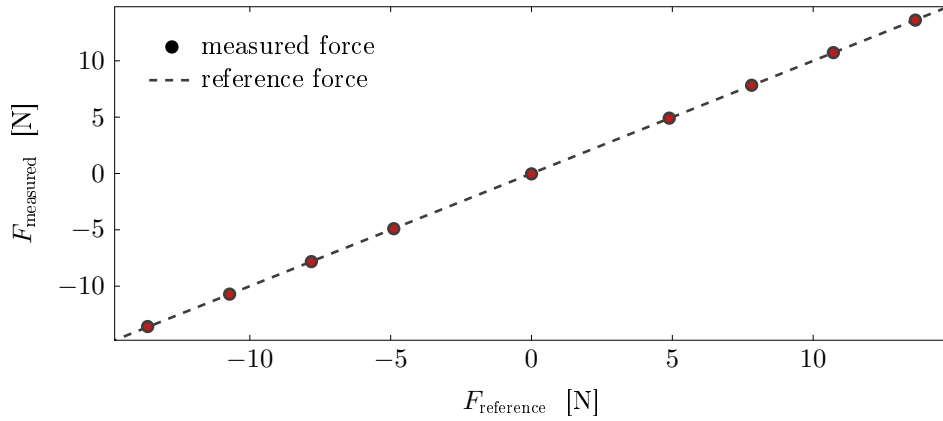


Figure 3.4: Force measured by the load cell in the tangential θ direction compared to reference force applied with a static weight. Error bars are very small and hidden by the markers.

As an example, the calibration results for the tangential force F_θ are presented in figure 3.4. The forces obtained from the voltage measurements multiplied by the calibration matrix F_{measured} are shown against the reference forces statically applied with the weights $F_{\text{reference}}$. For each loading condition, the measurement is repeated between 50 and 100 times. The diagonal dashed line indicates the ideal case, where the reference and measured values coincide, and the deviation from this line indicate the error e . The uncertainty is computed for each loading conditions with equation (3.3) and averaged.

Following this procedure, the uncertainties for all loads and moments were determined and are listed in table 3.1. The values reveal an overall low experimental uncertainty, below 5 % of the dynamic range, and confirm the reliability of the load cell results.

Component	Max range	Uncertainty
F_θ	$\pm 50 \text{ N}$	$\pm 0.06 \text{ N}$
F_R	$\pm 50 \text{ N}$	$\pm 0.20 \text{ N}$
M_x	$\pm 0.5 \text{ N m}$	$\pm 0.009 \text{ N m}$
M_y	$\pm 0.5 \text{ N m}$	$\pm 0.006 \text{ N m}$
M_z	$\pm 0.5 \text{ N m}$	$\pm 0.005 \text{ N m}$

Table 3.1: Load cell uncertainty for each load and moment.

3.2.4 Load cell aerodynamic validation

We validate our in-house load cell by characterising the static aerodynamic performance of the NACA0018 blade on the wind turbine. We place the wind turbine model at the centre of the water channel test section. The turbine top motor was initiated such that the blade was brought to the starting position of a wind turbine experiment, facing the flow at $\theta = 0^\circ$ (figure 1.2). At this position, the blade is 2.5 chord length away from the side wall. The flow velocity was set to 0.83 m/s, resulting in a chord-based Reynolds number $\text{Re} = \frac{U_\infty c}{\nu} 5 \times 10^4$. The turbine pitching motor performed a quasi-static pitch-up manoeuvre at a reduced frequency

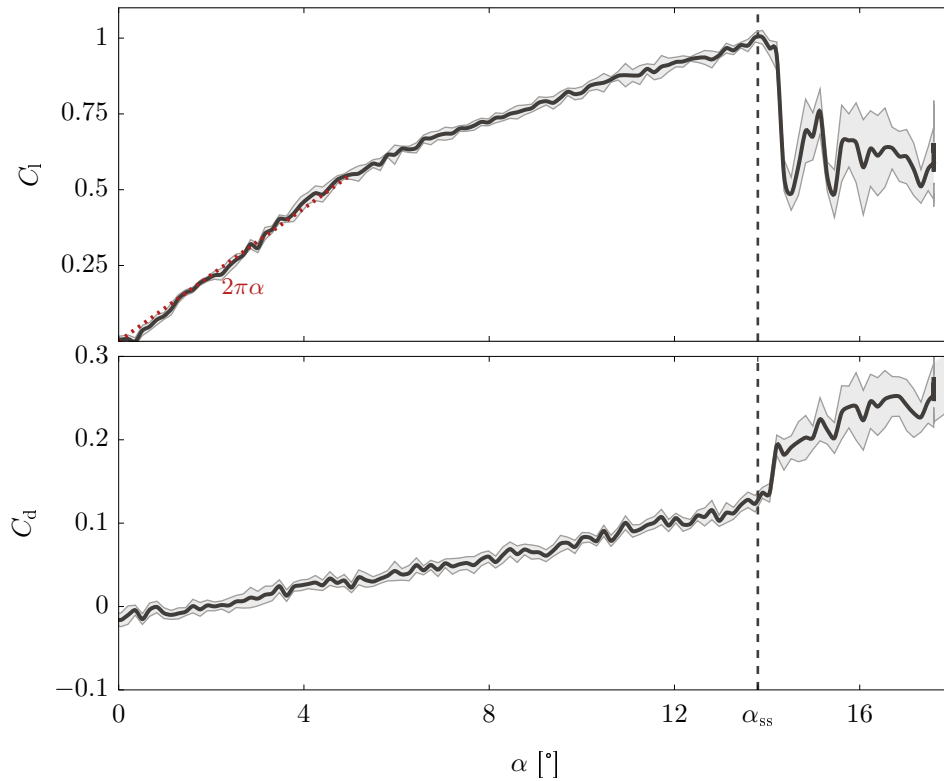


Figure 3.5: Lift and drag coefficients (C_l and C_d) against angle of attack. The turbine blade was subjected to an infinitely slow ramp-up following the procedure described in chapter 2. Aerodynamic forces experienced by the turbine blade were measured with our in-house load cell.

$k = 10^{-4}$, as suggested in chapter 2. The measured lift and drag coefficients are shown against the blade's angle of attack in figure 3.5.

The lift coefficient increases linearly for $\alpha \in [0^\circ - 5^\circ]$ and follows the 2π lift slope predicted by thin-airfoil theory. Thin-airfoil theory predicts the lift of a two-dimensional blade element operating in an inviscid and incompressible flow. The agreement between our experimentally measured lift coefficient and the thin-airfoil theory prediction validates the load cell's ability to capture aerodynamic forces experienced by the blade. This agreement also suggests that the splitter plates successfully mitigate three-dimensional tip effects and that the water channel walls do not significantly influence the blade-level flow physics in a static scenario.

The lift slope decreases past low angles of attack. This decrease is probably due to the flow's separation point on the suction side of the blade gradually travelling upstream from the trailing edge to the blade's leading edge. Stall occurs at an angle of attack $\alpha_{ss} = 13.7^\circ$, which is in excellent agreement with same profile blades from literature operating at $Re = 5 \times 10^4$. Post-stall load fluctuations related to vortex shedding also behave as expected.

The drag coefficient gradually increases between $\alpha = 0^\circ$ and α_{ss} , arguable because the aerodynamic force experienced by the blade is gradually re-oriented in the drag direction. Stall results in a rapid increase in the drag coefficient. The load cell's capture of unsteady forces experienced by the wind turbine blade undergoing static stall is very satisfactory, showing

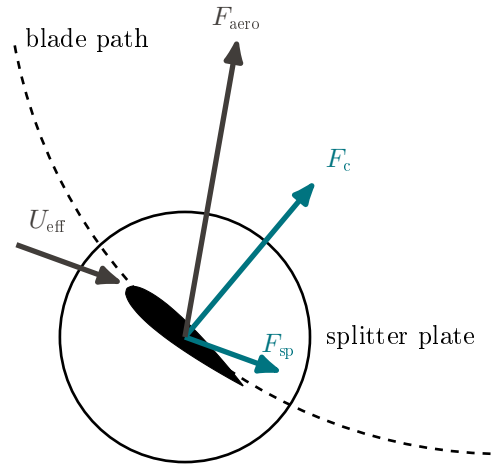


Figure 3.6: Free body diagram of the forces experienced by the turbine blade during wind turbine experimentation.

similar trends to those highlighted in chapter 2 from data acquired using an industrial load cell. This result is particularly encouraging, considering that the forces experienced by the blade are small compared to the full dynamic range the load cell was designed to measure. To perform vertical-axis wind turbine experimentation, we first isolate the aerodynamic force from the other forces experienced by the blade.

3.3 Isolation of aerodynamic forces on the wind turbine blade

We wish to investigate the aerodynamic forces F_{aero} experienced by the wind turbine blade. The built-in load cell captures two additional force contributions during wind turbine experimentation in the water channel: the centripetal force F_c related to the mass below the load cell following a circular path and the aerodynamic splitter plate force F_{sp} (figure 3.6). These two force components were isolated, measured, and subtracted from the raw force data to obtain the results presented in this thesis.

The centripetal force was measured by rotating the wind turbine blade in air at eight different rotational frequencies spanning the range of expected experimental rotational frequencies. For each rotational frequency, the centripetal force was measured for 30 s. The time-averaged centripetal force is presented as a function of the rotational frequency in figure 3.7. The error bars represent the absolute error computed in section 3.2.3. The centripetal force evolves with $F_c = mR\omega^2$, where m is the mass below the load cell, R the radius of the blade's circular path, and ω is the turbine's rotational frequency. A second-order polynomial fit was used to determine mR . The experimental data fit yielded an expression for the centripetal force $F_c = 0.047\omega^2$, as shown in figure 3.7.

The aerodynamic force related to the presence of the splitter plates F_{sp} was measured by operating the vertical-axis wind turbine in the water channel without the blade. Instead, a $D_{\text{cyl}} = 12$ mm diameter and $L_{\text{cyl}} = 150$ mm long cylinder was placed in between the two splitter

3.3 Isolation of aerodynamic forces on the wind turbine blade

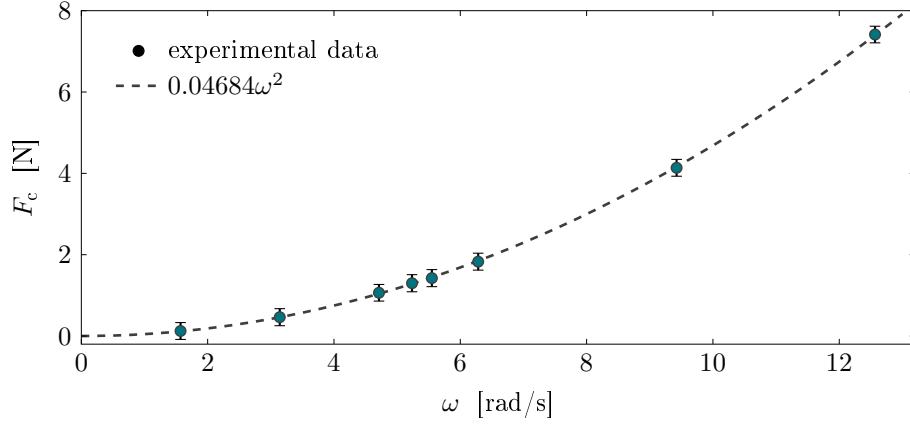


Figure 3.7: Centripetal force F_c measurement and modelling. The scattered points represent the averaged experimental measurements. Error bars represent the absolute error computed in section 3.2.3. The dashed line is the fitted polynomial function used to model the centripetal force.

plates to hold them in place. The aerodynamic forces generated by the cylinder F_{cyl} were offset using $F_{cyl} = 0.5C_{D,cyl}\rho U_{eff}^2 D_{cyl}L_{cyl}$, where $C_{D,cyl}$ was obtained from [91], and U_{eff} is calculated using equation (1.3). The inertial forces from the cylinder setup were also measured and subtracted from the splitter plate measurements. The splitter plate force $F_{sp,R}$ in the radial direction was small, below 5 % of the expected dynamic load during vertical-axis wind turbine experimentation. This value is considered to be within the error margin of the aerodynamic measurements and is ignored. The temporal evolution of $F_{sp,\theta}$ in the tangential direction for a wide range of tip-speed ratios is presented in figure 3.8 (a). Note that the maximum force in this direction reaches values above 10 N. As expected, $F_{sp,\theta}$ is maximum at $t/T = 0$ when the splitter plates are facing the flow and the effective velocity U_{eff} is maximum.

The splitter plate forces are modelled using a typical drag coefficient formulation:

$$F_{sp,\theta} = C_{D,sp}\rho U_{eff}^2 \pi R_{cyl}^2 \quad (3.4)$$

where R_{cyl} is the radius of the splitter plates and $C_{D,sp}$ is the drag coefficient to be determined by fitting the experimental data. A polynomial fit yielded a drag coefficient of $C_{D,sp} = 0.09$. The modelled splitter plate forces in the tangential direction are presented for the same range of tip-speed ratio in figure 3.8b. The model represents the experimental data best in the first and last quarter of the turbine rotation when the force is the largest. The force minimum is slightly delayed and extended for the experimental data compared to the modelled forces around $t/T = 0.5$. The delay is arguably related to wake delay and vortical structures interacting with the cylinder and splitter plates in the region. The small difference between the model and experimental results is deemed acceptable because the splitter plate influence is below 1 N when $0.25 \leq t/T < 0.75$. The model offers a satisfactory representation of the splitter plate interaction.

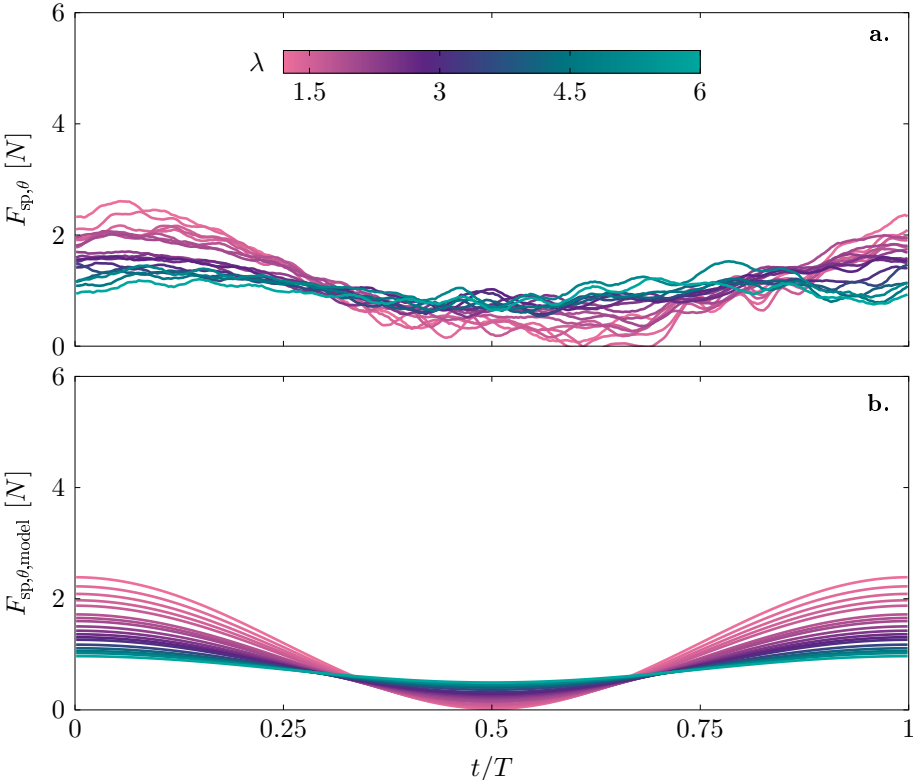


Figure 3.8: Tangential force related to the splitter plates (a) experimental measurement and (b) model. The range selected for the vertical axis represents the typical range of forces acquired in the tangential direction during wind turbine experiments.

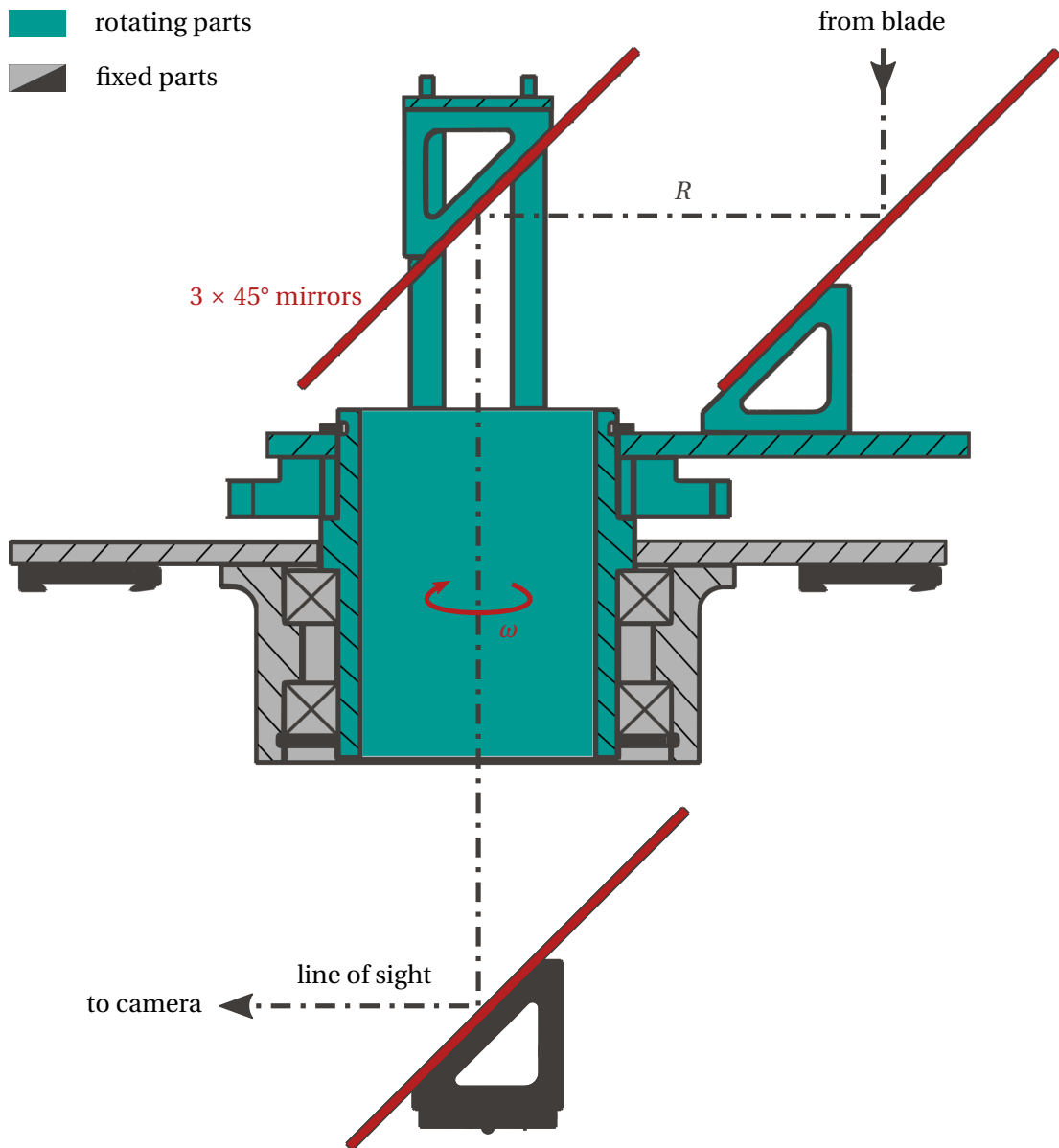


Figure 3.9: Section view of the rotating mirror system designed to acquire time-resolved particle image velocimetry with high spatial resolution. Sectioned parts appear with a striped pattern.

3.4 Design of a rotating mirror apparatus

Obtaining time-resolved particle image velocimetry (PIV) with satisfactory spatial resolution on a vertical-axis wind turbine is challenging. High-frequency cameras generally have limited resolution or limited recording time. Otherwise, the acquired data becomes prohibitively large to record in real-time. A standard solution is to capture the entire path followed by the turbine blade using a low-frequency high-resolution camera (e.g. 4096 px × 4096 px at 15 Hz) and capture phase-locked data. This solution involves obtaining multiple images of the blade crossing through specific azimuthal positions and computing phase-averaged flow fields to

reconstruct the temporal evolution of the flow. Even with a high-resolution camera and a high chord-to-diameter ratio, capturing the entire field of view with a single camera will result in a relatively low spatial resolution.

Another solution is using several cameras to divide the field of view into smaller high-resolution regions. This solution is expensive and involves complicated triggering and post-processing to stitch the fields of view back together, particularly for time-resolved data. Obtaining time-resolved PIV is desirable to investigate the highly unsteady aerodynamics of vertical-axis wind turbine blades.

We designed a rotating mirror apparatus to obtain time-resolved PIV with high spatial resolution. A cross-section view of this apparatus is shown in figure 3.9. The parts are colour coded depending on whether they are stationary or rotating. Two rotating mirrors are placed on a platform that rotates about an axis collinearly with the wind turbine's axis of rotation. The mirror on the right is placed at the same radius R as the wind turbine blade and reflects the blade's image to the left rotating mirror. The blade's image is reflected downward through a hollow shaft to a third stationary mirror placed underneath the apparatus. The stationary mirror is optional but allows us to position the camera horizontally. Using a 135 mm lens, this apparatus yields a 2.5×2.5 chord-length field of view centred around the blade with limited distortion and parallax effects.

3.5 Performing time-resolved force and flow measurements in a recirculating water channel

Experiments were conducted in a recirculating water channel with a test section of dimensions $0.6 \text{ m} \times 0.6 \text{ m} \times 3 \text{ m}$ and a maximum flow velocity of 1 m/s . The test section has transparent acrylic walls bound by a metallic frame, providing optimal optical access for velocity field measurements. A representation of the entire experimental apparatus is shown in figure 3.10.

We place the scaled-down turbine model at the centre of the test section. For all the data presented in this thesis, the rotational frequency was kept constant at 0.89 Hz , yielding a constant chord-based Reynolds number of $\text{Re}_c = (\rho \omega R c) / \mu = 50\,000$. The turbine's rotational frequency was kept constant to maintain a constant chord-based Reynolds number throughout the experiments. To vary the tip-speed ratio, we change the water channel's incoming flow velocity from 0.14 m/s to 0.70 m/s to obtain tip-speed ratios ranging from 1.2 to 6.

For each experiment that involves load measurements, the wind turbine model starts at rest, with the blade facing the oncoming flow. The turbine blade is accelerated to its prescribed rotational speed. After reaching the target rotational speed, we allow five complete turbine rotations for the turbine wake to develop before accounting for force recordings. The blade is actuated from the end of the first turbine rotation for blade pitching experiments. Aerodynamic forces acting on the turbine blade are recorded at 1000 Hz for 100 complete turbine rotations, and then the blade is brought to rest.

We follow the same procedure for experiments that involve high-speed particle image ve-

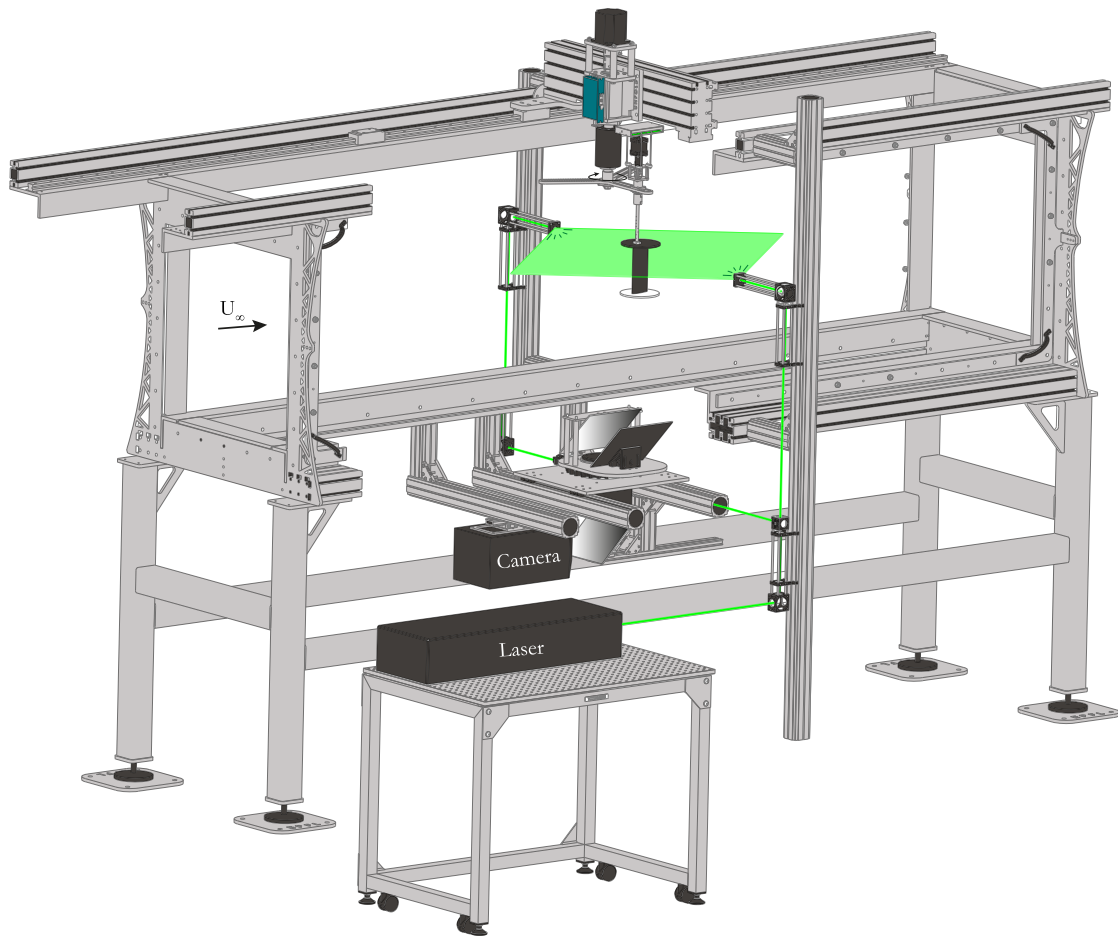


Figure 3.10: Schematic of the experimental setup including the wind turbine model, the light sheet, the rotating mirror system and high-speed camera for particle image velocimetry.

locimetry (PIV), except data is recorded for 23 s, or 20.5 turbine rotations, before the camera's memory is saturated. A dual oscillator diode-pumped ND:YLF laser ($\lambda = 527$ nm) with a maximum pulse energy of 30 mJ and a beam splitter were used to create two laser sheets from opposite sides of the channel. The light sheets were oriented horizontally at the mid-span of the turbine blade (figure 3.10). A high-speed camera and the rotating mirror apparatus were installed below the channel to capture the flow around the blade. The camera had a sensor size of $1024 \text{ px} \times 1024 \text{ px}$ (Photron Fastcam SA-X2), and an acquisition frequency is 1000 Hz.

3.6 Data processing

3.6.1 Filtering

Force data was filtered using a second-order low-pass filter with the cut-off frequency at 30 Hz. This frequency is multiple orders of magnitude larger than the pitching frequency and approximately 50 times larger than the expected post-stall vortex shedding frequency based on a chord-based Strouhal number of 0.2 [63]. The volts measured during the experiment with

our load cell are converted into forces using equation (3.1).

PIV images were filtered using a high-pass filter with a 4 px kernel size to improve the image contrast. No background image removal was required, as the black-painted top splitter blade blocked any potential parasitic background. The data was processed following standard procedures using a multi-grid interrogation algorithm [85]. The final window size was 48 px \times 48 px with an overlap of 75 %. This yields a grid spacing or physical resolution of 1.7 mm = 0.029c.

3.6.2 Force projection and non-dimensionalisation

The forces presented in this thesis are two shear forces applied at the blade's mid-span in the radial F_R and azimuthal F_θ directions, and the pitching moment about the blade's quarter-chord M_z (figure 3.11). The built-in load cell rotates along with the turbine blade, so no force projections are required unless the blade is pitching. For experiments where the blade is subjected to a pitch profile α_{pitch} , the measured forces are normal F_n and tangential to the blade's chord F_t . Those forces are projected back to the radial F_R and tangential to the blade's path F_θ directions:

$$F_R = F_t \sin(\alpha_{pitch}) + F_n \cos(\alpha_{pitch}), \quad (3.5)$$

$$F_\theta = F_t \cos(\alpha_{pitch}) - F_n \sin(\alpha_{pitch}). \quad (3.6)$$

The total force applied to the blade is computed by combining the two shear forces: $F_{tot} = \sqrt{F_R^2 + F_\theta^2}$. All force coefficients are non-dimensionalised by the blade chord c , the blade span

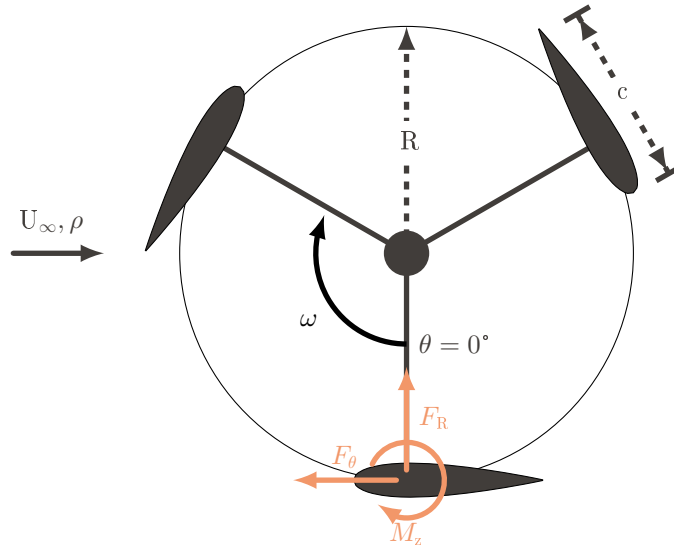


Figure 3.11: Aerodynamics force direction convention diagram. Here, a fluid of density ρ flows with a free stream velocity U_∞ from left to right.

s, and the blade velocity $U_b = \omega R$ such that:

$$C_{\text{tot}/R/\theta} = \frac{F_{\text{tot}/R/\theta}}{0.5\rho U_b^2 s c} .$$

The subscripts tot, R, or θ refer to the total force, the radial, or the tangential force component.

From our load measurements, we can also retrieve an idealised turbine power coefficient. The instantaneous power P generated by a vertical-axis wind turbine is linearly proportional to the tangential aerodynamic force experienced by the blade:

$$P(\theta) = F_\theta \omega R, \quad (3.7)$$

where ω is the rotational frequency and R is the turbine's radius. We can calculate the instantaneous power coefficient by normalising the estimated instantaneously generated power by the power available in the flow:

$$C_p(\theta) = \frac{P}{0.5\rho U_\infty^3 A_{\text{swept}}} , \quad (3.8)$$

where A_{swept} is the turbine's swept area given by the product of the turbine diameter and the blade's span. This definition of the power coefficient is idealised because it does not account for any mechanical or electronic losses that would occur on a wind turbine between the turbine blade torque generation and the generator's output.

3.6.3 Flow measurement mapping

Post-processing PIV depends on the frame of reference of interest. The data can be visualised in the wind turbine's fixed frame of reference or the blade's rotating frame of reference. Two steps are required to visualise the data in the wind turbine's frame of reference. The data needs to be mapped to its absolute position in space, and the influence of the mirror's rotation needs to be removed. Mapping involves translating the blade's local frame of reference centred at the blade's quarter-chord with coordinates (\tilde{x}, \tilde{y}) to a global frame of reference centred at the turbine's axis of rotation with coordinates (x, y) (figure 3.12). The rotating mirror apparatus induces a translation of raw images along the blade's circular path but does not induce any solid body rotation on the images, as shown by the coloured circles tracking the image corners in figure 3.12. This difference is important for interpreting the measured velocity field and the computation of the vorticity field. Mapping is thus performed for a given point P using:

$$x_p = \tilde{x}_p + R \sin(\theta), \quad (3.9)$$

$$y_p = \tilde{y}_p + R \cos(\theta). \quad (3.10)$$

Removing the influence of the mirror's translation on the measured velocity fields is achieved using the following:

$$u_p = \tilde{u}_p + \omega R \sin(\theta), \quad (3.11)$$

$$v_p = \tilde{v}_p + \omega R \cos(\theta). \quad (3.12)$$

Here, R is a fixed parameter equal to the distance between the axis of rotation and the centre of the mirror. This transformation does not affect the curl of the measured vector field, so vorticity is conserved across our two fields of view.

Visualising the data in the blade's frame of reference requires a single step: rotating the images about the blade's quarter-chord. The measured velocity field represents the effective flow conditions acting on the blade. The images are rotated from their frame of reference (\tilde{x}, \tilde{y}) to a rotated frame of reference $(x_{\text{rot}}, y_{\text{rot}})$ using a 2D rotation matrix:

$$\begin{bmatrix} x_{\text{rot}} \\ y_{\text{rot}} \end{bmatrix} = \begin{bmatrix} \cos(\theta) & -\sin(\theta) \\ \sin(\theta) & \cos(\theta) \end{bmatrix} \begin{bmatrix} \tilde{x} \\ \tilde{y} \end{bmatrix}. \quad (3.13)$$

For convenience, the velocity field in the rotated frame of reference is interpolated to a square Cartesian frame with fixed dimensions across all images.

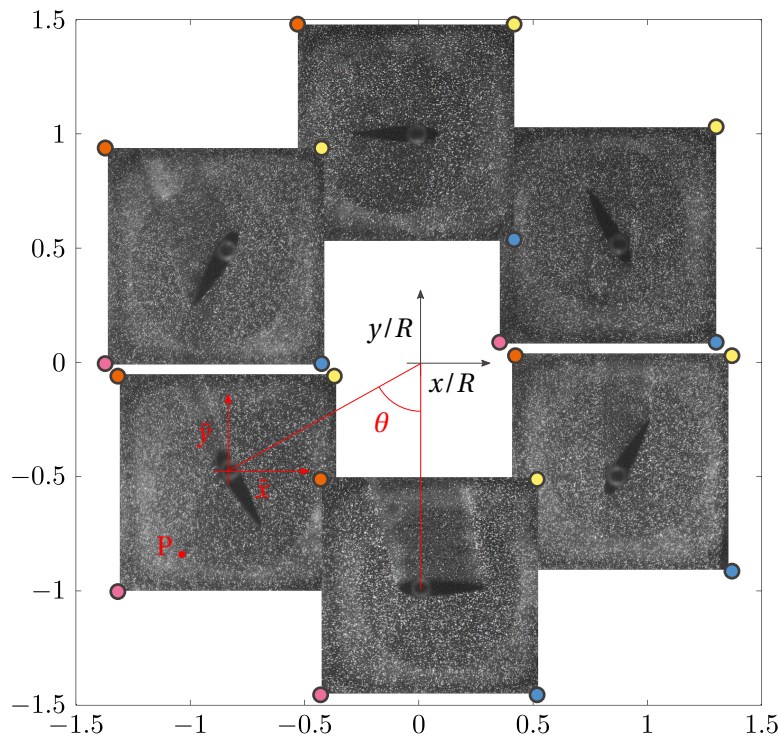


Figure 3.12: Mapping diagram for processed particle image velocimetry. Raw images are shown at their absolute position in the wind turbine's fixed frame of reference (x, y) centred at the turbine's axis of rotation.

3.6.4 Phase-averaging

Load measurements are obtained and phase-averaged over 100 wind turbine revolutions for all tip-speed ratio cases. Phase-averaging involves splitting the phase space into 540 bins that cover 0.67° without overlap. We calculate the mean performance value and its standard deviation for each bin. This method allows us to visualise the mean performance of the turbine blade at 540 phase positions and the corresponding cycle-to-cycle variations of the performance. The number of bins was selected to be large enough such that sufficient data points lie in each bin and small enough to reduce the smoothing of the data.

**DYNAMIC STALL ON VERTICAL-AXIS
WIND TURBINES REVISITED**

PART II

4

THE DYNAMIC STALL DILEMMA

The power performance of vertical-axis wind turbines is highly sensitive to flow separation and dynamic stall. Our experimental apparatus can obtain time-resolved flow and force measurements on a wind turbine blade for a wide operating envelope. This data allows us to characterise the interplay between the flow structures and the torque generated by wind turbine blades for a wide range of tip-speed ratios. This chapter discusses the dynamic stall dilemma: forming large-scale vortices yields a significant peak in power production, but vortex lift-off results in heavy drag excursions and undesirable load fluctuations. We quantify vortex strength, load fluctuations and torque production to compare how different tip-speed ratios score within this dilemma.

The work presented in this chapter was published in *Renewable Energies* [62].

CHAPTER HIGHLIGHTS

- ⊙ Decreasing tip-speed ratios offer higher peak power performance during vortex formation, but also aggravated post stall conditions.
- ⊙ We map turbine operating conditions to one of three regimes: deep stall, light stall, and no stall.
- ⊙ The light stall regime offers VAWT the best compromise in the dynamic stall dilemma as it yields positive tangential forces during the upwind and downwind rotation and reduces load transients by 75 compared to the deep stall regime.

4.1 Introduction

Vertical-axis wind turbines are excellent candidates for wind technology diversification, but their development was limited by their aerodynamic complexity. For vertical-axis wind turbines operating at low tip-speed ratios, typically $\lambda < 3$, the blade undergoes large variations in effective flow conditions (figure 1.2). The large unsteady excursions of the effective angle of attack beyond its static stall angle α_{ss} and the varying inflow velocity can lead to the occurrence of dynamic stall [14, 40, 97].

Dynamic stall is characterised by the formation, growth, and shedding of large-scale vortices [15]. Massive flow separation is delayed to higher angles of attack which leads to a lift overshoot with respect to the static response. The shedding of large-scale vortices is generally followed by a dramatic loss in aerodynamic efficiency and highly unsteady loads [72, 77]. Wind turbines operating at low tip-speed ratios experience stall vortices that form on the inboard side of the blade in the upwind half of the rotation. When these vortices shed, they convect downstream and interact with the blade for an extended period of time throughout the downwind half of the blade's rotation [23, 96, 97]. Blade-vortex interaction and post-stall vortex shedding cause highly transient and heavy load fluctuations that jeopardise the turbine's structural integrity and often lead to premature fatigue failure [24, 30, 79]. The low tip-speed ratio operation is associated with high variations in angle of attack, dynamic stall, and extended periods of time during which the flow is massively separated, compared to higher tip-speed ratio operation.

The goal of this chapter is to provide a detailed analysis of the interplay between dynamic stall and the aerodynamic performance of a single-bladed vertical-axis wind turbine or cross-flow turbine blade. This was achieved by experimentally collecting time-resolved unsteady aerodynamic loads and time-resolved flow field data on a scaled-down H-type Darrieus wind turbine operating at tip-speed ratios ranging from 1.2 to 6. Successive stages in the flow development within a single turbine rotation are identified and their influence on the loads experienced by the blade are described for different tip-speed ratios. Specific metrics are proposed to evaluate the performance of the wind turbine blade in terms of torque production and by the level of load transients related to flow separation. The timescales related to dynamic stall development are systematically quantified and compared to universal vortex formation timescales that are previously identified in literature. Based on the temporal evolution of unsteady loads, flow structures, and load transients, we establish a criterion to categorise the turbine's operation into one of three regimes: no stall, light stall, and deep dynamic stall. The criterion agrees with previously published work, highlighting the occurrence of stall for tip-speed ratios $\lambda < 4$ and a transition from light to deep stall at a critical tip-speed ratio related to the vortex formation timescale. To generalise our findings, we present a parametric map that predicts the expected stall regime based on the turbine's operating parameters, namely the tip-speed ratio λ and chord-to-diameter ratio c/D . These findings are valuable in the design of cross-flow and vertical-axis wind turbine geometries and operating conditions as the occurrence and degree of stall govern the expected performance of wind turbines.

4.2 Experimental apparatus and methods

Experiments were conducted in a recirculating water channel with a test section of dimensions $0.6 \text{ m} \times 0.6 \text{ m} \times 3 \text{ m}$. A representation of the full experimental apparatus is shown in figure 4.1.

4.2.1 Vertical-axis wind turbine model

A scaled-down model of a single-bladed H-type Darrieus wind turbine was mounted in the centre of the test section. The turbine was kept constant here at 30 cm. We used the single blade configuration to focus on the flow development around the blade in the absence of interference from the wakes of other blades. The blade has a NACA0018 profile with a span of $s = 15 \text{ cm}$ and a chord of $c = 6 \text{ cm}$, yielding a chord-to-diameter ratio of $c/D = 0.2$. The rotational frequency was kept constant at 0.89 Hz, yielding a constant chord-based Reynolds number of $\text{Re}_c = (\rho\omega Rc)/\mu = 50000$, where ρ is the density and μ the dynamic viscosity of water. To investigate the role of the tip-speed ratio in the occurrence of dynamic stall, we systematically vary the water channel's incoming flow velocity from 0.14 m/s to 0.70 m/s to obtain tip-speed ratios ranging from 1.2 to 6.

4.2.2 Force measurements

For each experiment, the wind turbine model starts at rest with the blade facing the oncoming flow. The turbine blade is accelerated to its prescribed rotational speed. After reaching the target rotational speed, we wait for five full turbine rotations before starting the load recordings. Aerodynamic forces acting on the turbine blade are recorded at 1000 Hz for 100 full turbine rotations, then the blade is brought to rest. The forces presented in this chapter are two shear forces applied at the blade's mid-span in the radial F_R and azimuthal F_θ direction, and the pitching moment about the blade's quarter-chord $M_{1/4}$ (figure 1.2). The total force applied to the blade is computed by combining the two shear forces: $F_{\text{tot}} = \sqrt{F_R^2 + F_\theta^2}$. All force coefficients are non-dimensionalised by the blade chord c , the blade span s , and the blade velocity $U_b = \omega R$ such that:

$$C_{\text{tot/R}/\theta} = \frac{F_{\text{tot/R}/\theta}}{0.5\rho U_b^2 s c} .$$

The subscripts tot, R, or θ refer to the total force, the radial, or the tangential force component.

4.2.3 Particle image velocimetry

High-speed particle image velocimetry (PIV) was used to measure the flow field around the wind turbine blade. A dual oscillator diode pumped ND:YLF laser ($\lambda = 527 \text{ nm}$) with a maximum pulse energy of 30 mJ and a beam splitter were used to create two laser sheets from opposite sides of the channel. The light sheets were oriented horizontally at mid-span of the turbine blade (figure 4.1). A high speed camera with a sensor size of $1024 \text{ px} \times 1024 \text{ px}$ (Photron Fastcam SA-X2) and a spinning mirror apparatus were installed below the channel to capture the flow around the blade. The spinning mirror apparatus allows us to measure

Chapter 4. The dynamic stall dilemma

the velocity field around the blade with a higher spatial resolution and without scarifying the temporal resolution. The field of view is $2.5c \times 2.5c$ centred around the blade. The acquisition frequency is 1000 Hz. The images were processed following standard procedures using a multi grid algorithm [85]. The final window size was $48 \text{ px} \times 48 \text{ px}$ with an overlap of 75 %. This yields a grid spacing or physical resolution of $1.7 \text{ mm} = 0.029c$.

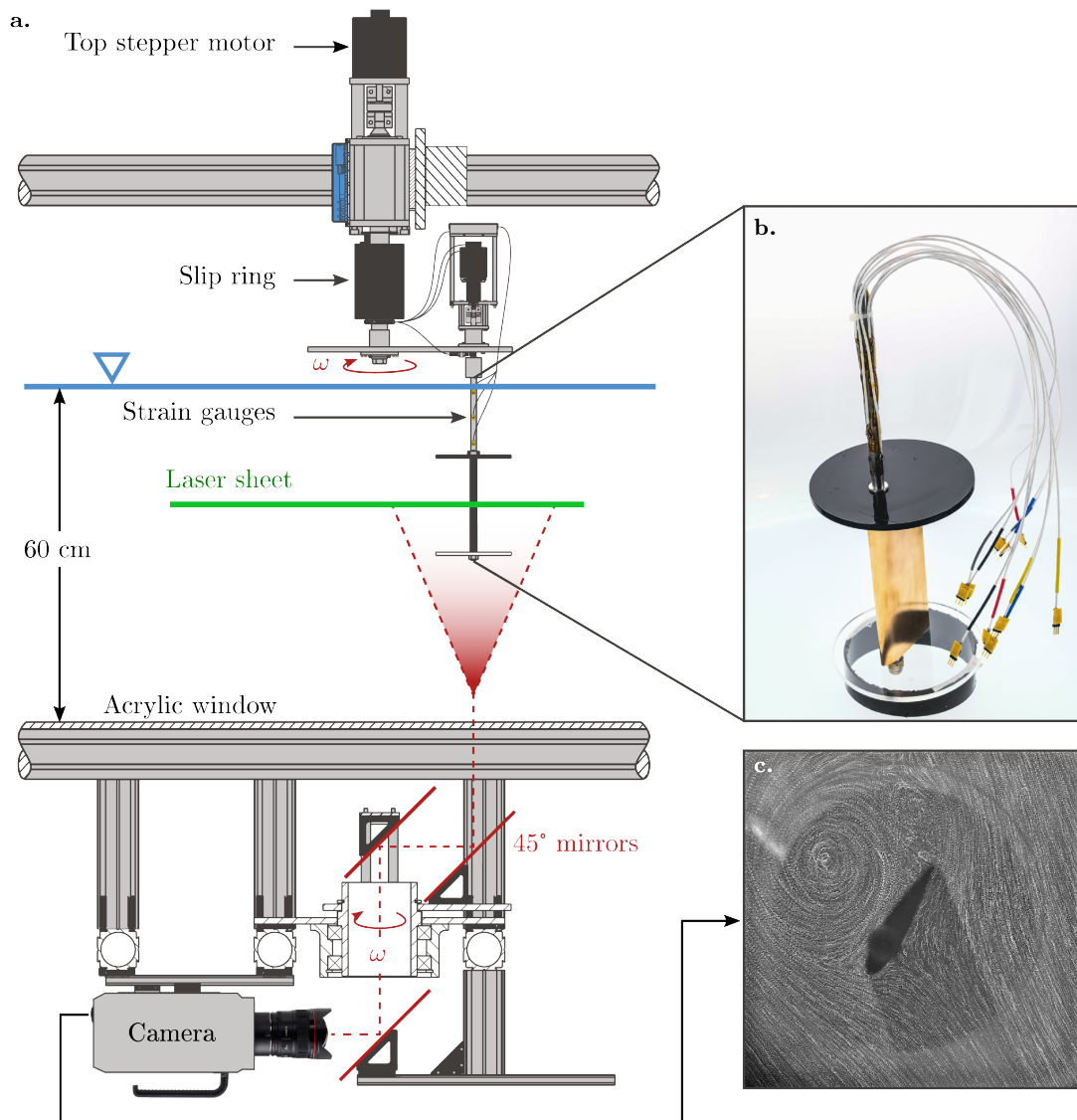


Figure 4.1: (a) Cross-sectional view of the experimental set-up at the test-section's mid-span, including the wind turbine model, the light sheet, the rotating mirror system, and the high-speed camera for particle image velocimetry. The turbine model and camera were not sectioned for clarity. (b) A close-up view of the blade sub-assembly, with installed strain gauges. (c) The camera's field of view indicated by a long exposure image of seeding particles in the flow.

4.3 Results

The temporal evolution of the effective angle of attack α_{eff} , effective flow velocity U_{eff} , and the phase-averaged total force coefficient C_{tot} experienced by the wind turbine blade operating at the tip-speed ratio $\lambda = 1.5$ are presented in figure 4.2. The blade's progression along its circular path relative to the incoming flow during one turbine rotation T is depicted at the top of the figure. The phase-averaged vorticity and velocity fields at eight selected points of interest (a)-(h) are shown at the bottom of figure 4.2. The velocity field is captured in the blade's frame of reference, so it shows the effective flow conditions acting on the blade.

At the beginning of the blade's revolution ($t/T = 0$), the blade sees the incoming flow under a zero angle of attack and the flow around the blade is attached (figure 4.2(a)). The small total force experience by the blade is attributed to unsteady aerodynamic effects caused by the high change in the blades' angle of attack or pitch rate at $t/T = 0$ [10]. During the initial part of the rotation, the angle of attack is positive and increases gradually until it reaches a maximum value of $\alpha_{\text{eff}} = 42$ at $t/T = 0.37$. At $t/T = 0.09$, the angle of attack exceeds the critical static stall angle of $\alpha_{\text{ss}} = 13.1^\circ$ that was determined for the turbine's blade at $Re = 50k$ using the procedure described in chapter 2. Shortly after the blade's angle of attack has exceeded its static stall value, vorticity starts to accumulate near the leading edge (figure 4.2(b)) and forms a coherent leading edge or dynamic stall vortex (figure 4.2(c)).

During the formation of the dynamic stall vortex, the total force coefficient increases approximately linearly with time from $C_{\text{tot}} = 0.5$ to $C_{\text{tot}} \approx 4$ within a quarter of the rotation period. This maximum value of the total force coefficient is well beyond the values that we observe for this airfoil under static conditions. This lift overshoot is a characteristic feature of dynamic stall. The decrease of the total force coefficient for $t/T > 0.24$ is linked to the lift-off of the dynamic stall vortex away from the airfoil's surface and the emergence of positive or opposite-signed vorticity between the vortex and the surface.

After lift-off, the dynamic stall vortex continues to grow and reaches a size that is of the order of the blade's chord length (figure 4.2(d)). Opposite sign vorticity has now spread across the entire chord length and leads to a loss of suction on the airfoil's surface and a drop in the total force coefficient. The total force coefficient drops even faster when the angle of attack starts to decrease for $t/T > 0.38$. During this part of the cycle ($0.38 < t/T < 0.5$), the large scale dynamic stall vortex loses coherence and the vorticity dissipates (figure 4.2(d,e)).

When the blade enters the second half of its rotation, the blade is surrounded by a heavily separated flow and the remnants of the dynamic stall vortex that is convected downstream (figure 4.2(e)). The blade now also moves in the downstream direction and continues to interact with its own wake until $t/T \approx 0.6$. This contributes to a further drop in the force coefficient to almost zero. The local minimum of the force coefficient coincides with the moment at which the effective angle of attack has reached its maximum negative value.

For the remainder of the cycle, the suction side of the blade is now on the outside of the circular trajectory where positive vorticity accumulates (figure 4.2(f)). This vorticity accumulates into a vortex that is stretched along the chord length and gives raise a local force maximum $C_{\text{tot}} = 1.1$

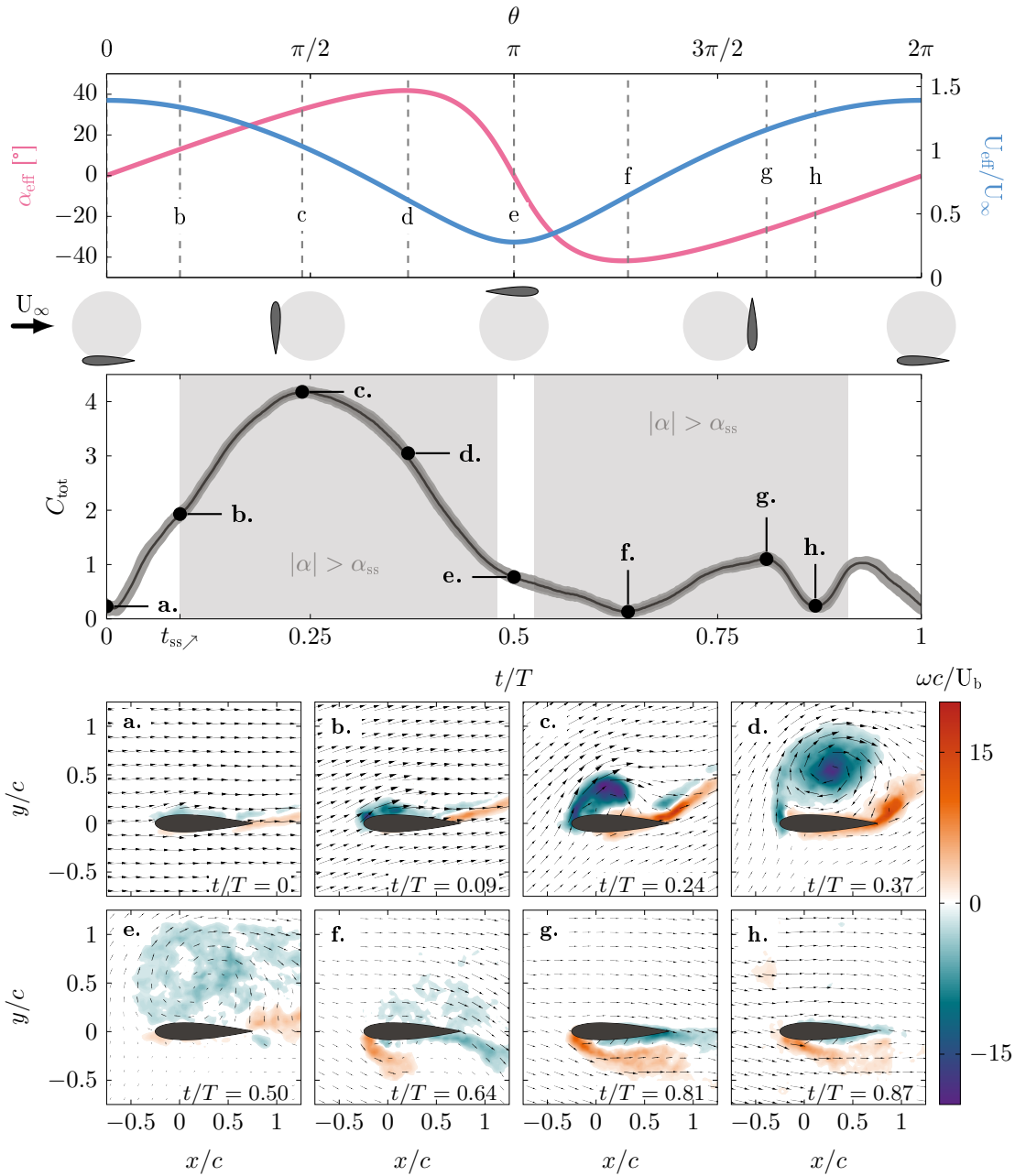


Figure 4.2: Temporal evolution of the effective angle of attack α_{eff} , effective flow velocity U_{eff} , and total force coefficient C_{tot} experienced by the wind turbine blade operating at the tip-speed ratio $\lambda = 1.5$. The blade's progression along its circular path relative to the incoming flow is depicted at the top of the figure. Phase-averaged vorticity and velocity fields at eight points of interest (a)-(h). The flow fields are rotated in the frame of reference of the blades. The vectors show the direction of the incoming flow and their relative lengths match the relative spatiotemporal differences in the velocity magnitude.

at $t/T = 0.8$ (figure 4.2(g)). This vortex does not have much time to grow and is convected downstream when the absolute value of the effective angle of attack decreases and the flow reattaches along both sides of the blade (figure 4.2(h,a)).

The blade kinematics α_{eff} and U_{eff} , phase-averaged total force coefficient C_{tot} and flow fields for the tip-speed ratio $\lambda = 3.0$ are presented in figure 4.3 for comparison. The main differences with the previously described development at $\lambda = 1.5$ are a lower total force magnitude, the smaller size of the dynamic stall vortex and a reduction in post-stall fluctuations. The total force magnitude in the upwind half of the blade's rotation ($0 \leq t/T < 0.5$) is 2.5 times smaller for $\lambda = 3.0$ compared to $\lambda = 1.5$ due to the lower pitching and surging amplitude experienced by the blade operating at $\lambda = 3.0$. The dynamic stall vortex that forms during the upwind half of the cycle at $\lambda = 3.0$ is much smaller and less coherent than the vortex formed at $\lambda = 1.5$. For $\lambda = 3.0$, the dynamic stall vortex does not cover more than half of the chord length (figure 4.3a-d). The portion of the cycle that is influenced by the interaction of the blade with the shed dynamic stall vortex is significantly reduced and the flow reattaches early in the downwind half of the rotation (figure 4.3f-h). In general, we observed less load fluctuations and a more symmetric load response for the first and second half of the rotation for higher tip-speed ratios. When the tip-speed ratio decreases towards 1, the blade's effective flow condition see larger periodic oscillations, leading to more dominant dynamic stall events, greater force production, and larger post-stall load transient.

The power production of vertical axis wind turbines is directly proportional to the force component tangential to the blade. The temporal evolutions of the tangential force coefficient C_{θ} experienced by the wind turbine blade operating at tip-speed ratios ranging from 1.2 to 6 are presented in figure 4.4(a). At a high tip-speed ratios ($\lambda \geq 4.5$), the blade experiences almost no tangential force during the entire rotation. For mid and low tip-speed ratios ($\lambda < 4.5$), the tangential force coefficient features a distinct peak in the upwind half that increases in magnitude (figure 4.4(b)) with decreasing tip-speed ratio (figure 4.4(b)).

The maximum tangential force coefficient increases from 0.24 at $\lambda = 3$ to 0.35 at $\lambda = 2.5$. In this range of tip-speed ratios, positive tangential force is mainly observed in the second part of the upwind part of the rotation and is attributed to the presence of a dynamic stall vortex (figure 4.3(d)). If we further reduce the tip-speed ratio, a stronger dynamic stall vortex is observed, which starts to form earlier in the cycle (figure 4.2(c) vs figure 4.3(d)). This results in a strong increase in the maximum tangential force from 0.35 at $\lambda = 2.5$ to 1.2 at $\lambda = 1.2$. The peak tangential force occurs earlier in the cycle the lower the tip-speed ratio. For $\lambda < 2.2$, the peak is followed by a significant drop and excursion in negative values (figure 4.4(a)). Negative tangential force is equivalent to negative instantaneous torque generated by the blade and is undesirable for a vertical-axis wind turbine.

The variation in the maximum tangential force coefficient with tip-speed ratio follows a bi-linear evolution with a transition point around $\lambda = 2.5$. The transition point corresponds to the conditions for which the maximum tangential force coefficient occurs at the maximum angle of attack and marks a fundamental shift in the unsteady blade load response (figure 4.4(d)). For $\lambda > 2.2$, the tangential force evolution follows the blade kinematics and the force maximum is

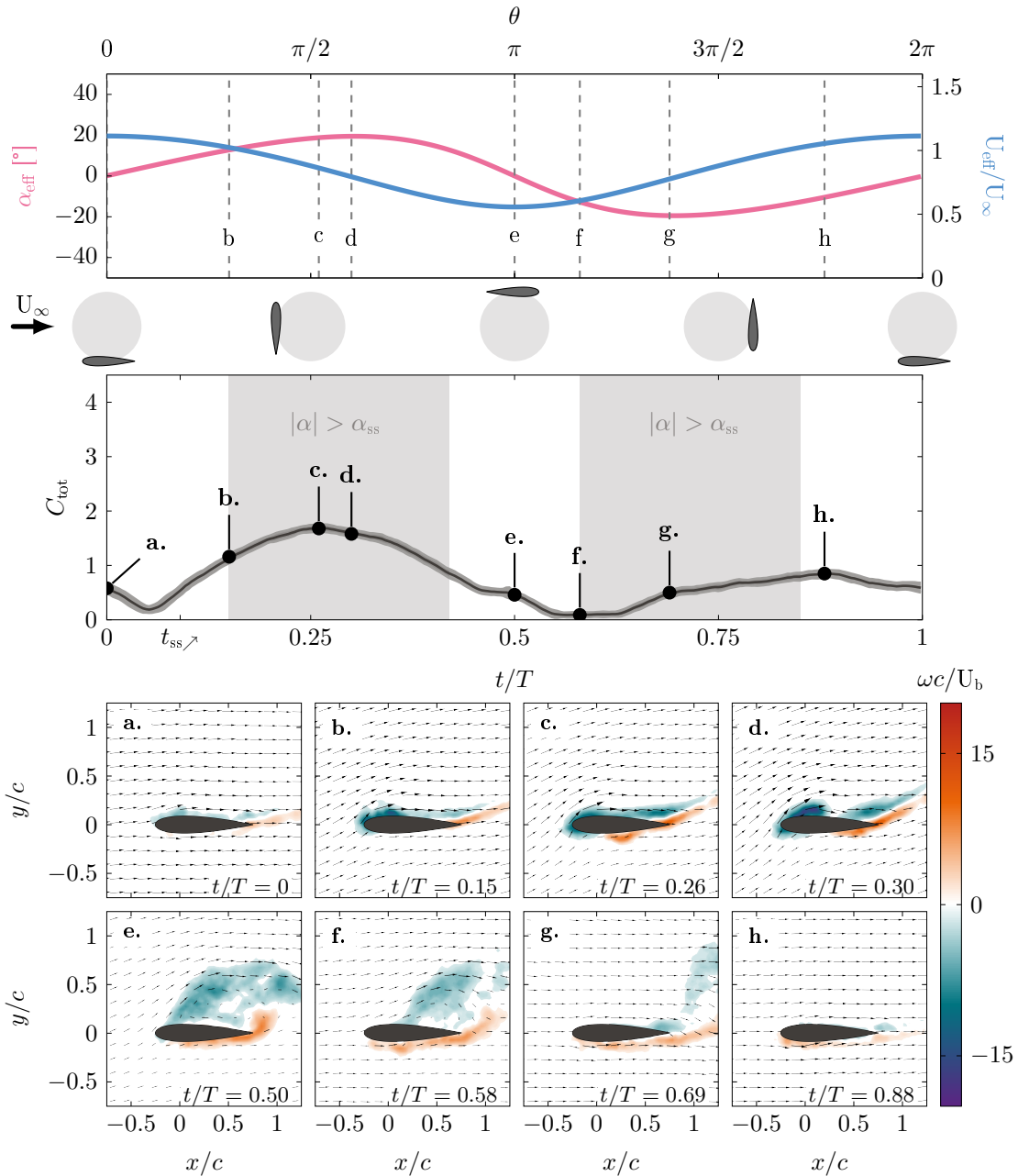


Figure 4.3: Temporal evolution of the effective angle of attack α_{eff} , effective flow velocity U_{eff} , and total force coefficient C_{tot} experienced by the wind turbine blade operating at the tip-speed ratio $\lambda = 3.0$. The blade's progression along its circular path relative to the incoming flow is depicted at the top of the figure. Phase-averaged vorticity and velocity fields at eight points of interest (a)-(h). The flow fields are rotated in the frame of reference of the blades. The vectors show the direction of the incoming flow and their relative lengths match the relative spatiotemporal differences in the velocity magnitude.

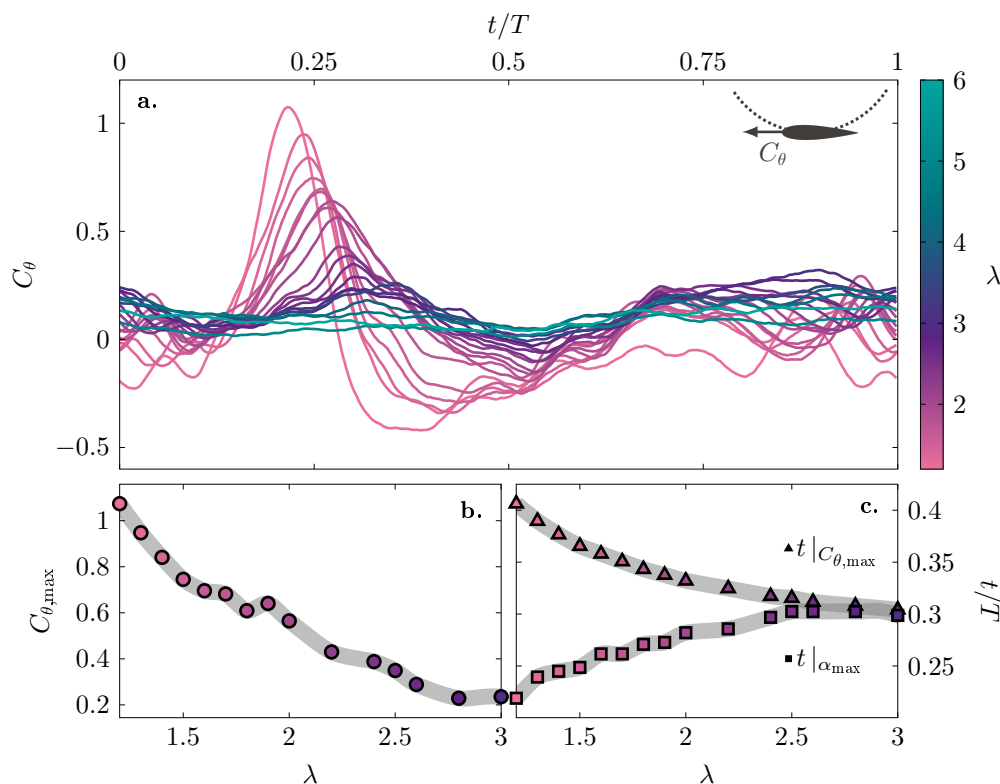


Figure 4.4: (a) Temporal evolution of the tangential force coefficient C_θ experienced by the wind turbine blade operating at tip-speed ratios ranging from 1.2 to 6. (b) Maximum values of the tangential force coefficient as a function of the tip-speed ratio. (c) Temporal occurrence of the tangential force maximum $t|_{C_{\theta,\max}}$ and temporal occurrence of the maximum angle of attack $t|_{\alpha_{\max}}$ as a function of the tip-speed ratio. We focus on tip speed ratio $\lambda \in [1.2 - 3]$ as they have a clearly defined maximum that can readily be identified.

governed by α_{\max} . For $\lambda < 2.2$, the tangential force evolution does not purely follow the blade kinematics anymore and is strongly affected by the occurrence of dynamic stall. This leads to a strong increase in the tangential force overshoot with decreasing tip-speed ratio but also an increase in the force fluctuations following the separation of the dynamic stall vortex.

To further evaluate the influence of dynamic stall on the tangential force coefficient, we analyse the temporal evolution of the circulation around the blade for five tip-speed ratio cases $\lambda = 1.2, 1.5, 2.0, 2.5, 3.0$ in figure 4.5. The circulation was computed by integrating all the phase-average vorticity in the entire field of view surrounding the blade. The circulation values were non-dimensionalised by the blade velocity and chord length. The absolute value of the normalised circulation is zero at the start of the upwind rotation and starts increasing approximately linearly in time with increasing rate for decreasing tip-speed ratios. The end of the linear increase region corresponds to the moment when the maximum tangential force is reached. At this point, the flow features a coherent leading-edge dynamic stall vortex which increases in size and strength with decreasing tip-speed ratio figure 4.5(a-d).

The absolute normalised circulation taken at the moment when the maximum tangential force coefficient is reached $\Gamma / cU_b @ C_{\theta,\max}$ is presented versus the maximum tangential force coefficient in figure 4.5(ii). A higher maximum tangential force coefficient is directly related

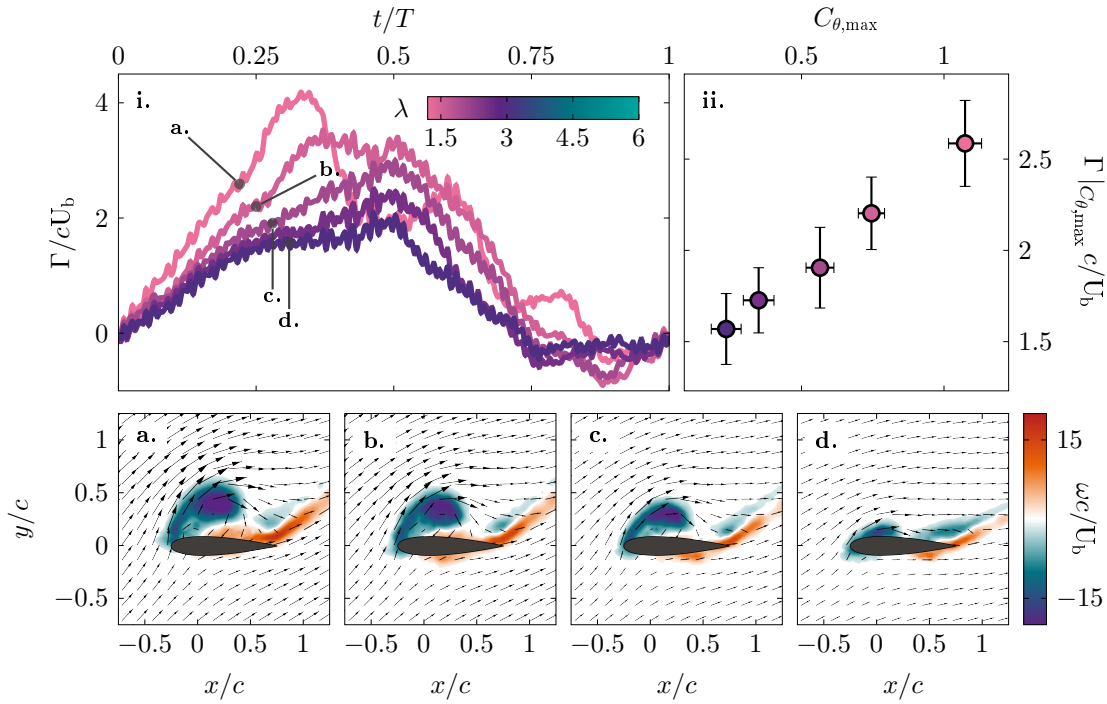


Figure 4.5: (i) Normalised circulation around the turbine blade against normalised time for tip-speed ratios $\lambda = 1.2, 1.5, 2.0, 2.5, 3.0$. (ii) Absolute normalised circulation taken at the moment when the maximum tangential force is reached ($\Gamma|_{C_{\theta,\max}}/cU_b$) against maximum tangential force coefficient $C_{\theta,\max}$. (a-d) Phase-averaged velocity and vorticity snapshots selected at times shown in (i).

to a stronger dynamic stall vortex figure 4.5(ii). This stronger dynamic stall vortex has also formed quicker than at lower tip speed ratios. The snapshots in figure 4.5(a-d) present the vortex at the moment in the cycle when the maximum tangential force is reached which occurs earlier for lower tip-speed ratios. From left to right, the time at which the snapshots are taken increases but we seem to be looking at the formation process of the vortex in reversed time. This highlights the importance of various time scales that play a role in the flow and force response on vertical-axis wind turbine blades.

After the maximum in tangential force coefficient is reached, the circulation associated with the dynamic stall vortex continues to increase. The blade is now in the second half of the upwind rotation, it is moving along the direction of the incoming flow and experiences a decreasing effective velocity. As a result, the vorticity feeding rate of the dynamic stall vortex decreases and the vortex lifts-off from the surface. Vortex lift-off occurs when the vortex has grown strong enough such that secondary vortices of opposite-signed vorticity emerge between the vortex and the blade's surface (figure 4.5(a)) or when the effective inflow velocity decreases and drops below the self-induced velocity of the vortex [56, 90]. Even though the dynamic stall vortex and the circulation in the field of view continues to increase for $0.25 \leq t/T < 0.4$, the tangential force coefficient drops as the vortex is no longer bound to the blade. The drop in the tangential force is followed by undesirable load transients that increase structural stress, lead to potentially vibrations, and sometimes even turbine failure. Here, we will now propose and present two methods to quantify these undesirable load fluctuations.

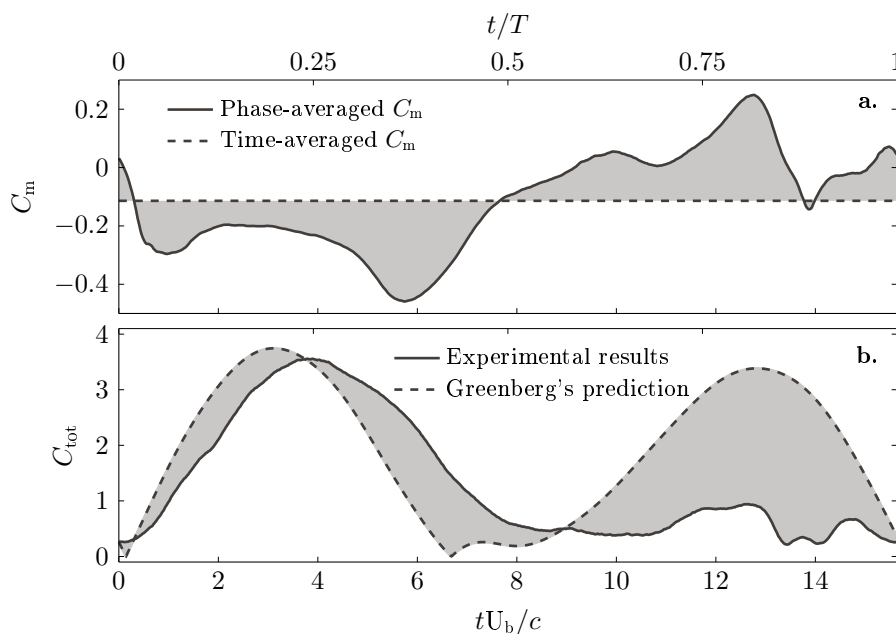


Figure 4.6: Proposed quantities to assess the magnitude of stall induced load transients based on (a) the phase-averaged pitching moment standard deviation; (b) the different between the phase-averaged total force coefficient C_{tot} and the inviscid solution obtained using an adapted Greenberg model from [10]. Examples include data for $\lambda = 1.5$ and $\lambda = 1.7$.

The first method consists of quantifying the standard deviation of the phase-averaged pitching moment acting on the blade (figure 4.6(a)). By definition, the pitching moment about the airfoil's aerodynamic centre is independent of the angle of attack. For a NACA0018, the aerodynamic centre is close to the quarter-chord. An increase in the standard deviation of the measured pitching moment serves as a measure of the extent of flow separation occurring on the blade. The pitching moment is also directly related to the torsional stress applied to the blade shaft. Significant transients of this metric are undesirable from a turbine structural integrity perspective.

The second method consists of computing the mean difference between the total phase-averaged force experienced by the blade and the total force computed using Greenberg's model ΔC_{total} (figure 4.6(b)). Greenberg's model is an inviscid flow model that is used to predict the unsteady aerodynamic loads acting on a blade placed in a free-stream and undergoing any combination of oscillatory pitching, surging, and heaving [45]. Greenberg's model was adapted here to accommodate the kinematics experienced by a wind turbine blade following the approach described by [10]. The Greenberg model does not account for vorticity-induced loads related to flow separation. The model also does not account for the fact that the blade follows a circular path which gives rise to apparent camber effects [12]. Large differences between the experimental loads and the inviscid solution indicate an increased influence of flow separation and blade-wake-interactions.

The phase-averaged pitching moment standard deviation and the mean difference in total force coefficient between experimental and theoretical results are presented in figure 4.7.

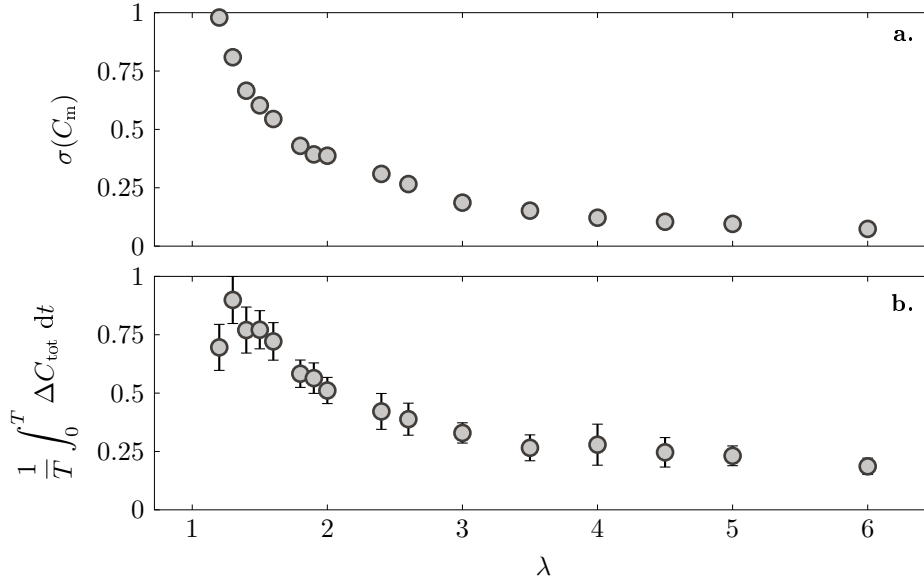


Figure 4.7: (a) Phase-averaged pitching moment standard deviation and (b) mean difference between the total force coefficient from experiments and the total force coefficient computed using the adapted Greenberg model from [10].

Both metrics are normalised by the maximum value achieved over this range of tip-speed ratios to facilitate comparison. The load fluctuations related to flow separation decrease with increasing tip-speed ratio following a power law decay. The phase-averaged pitching moment standard deviation is largest for the lowest tip-speed ratio ($\lambda = 1.2$). The pitching moment standard deviation decreases from 0.90 to 0.15 for the tip-speed ratio increasing from 1.2 to 3.0. The difference between the experimentally measured total load and the inviscid solution follows a similar trend as the pitching moment standard deviation. Both metrics are quick and easy to compute from instantaneous load measurements which makes them suitable metrics to use for future applications of flow control and closed loop performance optimisation.

Based on the temporal evolution of the torque production, flow structures, and load transients, we can distinguish three operating regimes for vertical-axis wind turbines: a regime where no stall occurs, and regimes that are characterised by light or deep dynamic stall. A parametric dynamic stall map indicating which regime a wind turbine is expected to operate in as a function of the tip-speed ratio and the chord-to-diameter ratio is desirable. To determine a robust criterion allowing for the classification of the different tip-speed ratios, we revert to the pitching-moment coefficient around the blade's quarter-chord. The temporal evolutions of the pitching moment coefficient during one turbine revolution at tip-speed ratios $\lambda \in \{1.2, 1.5, 2, 3\}$ are presented in figure 4.8(i). For all tip-speed ratios, we observe a minimum or negative peak pitching moment in the upwind part of the rotation. When the dynamic stall vortex forms and grows, it increases the suction at the leading edge, leading to a nose-down, i.e. negative, pitching moment (figure 4.8(i)). Once the feeding shear layer of the dynamic stall vortex is interrupted by opposite-signed vorticity close to the surface, the vortex is considered to be separated. The separation or pinch-off of the primary stall vortex marks the onset of dynamic stall and is followed by the recovery of the pitching moment (figure 4.8(a-d)). The minimum

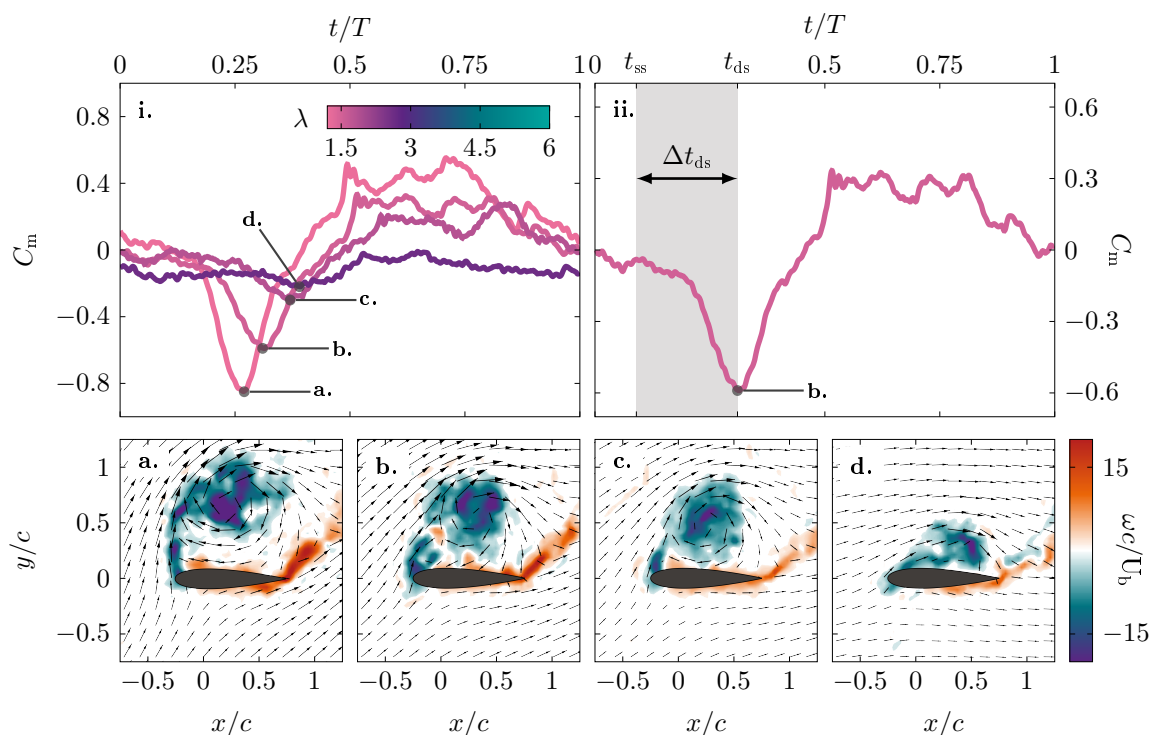


Figure 4.8: (i) Temporal evolution of the pitching moment coefficient for one blade rotation at tip-speed ratios $\lambda \in \{1.2, 1.5, 2, 3\}$; (ii) illustration of the definition and calculation of the dynamic stall delay; (a-d) instantaneous velocity and vorticity snapshots at vortex pinch-off, corresponding to the minimum pitching moment coefficient, for tip-speed ratios of (a) $\lambda = 1.2$, (b) $\lambda = 1.5$, (c) $\lambda = 2$, (d) $\lambda = 3$.

pitching moment coincides here with the leading-edge vortex separation and can be used as a reference to calculate the dynamic stall delay, previously referred to as the reaction delay $\Delta t_{c, \text{reaction}}$ in chapter 2.

The dynamic stall delay is an important timescale for modelling the dynamic stall load response [5]. The stall delay is defined as the time interval between the moment when the blade exceeds its critical static stall angle of attack t_{ss} and the onset of dynamic stall t_{ds} (figure 4.8(ii)). The non-dimensionalised dynamic stall delay follows a universal behaviour governed by the reduced pitch rate, which is largely independent from airfoil shape, motion kinematics, or Reynolds number [5, 60]. We computed the dynamic stall delay for all wind turbine experiments where the blade exceeds its static stall angle, which is for tip-speed ratios $\lambda \in [1.2 - 4]$. For wind turbine blades, the dynamic stall delay is calculated in terms of the airfoil's convective time scale $\int_{t_{ss}}^{t_{ds}} U_{\text{eff}}/c dt$, as shown in [29]. We considered the pitch rate acting on the blade when it exceeds its static stall angle $\dot{\alpha}_{ss}$ to determine the reduced frequency, such that $k = \dot{\alpha}_{ss} c / 2U_b$.

The wind turbine dynamic stall delay is presented as a function of the reduced frequency in figure 4.9. The wind turbine results are compared to the general behaviour observed for four other dynamic stall experiments: linear ramp-up motions of a NACA0018 at $Re = 7.5 \times 10^4$ [60], a sinusoidally pitching NACA0015 at $Re = 5.5 \times 10^5$ [46], a sinusoidally pitching 0A209 at $Re = 9.2 \times 10^5$ [78], and one data point extracted from the single-bladed vertical-axis wind

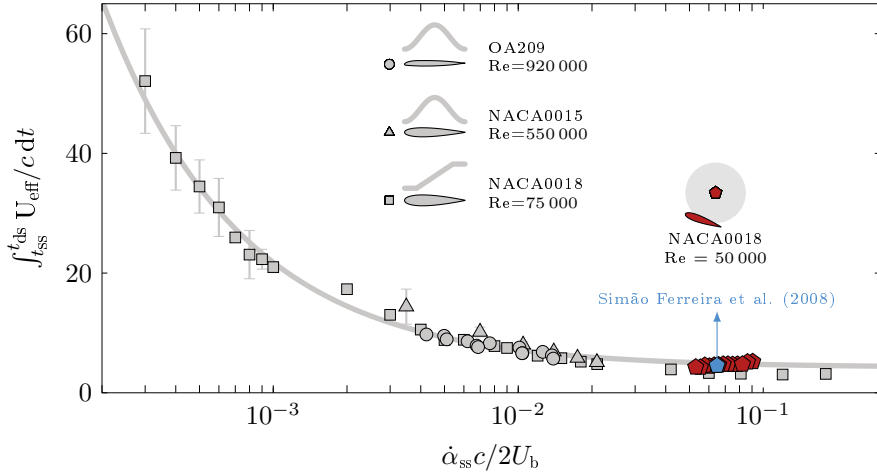


Figure 4.9: Dynamic stall delay Δt_{ds} as a function of the reduced frequency for the vertical-axis wind turbine operating at $\lambda \in [1.2 - 4]$. The results for the wind turbine blade are compared to those obtained for three other dynamic stall experiments: linear ramp-up motions of a NACA0018 at $Re = 7.5 \times 10^4$, a sinusoidally pitching NACA0015 at $Re = 5.5 \times 10^5$ [46], a sinusoidally pitching OA209 at $Re = 9.2 \times 10^5$ [78], and one data point extracted from the single-bladed vertical-axis wind turbine data by [97].

turbine data by Simão Ferreira et al. [97]. The wind turbine dynamic stall delay falls on the same power law decay as the result of the non-rotating dynamic stall data and reaches the same values as the rotating data from [97]. The agreement of vertical-axis wind turbine dynamic stall delay with different kinematics, airfoils, and Reynolds number suggests that the dynamic stall delay universality can be extended to pitching kinematics that include a surging component and a non-linear path. Furthermore, the dynamic stall delay can be used as a criterion to categorise the turbine's operation into one of three regimes: no stall, light stall, and deep dynamic stall.

We can predict whether the blade will undergo deep stall, light stall or no stall by comparing the expected dynamic stall delay with the actual time interval available for dynamic stall to occur for a given turbine geometry and tip-speed ratio. Deep dynamic stall will occur when the dynamic stall onset occurs before the maximum effective angle of attack is reached [78]. Vertical-axis wind turbine kinematics that yield a time interval between the moment the blade exceeds its static stall angle and when the moment it reaches its maximum effective angle that is longer than 4.5 convective ($\int_{t_{SS}}^{t_{ds}} U_{eff}/c dt > 4.5$) are expected to experience deep dynamic stall.

A theoretical parametric dynamic stall regime map is presented in figure 4.10. This map was computed based on the theoretical timescales of turbine blade kinematics obtained for a wide range of tip-speed ratios λ and chord-to-diameter c/D . For each operating condition, we compute the available time for vortex formation as the time difference between the moment when the blade exceeds its critical static stall angle of attack t_{ss} and the moment the maximum effective angle of attack is reached $t|_{\alpha_{max}}$. We calculate an excess convective time beyond the minimum required dynamic stall delay or vortex formation convective time as $\int_{t_{SS}}^{t|_{\alpha_{max}}} U_{eff}/c dt$ with the average dynamic stall delay of 4.5 required for highly unsteady motions (figure 4.9). Negative values of the excess time indicate operating conditions where the dynamic stall

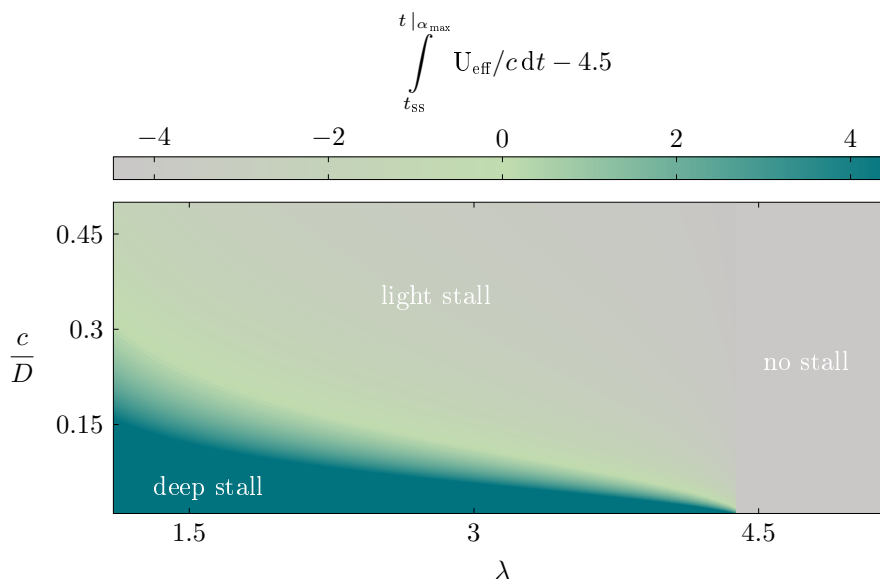


Figure 4.10: Theoretical parametric dynamic stall regime map based on the timescales of the turbine blade kinematics and the characteristic timescales of dynamic stall development. The difference between the available convective time for stall development and the expected dynamic stall delay for a given combination of the chord-to-diameter ratio c/D and tip-speed ratio λ is colour-coded and highlight the deep and light dynamic stall regimes. The no-stall regime indicates operating conditions for which the blade does not exceed its static stall.

vortex formation is interrupted by the change in sign of the effective pitch rate of the blade kinematics. When the blade's effective angle of attack decreases, the leading-edge vortex is forced to pinch-off before it has grown to its full size and strength. These conditions are known as light stall conditions. Vertical-axis wind turbines operating with $\lambda > 4.5$ are shown in grey as the blade does not exceed its static stall, measured to be $\alpha_{ss} = 13.1^\circ$. The boundary between light and deep dynamic stall is not very sensitive to the exact choice of the static stall angle, as the timescales vary only slightly for a small change in angle at high reduced frequencies. Note that this map does not account for blade-wake interactions arising from the presence of other blades. The map is also designed to diagnose the upwind half of the turbine rotation ($0 \leq t/T < 0.5$). During the downwind half ($0.5 \leq t/T < 1$), the blade may interact with previously formed wakes (figure 4.2(e-h)). These wake interaction can trigger the onset of flow separation even if the critical stall angle is not exceeded. These effects are not included in figure 4.10.

To summarise our findings, we show the evolution of the mean power coefficient $\overline{C_p}$ against tip-speed ratio in figure 4.11. The power coefficient increases from $C_p = 0.07$ at $\lambda = 1.5$ to $C_p = 0.28$ at $\lambda = 3.2$. A further increase in tip-speed ratio results in a rapid decrease in power coefficient, which become negative for $\lambda > 4.2$. A negative mean power coefficient is only possible for a motor-driven turbine and represents unrealistic turbine operating conditions. The theoretical stall regime regions show excellent agreement with the power coefficient's evolution across tip-speed ratios. A change in stall regime seems to provoke a sudden change in the mean power coefficient. The transition from deep to light stall leads to a significant increase in power coefficient, while the transition from light stall to no stall causes the mean power coefficient to become negative.

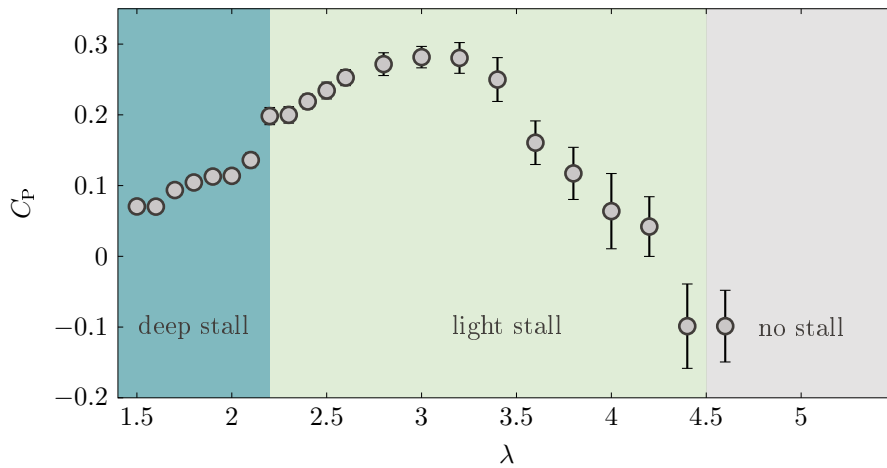


Figure 4.11: Power coefficient against tip-speed ratio for a single-blade wind turbine model. The expected theoretical stall regimes are shown in the background.

At low tip-speed ratios ($\lambda < 2.2$ for $c/D = 0.2$), vertical-axis wind turbines could achieve the highest power production and might seem attractive at first. The blade experiences a significant peak in thrust (positive C_θ) in the first quarter of the rotation ($0 \leq t/T < 0.25$), which is followed by large excursions in drag (negative C_θ) in the post-stall regime ($0.3 \leq t/T < 0.8$). This range of operating conditions is characterised by the formation of a large and coherent dynamic stall vortex, which interacts with the blade over an extended period of time when it convects downstream along the blade's path at the overlap between the upwind and downwind part of the rotation. Prolonged blade-wake interaction is very detrimental to the blade's torque production and yields low mean power coefficients for deep stall tip-speed ratios (figure 4.11). Massive flow separation and blade-vortex interaction lead to important load variations that might challenge the structural integrity of the wind turbine and decreases the appeal of low tip-speed ratio regime.

At intermediate tip-speed ratios ($2.2 \leq \lambda < 4.5$ for $c/D = 0.2$), the main torque production ($C_\theta > 0$) occurs partly during upwind ($0.15 \leq t/T < 0.5$), but also partly during downwind ($0.6 \leq t/T < 1$), as the turbine blade has time to recover from the light dynamic stall event that occurs during the upwind part of the motion. The leading-edge vortex is smaller in size and strength than at low tip-speed ratios and is shed from the blade before it has the change to grow to its full capacity, as the blade starts to pitching down less than three convective times after the blade has exceeded its static stall angle. The load transients related to flow separation for intermediate tip-speed ratios are 75 % lower than at low tip-speed ratios. The power coefficient peaks for light stall tip-speed ratios around $\lambda = 3.1$ (figure 4.11).

At high tip-speed ratios ($4.5 \leq \lambda$ for $c/D = 0.2$), the production of torque is significantly reduces and there is no vortex formation on the blade ($\alpha < \alpha_{ss}$). Vortex formation is the main mechanism by which a wind turbine blade generates torque, so high tip-speed ratios yield negative mean power coefficients (figure 4.11).

Light stall tip-speed ratios yield optimal power coefficient and lower stall-related load fluctuations, making this regime the sweet spot for typical vertical-axis wind turbine operation

and the preferred solution to the dynamic stall dilemma. These findings agree with previous studies in literature that found optimal operating conditions to be around a tip-speed ratio $\lambda = 3$ for wind turbines operating under comparable conditions [52, 89, 94].

4.4 Conclusion

Time-resolved force and velocity field measurements were conducted on a scaled-down model of a Darrieus H-type wind turbine operating at a chord-based Reynolds number $Re = 50\,000$, chord-to-diameter ratio $c/D = 0.2$ and tip-speed ratio $\lambda \in [1.2 - 6]$. The development of dynamic stall on a vertical-axis wind turbine was characterised over this comprehensive operational envelope. Vertical-axis wind turbines operating conditions are characterised by the tip-speed ratio λ and chord-to-diameter ratio c/D . Based on the flow and force data, we categorised the response of the wind turbine blade as a function of the operating conditions into three regimes: no stall, light dynamic stall, and deep dynamic stall.

Low tip-speed ratios ($\lambda < 2.2$ at $c/D = 0.2$) achieve a significant peak in torque production around $C_{\theta, \max} = 1.1$ when a dynamic stall vortex grows during the upwind half of the rotation. The maximum tangential force coefficient is directly related to the strength of the dynamic stall vortex and both increase with decreasing tip-speed ratio. When the stall vortex pinches-off before the maximum effective angle of attack is reached at low tip-speed ratios, the blade experiences deep stall which is associated with significant fluctuation of the loads and an asymmetry in the torque production between the upwind and downwind half of the turbine revolution.

At intermediate tip-speed ratios ($2.2 \leq \lambda \leq 4.5$), the maximum angle of attack is reached before the dynamic stall vortex has had enough time to grow to its full potential and the blade experiences light dynamic stall. The formation of the leading-edge vortex is interrupted by the change in pitch rate, yielding a smaller vortex with a 60 % reduction in vortex strength and tangential force maximum compared to the low tip-speed ratio cases. The post-stall load fluctuations are significantly reduced at intermediate tip-speed ratios, with a 75 % reduction in load transients compared to low tip-speed ratios. The turbine blade recovers faster from light stall conditions and achieves a second torque production region in the downwind half of its rotation. Intermediate tip-speed ratios offer a desirable compromise in the dynamic stall dilemma, as they strike a balance between torque production and structural resilience.

At high tip-speed ratios ($\lambda > 4.5$) the blade does not exceed its critical stall angle and dynamic stall does not occur. Future efforts will focus on developing smart active control strategies that would allow us to mitigate stall related load transients and to tap into the high torque production potential at low tip-speed ratios.

5

TIMESCALES OF DYNAMIC STALL DEVELOPMENT

Data-driven models and control strategies that are physics-informed are desirable to improve the efficiency and lifespan of vertical axis wind turbines. Existing models are challenged by the occurrence of dynamic stall because it is an unsteady phenomenon that features some stochasticity. The succession of events and their timescales are well characterised for wings undergoing dynamic stall when subjected to pitching manoeuvres in a steady free stream. In this chapter we present our findings on the characterisation of dynamic stall timescales on a vertical-axis wind turbine blade.

The work presented in this chapter was submitted to Flow [61].

CHAPTER HIGHLIGHTS

- ⊙ We perform parametric proper orthogonal decomposition to identify dominant flow structures that are common to all tip-speed ratios where the blade experiences dynamic stall.
- ⊙ We distinguish and quantify the timespan of six characteristic stall stages: the attached flow, shear-layer growth, vortex formation, upwind stall, downwind stall, and flow reattachment stage.
- ⊙ We demonstrate the aerodynamic loads hold sufficient sensory information to identify the transition between the stall events for closed-loop control applications.
- ⊙ The aerodynamic force completes over 60 % of its work during vortex formation, which underlines the importance of managing dynamic stall on vertical-axis wind turbines.

5.1 Introduction

Vertical-axis wind turbines typically experience flow separation on their blades, even at design operating conditions. Coherent accumulation of vorticity at the blade's leading edge is the main mechanism by which turbine blades generate torque. The shedding of vorticity from the blade, however, can cause undesired load fluctuations and structural damage. The severity of vortex shedding events increases for decreasing tip-speed ratios. The tip-speed ratio is considered low when the turbine blade exceeds its static stall angle for longer than 4.5 convective times, corresponding to the minimum amount of time required for a coherent leading-edge vortex to form chapters 2 and 4. Vertical-axis wind turbines operating at low tip-speed ratios ($\lambda \leq 2.2$ when $c/D = 0.2$) undergo deep dynamic stall, which is characterised by the formation, growth, and shedding of large-scale coherent vortices [15]. The shedding of large-scale vortices is generally followed by a dramatic loss in aerodynamic efficiency and highly unsteady loads that can potentially lead to turbine failure [19, 72, 77].

The temporal occurrence and landmark stages characterising dynamic stall on two-dimensional pitching airfoils in a steady free-stream flow are well documented [15, 25, 77] and their load responses can be reasonably well modelled [5, 44, 63]. For a rotating wind turbine blade, the occurrence of dynamic stall is affected by the circularity of the blade's path in several ways. The dynamic stall vortex is convected downstream along the blade's path after it is shed, extending the blade-vortex interaction compared to a blade pitching in a steady flow. The flow topology is dominated by the extended presence of a dissipating dynamic stall vortex at the overlap between the upwind and downwind halves of the blade rotation when the effective velocity is at its lowest (figure 1.2) [22, 96]. The flow and wake curvature also influence the effective flow acting on a vertical-axis wind turbine blade, leading to virtual camber and incidence effects [9, 74]. The blade crosses the same stream tube twice, leading to repeated blade-wake interactions even for a single-blade configuration [40, 80]. Typical descriptions of effective flow conditions on a turbine blade, based on inviscid flow theory (equations (1.2) and (1.3)) do not faithfully capture the complexity of the events unfolding during the blade's rotation, even when coupled with an additional induced velocity term [6, 81].

Low-order models, such as the actuator cylinder model, improve the prediction of effective flow conditions and unsteady loads by accounting for the velocity induced to the flow by the presence of a rotating turbine [68]. The absence of a reliable dynamic stall model for vertical-axis wind turbines limits the validity of low-order models for low to intermediate tip-speed ratios [23]. The most widely used dynamic stall models were developed for pitching blades operating in a free stream [44, 63]. These models rely on a sound understanding of landmark timescales that govern the development of flow separation, namely the vortex formation time and vortex shedding frequency [5]. For a vertical-axis wind turbine, the timescales of landmark stall events, such as shear layer roll-up or stall onset, have not yet been characterised. Dynamic stall timescales are crucial parameters in the overall design and modelling of a vertical-axis wind turbine and for more advanced applications such as devising active flow control strategies.

This chapter aims at improving our qualitative and quantitative understanding of the chain of events leading to dynamic stall on a vertical-axis wind turbine blade and the associated timescales. We present time-resolved velocity field and load measurements on a scaled-down H-type Darrieus wind turbine operating in a water channel. A large range of tip-speed ratios is covered to yield a comprehensive characterisation of the occurrence of deep stall on a vertical-axis wind turbine. Proper orthogonal decomposition (POD) is performed on the measured vorticity field to extract the spatial modes and timescales that dominate the development of dynamic stall. Landmark dynamic stall stages and their timescales are extracted by analysing the interplay of the POD time coefficients related to the three most energetic spatial modes. The POD time coefficients indicate the timing of the leading-edge vortex life cycle and other dominant flow features. The timing of the dynamic stall stages is also extracted based solely on the aerodynamic loads by analysing distinct topological changes in the unsteady load response trajectory. The timescale characterisation based on a load response is desirable as it is more feasible in full-size applications than any analysis that requires velocity field measurements. We find a good agreement between the timescales obtained from force measurement with the timescales extracted from the vorticity POD time coefficients.

5.2 Experimental apparatus and methods

The data presented in this chapter was obtained during the same experimental campaign as for chapter 4. For a full description of the experimental apparatus and methods, you may refer to section 4.2. Proper-orthogonal decomposition was performed for the present chapter and our method is described hereafter.

The flow development during a full blade rotation is characterised by significant changes in the flow topology and the formation of vortices when dynamic stall occurs. To identify energetically relevant flow features and their time evolution, we will apply a proper orthogonal decomposition (POD) of the vorticity field. The POD method was introduced to the field of fluid mechanics to identify coherent structures in turbulent flows [66]. The spatial modes ψ_n reveal the dominant and recurring patterns in the data. The corresponding temporal coefficients a_n indicate the dynamic behaviour of the coherent spatial patterns identified in the modes and can be used to extract the characteristic physical timescales of the problem. As the flow under consideration is vortex dominated, we have opted to decompose the vorticity field instead of the velocity field. The POD decomposes the vorticity snapshots at time t_i into a sum of orthonormal spatial modes $\psi_n(x, y)$ and their time coefficients $a_n(t_i)$ such that

$$\omega(x, y, t_i) = \sum_{n=1}^N a_n(t_i) \psi_n(x, y), \quad (5.1)$$

where N is the total number of snapshots. The POD modes ψ_n form an optimal basis, from which the original system can be reconstructed with the least number of modes compared to any other basis [98, 101].

A key aspect of our study is to compare the dominant flow features shared across varying tip-speed ratios and their relative importance for each case. To this purpose, we have

stacked the vorticity fields $\omega^\lambda(x, y, t_i)$ for all tip-speed ratios $\lambda \in [1.2, 1.5, 2, 2.5, 3]$ into a single matrix $\Omega = [\omega^{\lambda=1.2}, \omega^{\lambda=1.5}, \dots, \omega^{\lambda=3}]^T$ for decomposition. The POD of this combined dataset yields the spatial modes $\psi_n(x, y)$, which are common for all cases. The mode coefficient matrix comprises the mode coefficients corresponding to the individual cases $A = [a^{\lambda=1.2}, a^{\lambda=1.5}, \dots, a^{\lambda=3}]$. The POD eigenvalues ζ_n indicate the contribution of each mode n to the total energy of the stacked vorticity fields. They are strictly decreasing as POD ranks the modes according to their energy content. With this approach, the vorticity fields for each tip-speed ratio can be reconstructed based on the same set of spatial modes. The temporal contribution of these common structures to individual tip-speed ratios λ is given by the corresponding temporal coefficients a_n^λ . A vorticity field for a specific $\lambda = \lambda_m$ can be reconstructed as

$$\omega^{\lambda=\lambda_m}(x, y, t_i) = \sum_{n=1}^N a_n^{\lambda=\lambda_m}(t_i) \psi_n(x, y) \quad . \quad (5.2)$$

The energy contribution $\zeta_n^{\lambda=\lambda_m}$ of individual spatial modes $\psi_n(x, y)$ in the tip-speed ratio case $\lambda = \lambda_m$ is computed from the corresponding time coefficients as

$$\zeta_n^{\lambda=\lambda_m} = \langle a_n^{\lambda=\lambda_m}, a_n^{\lambda=\lambda_m} \rangle = \frac{1}{N_t} \sum_{i=1}^{N_t} \left(a_n^{\lambda=\lambda_m}(t_i) \right)^2 \quad , \quad (5.3)$$

where N_t is the number of snapshots considered for the individual tip-speed cases. Here, we used the same number of snapshots $N_t = 200$ for each tip-speed ratio. The procedure used here is similar to the parametric modal decomposition presented by [18].

5.3 Results

The temporal evolution of the phase-averaged power coefficient for a wind turbine operating at tip-speed ratio $\lambda = 1.5$ is shown as a polar plot in figure 5.1. In a polar plot, a radial increase of the plotted line indicates an increase in power coefficient C_p . The central circle represents the $C_p = 0$ level. The azimuthal progression of the line represents time, plotted according to our usual convention for wind turbine blades (figure 1.2). The interplay between the power coefficient and the flow structures forming around the wind turbine blade is highlighted with phase-average vorticity fields presented throughout the blade's rotation. The total aerodynamic force orientation and relative magnitude are represented by an arrow starting from the blade's quarter-chord.

When the blade is facing the wind ($\theta = 0^\circ$), the flow is attached and vorticity is only present in the blade's wake. The total force is small but increases rapidly when the blade moves upwind. At $\theta = 33^\circ$, the blade's effective angle of attack exceeds its critical static stall angle and flow reversal emerges on the suction side of the blade. The shear layer rolls up to form a coherent dynamic stall vortex at the leading edge of the blade. The presence of this leading-edge dynamic stall vortex causes the power coefficient to rise from -0.03 at $\theta = 0^\circ$ to its maximum value of 0.32 at $\theta = 77^\circ$. Thereafter, the dynamic stall vortex continues to grow in size and strength and it moves from the leading edge towards the mid-chord position. This migration redirects the aerodynamic force in the radial direction and the power coefficient rapidly drops

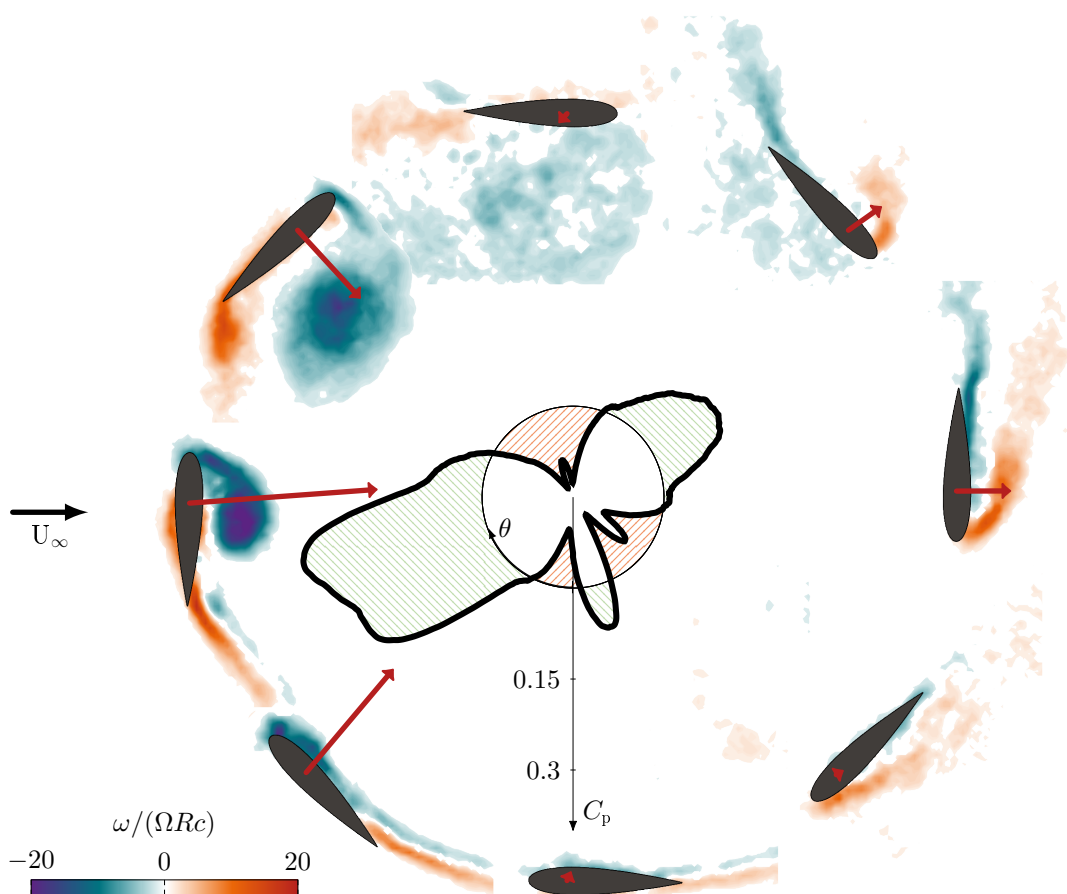
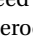
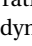


Figure 5.1: Polar plot of the temporal evolution of the phase-averaged power coefficient C_p for a vertical-axis wind turbine operating at tip-speed ratio $\lambda = 1.5$. Phase-averaged normalised vorticity fields are shown throughout the blade's rotation. The total aerodynamic force acting on the blade at the various azimuthal locations is depicted by arrows starting from the blade's quarter-chord. The length of the arrows indicates the relative magnitude of the force. The hatched regions  and  represent regions of torque generation and dissipation respectively.

when the vortex detaches from the blade around $\theta = 114^\circ$. After lift-off, the dissipating vortex is convected downstream along the blade's path. The interaction between the dissipating stall vortex and the turbine blade is detrimental to power production. The power coefficient remains around its minimum value of -0.14 between $\theta = 150^\circ$ and $\theta = 180^\circ$. During the downwind half of the blade's rotation ($180^\circ \leq \theta < 360^\circ$), there is a reversal between the suction and pressure sides of the blade. A second counter-rotating leading-edge vortex now forms on the extrados of the blade's circular path ($\theta = 240^\circ$). This vortex is less coherent and less strong than the one formed during the upwind. It still yields a local maximum in the power coefficient around 0.1. The second leading edge vortex does not remain bound to the blade for long and before we reach $\theta = 270^\circ$, a layer of negative vorticity is entrained between the vortex and the blade surface. The lift-off of the second leading edge vortex leads again to a drop in the power coefficient below 0. The power coefficient reaches a local minimum of -0.07

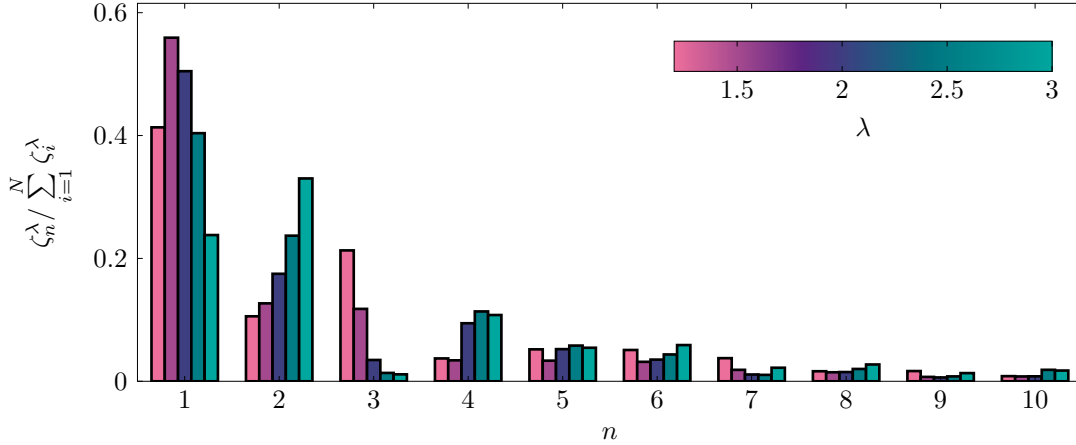


Figure 5.2: Normalised eigenvalues associated with the first ten spatial POD modes for different tip-speed ratios calculated according to equation (5.3).

at $\theta = 329^\circ$. This phase position corresponds to the moment when the blade’s angle of attack returns below its critical stall angle and flow reattachment is initiated.

Dynamic stall plays a central role in the temporal evolution of the power coefficient for vertical-axis wind turbines operating at low tip-speed ratios. For all cases with $\lambda \leq 2.4$ in our configuration, we observe a succession of six characteristic stages, including attached flow, shear layer growth, upwind vortex formation, upwind stall, downwind stall, and flow reattachment. The wind turbine’s performance varies significantly from one stage to the next. Here, we focus on the characterisation of the temporal development of the flow structures during the full dynamic stall life cycle, their influence on the unsteady load response and turbine power production, and changes in the life cycle as a function of the tip-speed ratio.

We use the proper-orthogonal decomposition (POD) of the vorticity field to identify the energetically dominant spatial modes that characterise the flow around our vertical-axis wind turbine blade. The POD time coefficients associated with the dominant spatial modes are examined to identify the characteristic dynamic stall timescales. A single set of spatial eigenmodes is extracted from the ensemble of phase-averaged vorticity fields measured at different tip-speed ratios following the procedure described in section 5.2.

The eigenvalues ζ_n^λ associated with the first ten spatial POD modes for different tip-speed ratios are presented in figure 5.2. The tip-speed ratio specific eigenvalues are calculated according to equation (5.3) and represent the energy contribution of the individual spatial modes in the vorticity field reconstruction for the specific tip-speed ratio. The eigenvalues are normalised by the sum of the tip-speed-ratio-specific eigenvalues. Overall, the energy contribution of the modes decreases rapidly with increasing mode number and the first three modes represent more than 70 % of energy for all tip-speed ratios. Analysing flow structures with POD requires striking a balance between conciseness and completeness. Selecting too few modes means one might ignore a too large energetic portion of the flow, while selecting too many sacrifices the benefits of a low-order analysis. Here, we focus on the first three spatial modes to analyse the temporal development of dominant flow features.

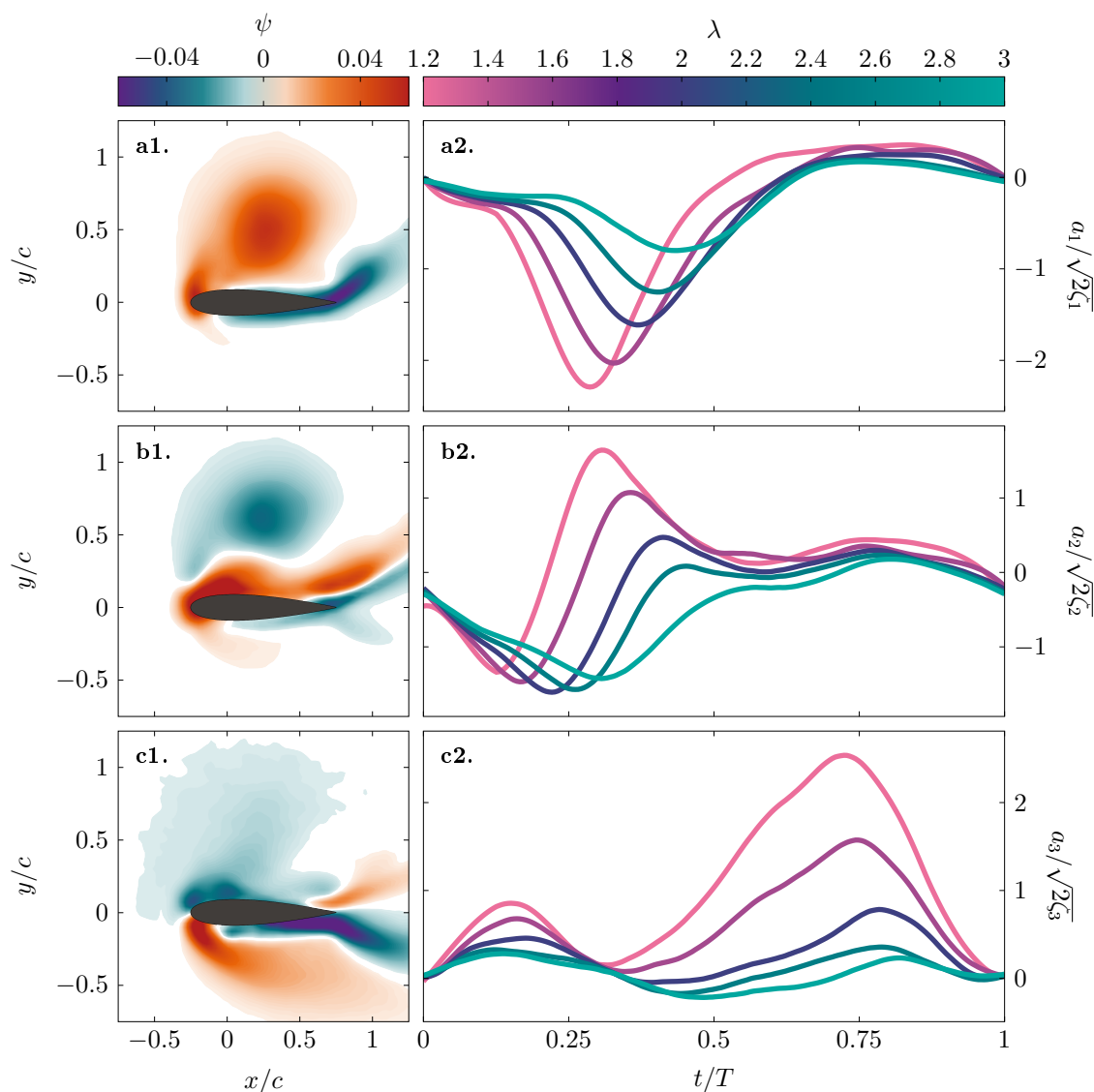


Figure 5.3: First three spatial POD modes (a1-c1) and the evolution of the corresponding time coefficients for tip-speed ratios $\lambda = 1.2, 1.5, 2.0, 2.5$ and 3.0 (a2-c2).

The first three spatial POD modes are presented in figure 5.3. The corresponding time coefficients are shown for tip-speed ratios $\lambda = 1.2, 1.5, 2.0, 2.5$ and 3.0 . The time coefficients a_n are normalised by the eigenvalues obtained from the stacked flow field POD (section 5.2). The first spatial mode is characterised by the presence of a large dynamic stall vortex with a vortex centre located at mid-chord and half-chord length above the blade's surface. Note that the modes are presented in the blade's frame of reference. Everything that is above the blade corresponds to what happens on the intrados of the blade's rotational trajectory. The temporal evolution of the corresponding time coefficient a_1 shows a distinctive peak when the upwind dynamic stall vortex is prominent. The amplitude of the peak increases with decreasing tip-speed ratio. The increase in amplitude highlights a more dominant large-scale vortex for decreasing tip-speed ratio. At lower tip-speed ratios, the maximum effective angle of

Chapter 5. Timescales of dynamic stall development

attack increases (figure 1.2) and the strength of the dynamic stall vortex increases [62]. The first POD mode and the corresponding time coefficient can be used to characterise the timescales related to the formation of the upwind dynamic stall vortex.

The interpretation of the second spatial POD mode is more intricate than the first one, as it seems to combine two consecutive events that occur in the flow. The time coefficient a_2 is negative at the start of the upwind and initially decreases for all cases ($0 \leq t/T < 0.25$). During this time period, flow reversal is first observed on the suction side of the turbine blade or the intrados of the blade's rotational trajectory. Once the blade exceeds its critical stall angle, the time coefficient a_2 starts to increase, becomes positive values, and peaks at the occurrence of vortex lift-off. The increase in a_2 can be interpreted as the transition from a strong accumulation of negative vorticity near the surface during flow reversal, to the growth of a large vortex that entrains positive vorticity near the surface that leads to separation of the main upwind stall vortex. The second POD mode and the corresponding time coefficient can be used to characterise the transition from the accumulation of vorticity and growth of the shear layer to the roll-up of the shear layer into a large-scale upwind dynamic stall vortex.

The third spatial POD mode does not display the presence of a coherent flow structure but rather a state of massively separated flow. The corresponding time coefficient a_3 significantly increases immediately after the separation of the upwind stall vortex, which corresponds to the moment when the amplitude of the first time coefficient a_1 decreases. The third spatial mode represents the fully separated flow following vortex detachment. The severity of the post-stall conditions increases with decreasing tip-speed ratio. Low tip-speed ratio cases are characterised by the formation of a stronger dynamic stall vortex than intermediate and high tip-speed ratio cases and they experience more pronounced deep stall events. The absence of a coherent flow structure in the third spatial mode explains the asymmetry in power production between the upwind and downwind halves of the rotation presented exemplarily in figure 5.1. During upwind, a torque-producing coherent leading-edge vortex is formed. During downwind, the flow is massively separated and the loads are characterised by drag excursions.

The first three POD time coefficients contain the essential information to create a timeline of the temporal flow development on the turbine blade. To further analyse the flow development for different tip-speed ratios, we build a phase map using the time coefficients of the first three POD modes.

The trajectories in the feature space spanned by the POD time coefficients corresponding to the three dominant modes are shown in figure 5.4(a) for tip-speed ratio cases $\lambda = 1.2, 1.5, 2.0, 2.5$ and 3.0 . The trajectory corresponding to the tip-speed ratio $\lambda = 1.5$ is colour-coded and used as an example to demonstrate our approach to identifying the timing of the various stages in the flow development. The feature space representation highlights the interplay between the time coefficients. We analyse the points of inflexion of the trajectory. A change in the relative importance of the time coefficient creates an inflexion point on the trajectory in the feature space and relates to key events in the flow development. The inflexion points were systematically compared to the phase-averaged flow fields to determine their physical

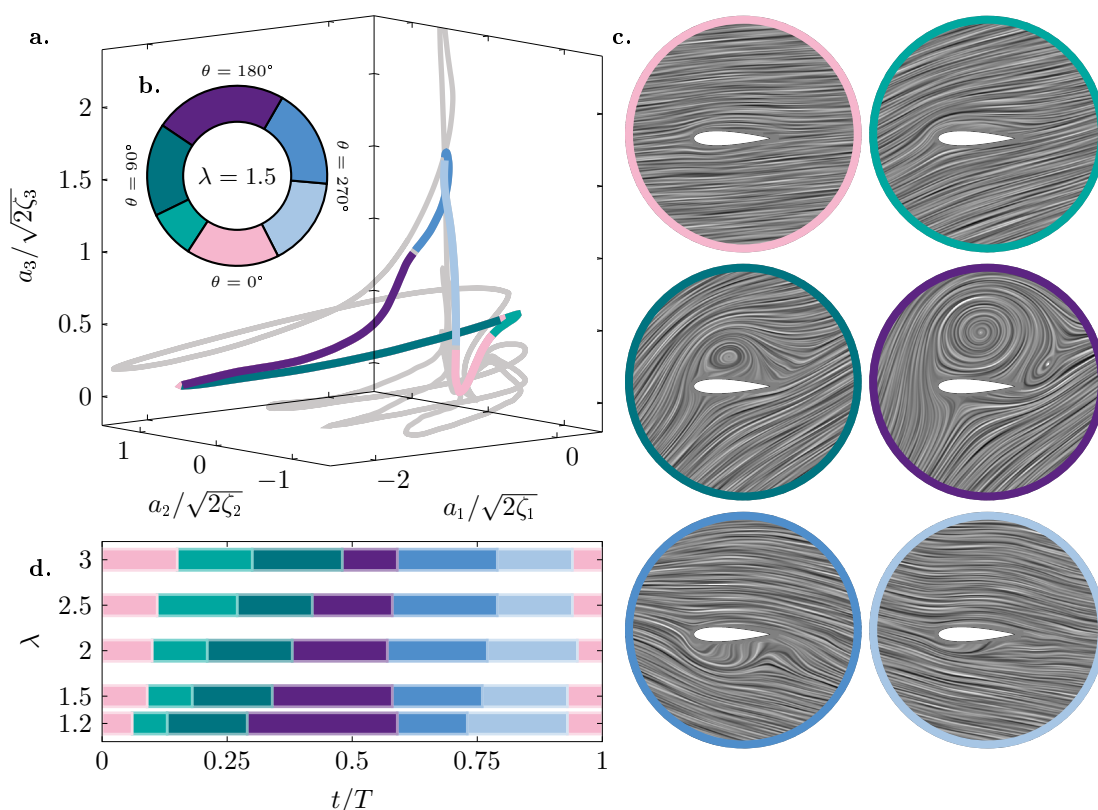


Figure 5.4: (a) Time coefficient parametric curve obtained from the stacked vorticity field POD (section 5.2). The inset (b) shows the phase map of the characteristic dynamic stall stages experienced by the wind turbine blade operating at tip-speed ratio $\lambda = 1.5$. The stages are: attached flow (pink), shear layer growth (teal), vortex formation (dark teal), upwind stall (purple), downwind stall (blue), and flow reattachment (light blue). (c) Selected snapshots of the flow topology representing the characteristic stall stages obtained by the line integral convolution method. (d) Duration and timing of the dynamic stall stages for tip-speed ratio cases $\lambda = 1.2, 1.5, 2.0, 2.5$ and 3.0 .

significance. The results presented here are manually extracted and subject to the authors' discretion. We identify the timing and duration of six landmark stages: attached flow (pink), upwind shear layer growth stage (teal), upwind vortex formation stage (dark teal), upwind stalled stage (purple), downwind stalled stage (blue), and flow reattachment (light blue). A phase map for the six stages is shown for $\lambda = 1.5$ in figure 5.4(b). Visualisations of the flow topology characteristic of the individual stages are obtained by applying the line integral convolution method (LIC) to phase averaged flow field snapshots (figure 5.4(c)). The timing and duration of the dynamic stall stages for tip-speed ratios $\lambda = 1.2, 1.5, 2.0, 2.5$ and 3.0 are summarised in figure 5.4(d).

The same six stages occur for all tip-speed ratios, but the timing and duration of these stages vary. The flow is attached when the blade enters the upwind part of the rotation for all cases. First signs of stall development occur when the blade exceeds its critical stall angle, which happens later in the cycle for higher tip-speed ratios (figure 1.2b). Within less than a quarter of a rotation, a coherent upwind stall vortex has formed, which continues to grow in chord-wise and chord-normal direction until the vortex lifts off and opposite-signed vorticity is entrained between the vortex and the blade's surface. The entrainment of secondary vorticity ultimately leads to the detachment of the stall vortex and the onset of upwind dynamic stall. This

process is similar to the vortex-induced separation observed on two-dimensional pitching and plunging airfoils [28, 78, 90].

The onset of the upwind dynamic stall is identified in the POD feature space in figure 5.4(a) as the local maximum of a_2 and the minimum of a_1 . The time interval between the moment when the critical stall angle is exceeded and the onset of stall, is defined as the upwind stall development, which is divided into two parts in analogy with the flow development observed on pitching airfoils [27, 77]. The first part is characterised by the accumulation of bound vorticity and the thickening of the surface shear layer. We call this stage the shear layer growth stage. The shear layer growth stage (■) takes up a larger portion of the cycle when the tip-speed ratio increases (figure 5.4d). A kink in the feature space at the minimum of a_2 and a local extremum of a_1 marks the start of the roll-up of the shear layer into a coherent dynamic stall vortex. This second part of the upwind stall development is characterised by the growth of the upwind dynamic stall vortex and is called the upwind vortex formation stage. The vortex formation stage (■) occupies approximately the same portion of the cycle for all tip-speed ratios but ends earlier in the cycle for lower tip-speed ratios (figure 5.4d). Stall onset marks the end of the vortex formation stage and the start of the upwind stalled stage.

The next transition is marked by the switch of the leading edge stagnation point from the intrados of the blade path to the extrados, which corresponds respectively to the bottom and the top side of the blade in the snapshots presented in figure 1.2c. This transition is identified in the POD feature space as an inflexion point in the gradient of a_3 and occurs at approximately the same point in the cycle (figure 5.4d). As the blade enters the downwind half of the rotation, the fully separated flow has no time to reattach to the blade even though the angle of attack is theoretically at 0° when $\theta = 180^\circ$. Furthermore, the blade's angle of attack varies more rapidly in the first part of the downwind than during the upwind. There is insufficient time for a clear shear layer growth and vortex formation stage during the downwind, so we only consider an overall downwind stalled stage [62]. The end of the downwind stalled stage is marked by the maximum value of a_3 and it is followed by the flow reattachment stage.

The flow reattaches to the blade for all cases in the last quarter of the turbine's rotation. The absence of flow reattachment between the upwind and downwind parts of the rotation is related to the chord-to-diameter ratio. This parameter governs the frequency at which the turbine blade experiences the variation in effective flow conditions and the perceived curvature of the flow. In this study, the chord-to-diameter ratio is at the higher end of the spectrum ($c/D = 0.2$), and the switch in the effective flow conditions occurs too fast for the flow to reattach between the upwind and downwind.

The characteristic upwind dynamic stall delay is the combined duration of the shear layer growth and the vortex formations stage. Based on previous work, we expect that the duration of the stall delay expressed in convective time scales becomes independent of the kinematics for larger reduced frequencies [5, 60]. Generally, the non-dimensional convective time is obtained by dividing the physical time by c/U , with U a constant characteristic velocity. Here, the effective flow velocity experienced by the blade changes constantly and instead of using the blade velocity or the free-stream velocity to obtain a non-dimensional convective time, we

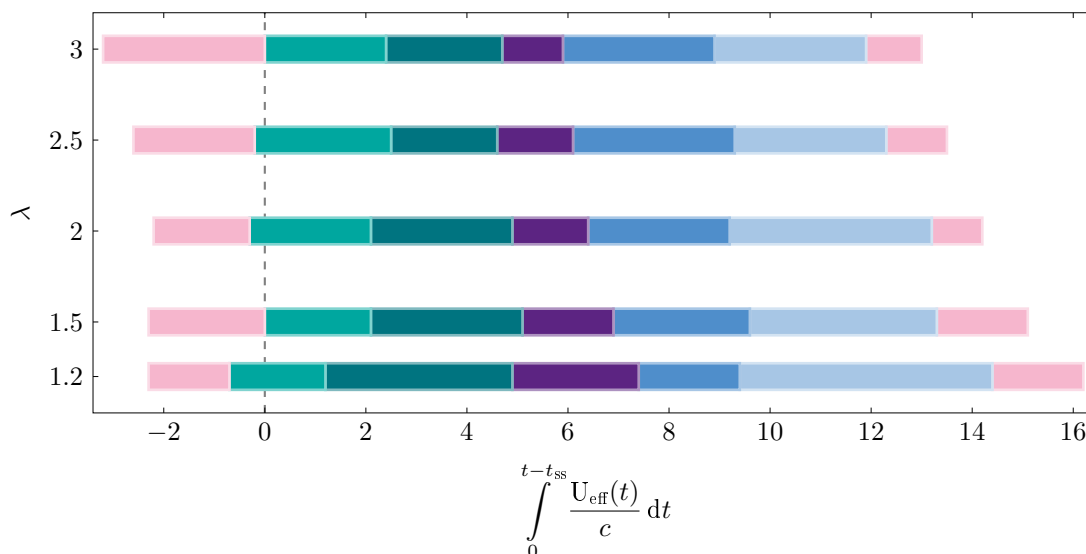


Figure 5.5: Duration and timing of the dynamic stall stages for tip-speed ratio cases $\lambda = 1.2, 1.5, 2.0, 2.5$ and 3.0 in terms of the convective time.

opt here to take the constantly varying effective flow velocity into account and calculate the convective time perceived by the turbine blade using:

$$\int_0^{t-t_{ss}} \frac{U_{\text{eff}}(t)}{c} dt, \quad (5.4)$$

where U_{eff} is the effective flow velocity obtained from the vectorial combination of the blade velocity and the incoming flow velocity (figure 1.2).

The temporal occurrence of dynamic stall stages scaled with the convective time is presented in figure 5.5. Note that we subtract the time at which the static stall angle is exceeded t_{ss} to realign subsequent stall events, in accordance with results presented in [14]. When we express the upwind stall delay (■ + ■) in terms of convective times, the stall delay does not depend on the tip-speed ratio and converges to approximately 4.5 convective times, which matches standard vortex formation times found in literature [20, 29, 43, 54]. The combination of the upwind and downwind stalled stages also reaches similar values for all tip-speed ratios, although the distribution between the two stages varies. The flow reattachment timescale decreases slightly for increasing tip-speed ratios. This trend may be due to the discrepancy between the effective flow velocity calculated using equation (1.3) and the actual effective flow velocity acting on the turbine blade in the downwind half of the turbine rotation. Equation (1.3) neglects any influence of the induced velocity from shed vorticity, which is abundant in the downwind half of the turbine's rotation. Overall, the convective time offers a promising scaling option for dynamic stall timescales on vertical axis turbines. Further work can aim at modelling the influence of vorticity induced velocity to improve the scaling and implement universal timescales into dynamic stall modelling and control strategies for vertical-axis wind turbines.

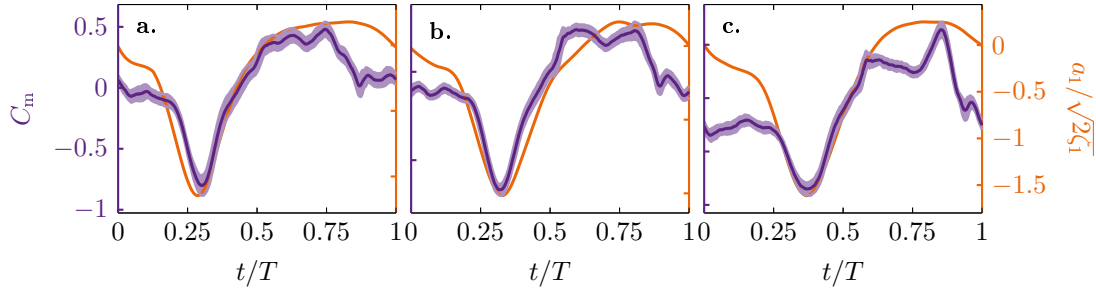


Figure 5.6: Comparison of the temporal evolution of the first POD mode time coefficient a_1 and the phase-averaged pitching moment coefficient for tip-speed ratio cases $\lambda = 1.2, 1.5, 2.0$.

We cannot rely on flow measurements if we want to achieve real-time active flow control on a wind turbine blade. The processing time of the flow measurement around the blade, capturing vortex formation or incoming gusts, for instance, is prohibitively high to actuate a response in time. Finding patterns in the readily available aerodynamic loads that indicate the occurrence of stall stages is desirable. This feasibility of replacing the time series of the POD coefficients with load measurement time series was inspired by the similarity between some features in the POD time coefficients and the temporal development of the aerodynamic loads. In figure 5.6, we compare the temporal evolution of the time coefficient a_1 corresponding to the first POD mode and the phase-averaged pitching moment coefficient for tip-speed ratios $\lambda = 1.2, 1.5, 2.0$. The general shape of the two curves is in close agreement. The timing of the distinctive peak displayed by the time coefficient a_1 perfectly matches the timing of the negative pitching moment peak. The pitching moment is highly sensitive to changes in the formation of the large-scale upwind dynamic stall vortex, which is characterised by the mode coefficient a_1 . This further confirms our interpretation of the first POD mode and motivates us to extract the timing and duration of the dynamic stall stages based solely on the aerodynamic loads.

We analyse the dynamic stall timescales based on the development of the unsteady loads experienced by the wind turbine blade using a similar approach as for the POD time coefficients. Our new feature space is built using the azimuthal force, radial force and pitching moment coefficients and analyse the measured trajectories in figure 5.7(a) for 19 tip-speed ratio cases with $\lambda \in [1.2 - 3.0]$. The trajectory corresponding to the tip-speed ratio $\lambda = 1.5$ is colour-coded and used as an example to demonstrate the automated identification of the dynamic stall stages from the unsteady loads. Automated identification increases the robustness and the potential of using unsteady loads as the input for active flow control laws. The points of inflexion formed by the unsteady load trajectories are not as clearly defined as those in the POD time coefficient trajectory shown in figure 5.3(a), but we are able to identify five extrema that are systematically featured in the temporal development of the aerodynamic loads and that can be directly related to the changes in the dynamic stall life cycle. These extrema were identified by closely analysing the interplay between flow structures developing around the turbine blade and abrupt changes in the load response.

The first extremum we identified is the tangential force minimum occurring shortly after the blade enters the upwind half of its rotation ($0 \leq t/T < 0.5$) (figure 5.7b). This time instant is followed by a strong increase in torque production, which corresponds to the shear-layer

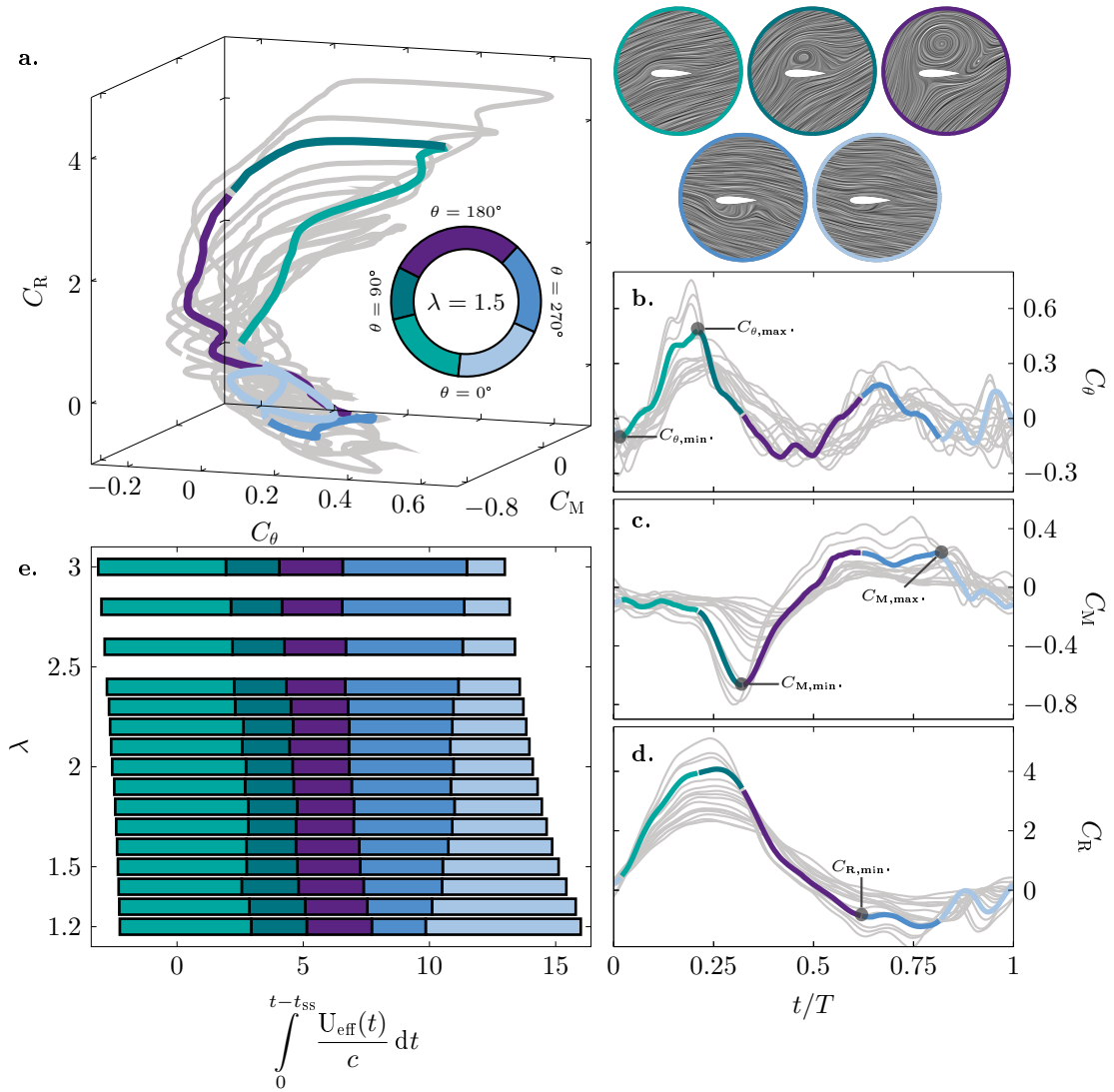


Figure 5.7: (a) Unsteady force parametric curve for tip-speed ratios $\lambda \in [1.2-3.0]$. The inset shows the phase map of the characteristic dynamic stall stages experienced by the wind turbine blade operating at tip-speed ratio $\lambda = 1.5$. The stages are: attached flow and shear layer growth (teal), vortex formation (dark teal), upwind stall (purple), downwind stall (blue), and flow reattachment (light blue). (b) Duration and timing of the dynamic stall stages retrieved from the unsteady loads for tip-speed ratio $\lambda \in [1.2-3.0]$. Temporal evolution of phase-averaged unsteady (c) tangential load coefficient C_θ , (d) pitching moment coefficient C_M , (e) radial force coefficient C_R for tip-speed ratios $\lambda \in [1.2-3.0]$. Selected snapshots of the flow topology representing the characteristic stall stages are repeated as reminders.

growth stage (figure 5.1, $\theta = 45^\circ$). The end of the shear-layer growth stage coincides with the tangential force maximum occurring around $t/T = 0.25$. The vortex formation stage is characterised by the convection of the upwind dynamic stall vortex from the leading edge towards the mid-chord position, causing a significant excursion of the pitching moment coefficient from just below 0 to its minimum value $C_{M,\min}$ (figure 5.7c). The pitching moment minimum coincides with vortex separation and the beginning of the upwind stalled stage. Vortex separation is followed by a significant loss in radial force that decreases until around $t/T = 0.6$, reaching a plateau that corresponds to the downwind stalled stage. Lastly, the pitching moment coefficient reached a local maximum before returning to its initial value during the flow reattachment stage. These extrema are used to identify the landmark dynamic stall stages for all tip-speed ratio cases $\lambda \in [1.2 - 3.0]$. The radial force coefficient (figure 5.7d) helps to separate the local extrema of interest in the other loads and automate their identification.

A phase map showing the temporal occurrence of dynamic stall stages identified using unsteady loads is shown as an inset in figure 5.7(a) for $\lambda = 1.5$. The stages we identify from loads are the same as those identified using the time coefficient of the vorticity field POD with one exception: the attached flow stage. There is no clear indication of an attached stage in the unsteady load response. The blade experiences an immediate load response to the increase of the effective angle of attack at the beginning of the blade's rotation, but the appearance of flow reversal and shear-layer growth is delayed to higher angles of attack. The first stage (■) shown in figure 5.7(e) thus combines the attached flow stage and the shear layer growth stage. The timing and duration of the following stages match those computed with the POD time coefficients. These findings suggest that the aerodynamic loads contain sufficient information to identify whether a wind turbine blade is undergoing dynamic stall and which stage the flow development is currently in.

A direct comparison of both stage identification methods is desirable to assess the potential of unsteady loads to capture the timescales of flow development for analytical or control purposes. To allow for a direct comparison between the stages computed from the aerodynamic loads and those obtained using the POD time coefficients, we calculated the work done by the total aerodynamic force in each stage for both methods. The work done by the total aerodynamic force over a given stage is calculated with:

$$W_{\text{stage}} = \overline{F_{\text{tot}}} \Theta_{\text{stage}} R \quad (5.5)$$

where $\overline{F_{\text{tot}}}$ is the mean total aerodynamic force experienced by the turbine blade over that stage and Θ_{stage} is the angular distance covered by the blade throughout the stage. This metric allows a pertinent comparison between the two stage identification methods because it accounts for both the duration of the stage and the magnitude of the loads experienced by the turbine blade during that stage. A small error in the timescale of a given stage is enhanced if the stage is related to significant unsteady loads. The total force was selected because it accounts for both the radial and tangential force components. The stage-wise contributions to the work completed by the aerodynamic force are compared in figure 5.8 for stages identified using either the aerodynamic loads or the POD time coefficients for tip-speed ratios $\lambda = [1.2, 1.5, 2.0, 2.5 \text{ and } 3.0]$. To facilitate the comparison, the work completed in each

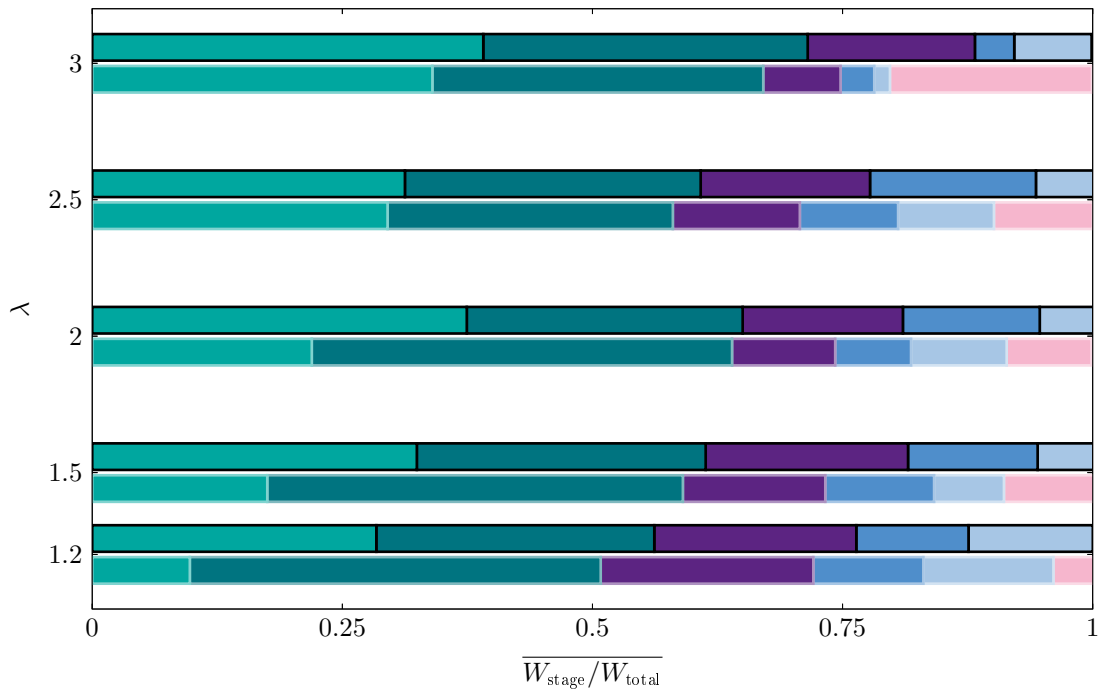


Figure 5.8: Stage-wise contribution to the total work completed by the total aerodynamic force throughout the blade's rotation. The stage contributions are compared for stages identified either by using aerodynamic loads (dark contours) or by using POD time coefficients (light contours) for tip-speed ratios $\lambda = [1.2, 1.5, 2.0, 2.5 \text{ and } 3.0]$.

stage W_{stage} is normalised by the total work completed by the aerodynamic force throughout the blade's rotation $W_{\text{total}} = \overline{F_{\text{tot}}} 2\pi R$.

Overall, most of the aerodynamic work is completed during the shear layer growth (■) and the vortex formation stage (■). These stages are associated with the accumulation of vorticity close to the blade's surface, which creates significant suction over about one quarter of the turbine's rotation. This trend is verified for both stage identification methods at all tip-speed ratios. The combined contribution of the shear layer growth and the vortex formation stage is nearly independent of tip-speed ratio and reaches 0.6 for all cases. Both stage identification methods show excellent agreement. The aerodynamic loads do not allow for a clear identification of the attached flow stage. Instead, the attached flow stage is distributed across the flow reattachment and mainly the shear layer growth stages. The work contribution of the attached flow stage is limited across tip-speed ratios. The accurate capture of key timescales, such as the vortex formation time, is a satisfactory and promising result for the use of aerodynamic loads as a tool to identify flow development timescales and implement closed-loop control strategies.

5.4 Conclusion

We collected time-resolved velocity field and unsteady load measurements on a vertical-axis wind turbine operating at low tip-speed ratios $\lambda \in [1.2 - 3.0]$ to characterise the chain of events that leads to dynamic stall and to quantify the influence of the turbine operation conditions

Chapter 5. Timescales of dynamic stall development

on the duration of the individual stages of the flow development. The dominant flow features and their timescales were first analysed using a proper orthogonal decomposition of the stacked vorticity fields from different tip speed ratio conditions. This procedure is known as a parametric modal decomposition and yields a single set of representative spatial modes and tip-speed ratio specific temporal coefficients and eigenvalues that can be directly compared to characterise the influence of the tip-speed ratio on the temporal development of the dominant spatial flow features.

Based on the POD time coefficients of the three most energetic modes, we were able to identify the timing and duration of six landmark dynamic stall stages: the attached flow, shear layer growth, vortex formation, upwind stall, downwind stall, and flow reattachment stage. The duration of the attached flow increases with increasing tip-speed ratio as the blade exceeds its critical stall angle later for higher tip-speed ratios. The combined duration of the shear layer growth and vortex formation stages represent the characteristic dynamic stall delay. This dynamic stall delay is independent of tip-speed ratio for our experimental conditions and reaches a constant non-dimensional value of 4.5 convective times, which corresponds to the typical dynamic stall delays found on non-rotating pitching and plunging airfoils at comparable reduced frequencies. The upwind and downwind stall stages shorten with increasing tip-speed ratio as the blade spends less time at angles of attack beyond the critical stall angle. Flow reattachment starts once the blade returns below its critical angle and full reattachment is reached within 3 to 4 convective times for all cases studied. The dynamic stall stages were also identified based solely on the measured aerodynamic loads. The timing of the dynamic stall stages based on the loads agrees well with the timing based on the time coefficients of the first three modes of the POD of the vorticity field.

Our findings demonstrate that aerodynamic loads are suitable for analysing the timescales of flow development on a vertical axis wind turbine blade and can be used for flow control applications. However, a control strategy should not necessarily aim at avoiding the onset of dynamic stall as the work completed by the aerodynamic forces during the upwind dynamic stall delay represents approximately 60 % of the total work completed throughout the turbine's rotation. Future work should focus on careful management of the dynamic stall vortex formation and shedding to exploit the work done by the vortex but avoid potential negative ramifications related to its shedding.

FLOW CONTROL ON VERTICAL-AXIS WIND TURBINES

PART III

6

THE ROLE OF BLADE PITCH ANGLE IN DYNAMIC STALL DEVELOPMENT

Vertical-axis wind turbines that operate at low-tip speed ratios undergo deep dynamic stall, which leads to a significant loss in efficiency and undesired load fluctuations. We wish to investigate the potential of blade pitching as a flow control. The first step in this endeavour was to assess the influence of a static change in pitch angle on the turbine's power performance and the flow development around the turbine blade. Our results show a significant response of the turbine performance to a static pitch-angle offset, which encourages the investigation of dynamic blade pitching.

CHAPTER HIGHLIGHTS

- ⊙ We compare the performance of vertical-axis wind turbines operating at a low tip-speed ratio of $\lambda = 1.5$ with blade pitch-angle offsets ranging from -24° to 5° .
- ⊙ Moderately low pitch angle offsets ($\alpha_{\text{offset}} \in [-9^\circ, -4^\circ]$) improve the power coefficient by 25 % and reduce the load fluctuations related to flow separation by 20 % compared to no pitch-angle offset at $\lambda = 1.5$.
- ⊙ Static pitch-angle offsets affect the timescales of vortical flow structures forming on the blade and the direction of the aerodynamic force acting on the blade to enhance wind turbine performance.

6.1 Introduction

Adopting a control strategy to mitigate the occurrence of dynamic stall on vertical-axis wind turbines is desirable. Control strategies are categorised as active or passive based on whether they require actuation during the turbine's operation. Passive control strategies are advantageous because they do not require significant installation or maintenance costs and do not increase the turbine's complexity. These strategies include tuning geometrical parameters, such as airfoil shape, turbine geometry or blade pitch angle, or using passive actuators, such as surface treatments, vortex generators or torsional springs on the blade mounts.

Blade pitch angle is a promising passive control strategy that has previously attracted academic attention. This strategy aims at shifting the theoretical angle of attack variation (equation (1.2)) by a fixed increment, here called the pitch-angle offset α_{offset} , as shown in figure 6.1. The instantaneous forces experienced by a wind turbine blade with pitch-angle offsets in the range of -7° to 3° were investigated at high tip-speed ratios using unsteady Reynolds-averaged Navier-Stokes simulations by Rezaeiha, Kalkman, and Blocken [87]. The blade's aerodynamic performance was shown to be highly sensitive to a pitch-angle offset. A 6.6 % power coefficient improvement was achieved for a -2° pitch offset at tip-speed ratio $\lambda = 4$. Wind tunnel experiments performed by Armstrong, Fiedler, and Tullis [4] investigated pitch-angle offsets α_{offset} between -9° and 3° for a high-solidity vertical-axis wind turbine. The power coefficient was highest at $C_p = 0.275$ for $\alpha_{\text{offset}} = -3.5^\circ$ at $\lambda = 2$, with a 20 % improvement compared to $\alpha_{\text{offset}} = -1.5^\circ$. Studies of the blade-level physics of a vertical-axis wind turbine blade with a pitch-angle offset operating at low tip-speed ratios are lacking. Numerical investigations struggle to capture the blade-level fully separated flow physics unless they become prohibitively expensive to sweep multiple pitch-angle offsets [38, 39, 87]. Experimental investigations generally measure turbine-level metrics, such as the power coefficient, rather than focus on instantaneous blade-level physics.

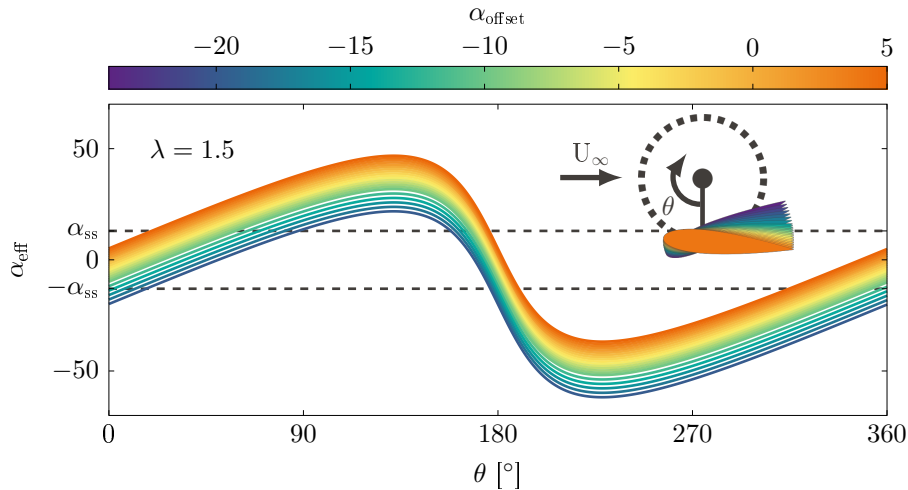


Figure 6.1: Temporal variation of the effective angle of attack α_{eff} for a wind turbine blade operating at tip-speed ratio $\lambda = 1.5$ with a blade pitch-angle offset α_{offset} . The convention used as blade pitching direction is depicted at the top right of the figure, along with the blade's $\theta = 0^\circ$ starting position and direction.

This chapter investigates a broad range of pitch-angle offsets between -24° and 5° for a single-bladed vertical-axis wind turbine undergoing dynamic stall at tip-speed ratio $\lambda = 1.5$. We perform time-resolved force measurements to compare the temporal development of the instantaneous power coefficient and pitching moment coefficient across pitch-angle offsets. The time-averaged power coefficient and pitching moment standard deviation are calculated for each blade pitch angle. The latter metric measures the intensity of undesired load fluctuations related to flow separation (chapter 4). Time-resolved particle image velocimetry allows us to unravel the mechanism by which pitch-angle offsets can improve the performance of wind turbine blades.

6.2 Experimental methods

The data presented in this chapter was obtained using the same experimental apparatus and methodologies as those described in chapter 4. Here, all dimensionless parameters that describe the turbine's operating conditions were kept constant (equation (1.1)). The chord-to-diameter ratio was 0.2, the chord-based Reynolds number was 50 000, and the tip-speed ratio was 1.5.

For each experiment, we systematically actuated the blade pitching motor to adjust the blade's angle of attack offset during the first turbine rotation. The pitch offset was kept constant during the experiment, so the pitching blade motor only provided the holding torque to maintain the blade's pitch angle. We investigated blade pitch-angle offsets α_{offset} in the range of -24° to 5° . We allowed 5 full turbine rotations for the turbine wake to fully develop before accounting for the forces acting on the turbine blade. We recorded forces for 100 rotations and brought the blade to rest.

We evaluate the performance of each blade pitch offset by computing two metrics: the power coefficient (equation (3.8)) and the pitching moment standard deviation. The power coefficient is the conventional measure for wind turbine efficiency, indicating the proportion of the kinetic energy carried by the flow converted into mechanical torque. The pitching moment standard deviation was demonstrated to correlate with the unsteady load fluctuations related to the occurrence of flow separation from the blade's surface chapter 4. These metrics were compared across the full range of pitch-angle offsets and determined an optimal pitch-angle offset. We acquired time-resolved flow measurements to compare the development of flow structures for the wind turbine blade with optimal pitch-angle offset and no angle offset.

6.3 Results

The temporal evolution of the instantaneous power and pitching moment coefficients are compared for the complete range of pitch-angle offsets in figure 6.2(a) and (c) respectively. The time-averaged power coefficients and pitching moment standard deviations are compared in figure 6.2(b) and (d) respectively. Desirable performance maximises the power coefficient while minimising the pitching coefficient standard deviation. Both metrics feature an optimal

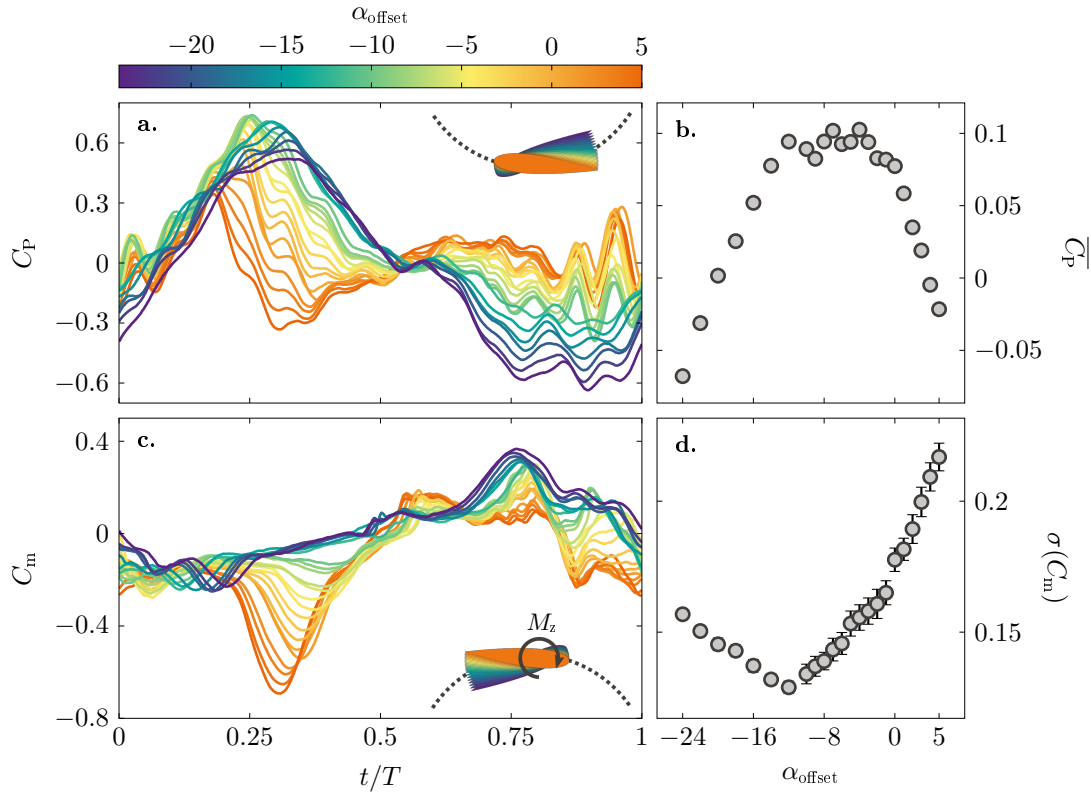


Figure 6.2: Temporal evolution of (a) the instantaneous power and (c) pitching moment coefficients for the complete range of pitch-angle offsets $\alpha_{\text{offset}} \in [-24^\circ - 5^\circ]$. The time-averaged power coefficients $\overline{C_p}$ and pitching moment standard deviations $\sigma(C_m)$ are compared in (b) and (d) respectively. The error bars represent the standard deviation of these metrics across the 100 turbine rotations. The error bars are invisible for some points because they are tiny and hidden by the marker.

point that is reached for different pitch-angle offsets. The mean power coefficient reaches a maximum of $\overline{C_p} = 0.1$ at $\alpha_{\text{offset}} = -4^\circ$, though one can argue that the power coefficient features a plateau around 0.1 between $\alpha_{\text{offset}} = -4^\circ$ and -9° . The pitching moment coefficient standard deviation features a distinctive minimum at $\alpha_{\text{offset}} = -12^\circ$. Based on these observations, we divide our analysis into three groups: pitch-angle offsets greater than 0° , smaller than -9° and between 0° and -9° .

We first compare the performance of pitch-angle offsets between 0° and -9° . A simple -4° pitch-angle offset improves the mean power coefficient by 25 % compared to no pitch-angle offset. Reducing the pitch-angle offset up to -9° increases and widens the peak power coefficient achieved in the upwind half of the turbine rotation around $t/T = 0.3$. This improvement in upwind performance only slightly sacrifices the performance of the downwind half, arguably because the blade undergoes deep stall for all pitch-angle offsets between -9° and 0° . At those pitch offset angles, the dynamic stall vortex yields a characteristic minimum on the pitching moment coefficient evolution between $t/T = 0.3$ and 0.4 . This minimum occurs progressively later for decreasing pitch-angle offset, suggesting vortex formation occurs later for low pitch-angle offsets. This result is expected since the blade exceeds its critical stall angle later in the rotation. In the downwind half, the power coefficient becomes negative and the

pitching moment flips to positive values. Both observations suggest the flow is massively separated for most of the downwind half. Though decreasing pitch-angle offsets results in slightly deteriorated power performance in the downwind half, the performance is much less sensitive to pitch-angle offset in the downwind half compared to the upwind half. Pitch-angle offsets between -4° and -9° all found a strong compromise between high power production in the upwind half and limited power loss in the downwind half.

Further reducing the pitch-angle offset below -9° yields a wider but smaller peak in the instantaneous power coefficient upwind and a significant drag excursion in the downwind half. The smallest pitching moment standard deviation was reached at -12° , achieving a 24 % decrease compared to no pitch-angle offset. The temporal evolution of the pitching moment coefficient does not feature a significant peak in either the upwind or downwind half for blade-pitch offset around -12° . This behaviour suggests the blade does not experience deep stall, limiting the severity of post-stall load fluctuations. Very low pitch-angle offsets ($\alpha_{\text{offset}} < -12^\circ$) feature a significant maximum in pitching moment coefficient in the downwind half around $t/T = 0.8$. This peak arguably results from the formation of a large-scale dynamic stall vortex on the extrados of the blade's circular path. This would not be surprising given that the effective angle of attack can reach values lower than -40° . A vortex forms on the surface of the blade that is pitched towards its suction side in the downwind half. The vortex' suction on the blade surface results in a prohibitively large negative power coefficient excursion. Pitch-angle offsets below -9° avoid stall in the upwind half but experience deep stall in the downwind half instead, resulting in a poor mean power coefficient performance.

Increasing the pitch-angle offset above 0° rapidly decreases the mean power coefficient and increases the pitching moment standard deviation. The temporal evolution of the pitching moment coefficient features a greater peak that occurs earlier in the blade's rotation. This suggests the turbine blade spends a more significant portion of the upwind half surrounded by fully separated flow. Positive pitch-angle offsets are detrimental to wind turbine performance in terms of power production and structural resilience. Flow measurements are desirable to analyse the mechanisms by which pitch-angle offsets influence turbine performance.

Flow measurements were performed on a wind turbine blade operating at tip-speed ratio $\lambda = 1.5$ with a pitch-angle offset $\alpha_{\text{offset}} = -4^\circ$. This pitch-angle offset was selected because it achieved the highest mean power coefficient. Compared to lower pitch-angle offset, $\alpha_{\text{offset}} = -4^\circ$ had a slightly higher pitching moment standard deviation. However, the power coefficient displayed lower asymmetry between the upwind and downwind halves compared to the lower pitch-angle offsets. Having fewer variations in power coefficient is desirable in the design of vertical-axis wind turbine, validating our choice of selecting $\alpha_{\text{offset}} = -4^\circ$. This optimum also agrees with findings in the literature [4, 87].

Polar plot of the temporal evolution of the phase-averaged power coefficient C_p for wind turbine blades operating at tip-speed ratio $\lambda = 1.5$ with no pitch-angle offset and a pitch-angle offset $\alpha_{\text{offset}} = -4^\circ$ are compared in figure 6.3. In a polar plot, a radial increase of the plotted line indicates an increase in power coefficient C_p . The central circle represents the $C_p = 0$ level. The azimuthal progression of the line represents time, plotted according to our usual

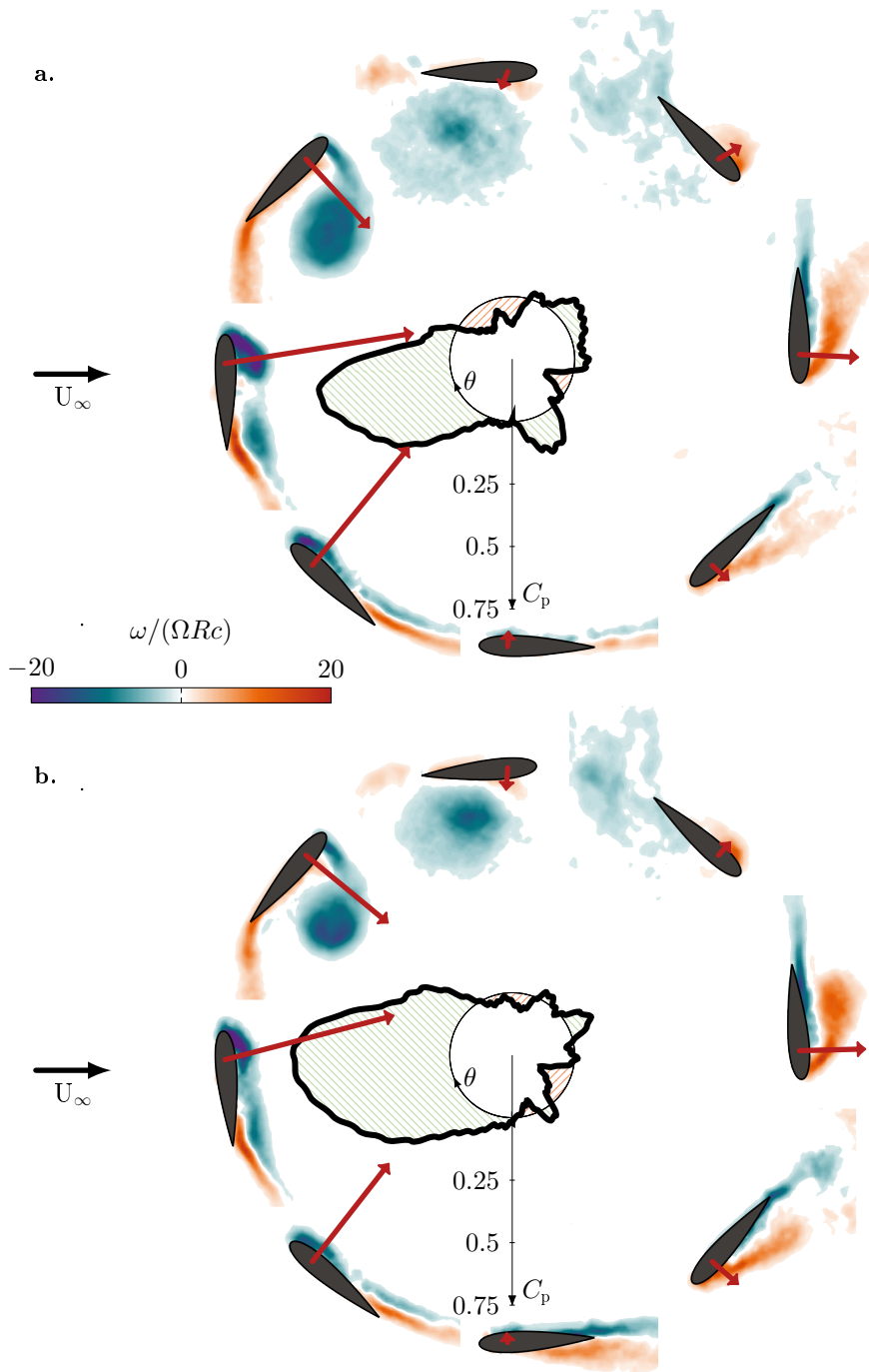
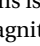
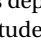


Figure 6.3: Polar plots of the temporal evolution of the phase-averaged power coefficient C_p for wind turbine blades operating at tip-speed ratio $\lambda = 1.5$ with (a) pitch-angle offset $\alpha_{\text{offset}} = 0^\circ$ and (b) a pitch-angle offset $\alpha_{\text{offset}} = -4^\circ$. Phase-averaged normalised vorticity fields are shown at eight equally spaced azimuthal positions ($\theta = [0 : 45 : 360^\circ]$) to illustrate the development of flow structures for both individuals. The total aerodynamic force acting on the blade at the various azimuthal locations is depicted by arrows starting from the blade's quarter-chord. The length of the arrows indicates the relative magnitude of the force. The hatched regions  and  represent regions of torque generation and dissipation respectively.

convention for wind turbine blades (figure 1.2). Phase-averaged normalised vorticity fields are shown throughout the blade's rotation for both pitch-angle offsets. In the upwind half, the vorticity fields at $\theta = 45^\circ$, 90° and 135° show that vortex formation is slightly delayed for the $\alpha_{\text{offset}} = -4^\circ$ blade compared to no pitch-angle offset. The stall vortex is systematically slightly smaller and more coherent for the $\alpha_{\text{offset}} = -4^\circ$ case compared to $\alpha_{\text{offset}} = 0^\circ$. The negative pitch angle offset redirects the total aerodynamic force experienced by the blade in the presence of the large-scale vortex towards the forward tangential direction. The total force has a comparable magnitude for both cases, but the pitch-angle offset of -4° redirects the force towards the torque-generating direction. The force redirection yields a much higher peak in power production at $\theta = 90^\circ$, and the delayed vortex formation extends this peak's duration.

The downwind half of the turbine's rotation features fully separated flows for both cases. Here, the small pitch-angle offset is detrimental to the turbine's performance. Similarly to the upwind half, the pitch-angle offset redirects the aerodynamic force. This time, however, the blade is pitched towards the suction side, so the force is re-oriented backwards in the tangential direction. The blade with no blade pitch-angle offset generates small amounts of torque at $\theta = 270^\circ$, while the blade at $\alpha_{\text{offset}} = -4^\circ$ dissipates torque at the same position. Flow reattachment is slightly delayed for the blade at $\alpha_{\text{offset}} = -4^\circ$, depriving this blade of the small region of power production at the end of the downwind half. Nevertheless, the significant peak in power production achieved in the upwind half by the blade at $\alpha_{\text{offset}} = -4^\circ$ outweighs the limited power production from the downwind half. The key to performance improvement was the redirection of the aerodynamic force when it was at its largest ($\theta = 90^\circ$). This mechanism was reversed in the downwind half ($\theta = 270^\circ$) with little consequence because the total force was near its lowest.

6.4 Conclusion

In this chapter, we investigated the influence of a static pitch-angle offset on turbine performance. We kept the turbine operating conditions constant at a low tip-speed ratio of $\lambda = 1.5$ to study the influence of pitch angle on a blade that undergoes dynamic stall. We systematically varied the blade's pitch angle in the range of -24° to 5° for each experiment. We distinguished three different categories of blade pitch-angle offsets based on their influence compared to no pitch-angle offset. Positive pitch-angle offsets encourage early vortex formation and suffer from the extended occurrence of dynamic stall, which was detrimental both for power production and turbine structural integrity. Large negative pitch-angle offsets ($\alpha_{\text{offset}} < -12^\circ$) mitigate the occurrence of stall in the upwind half of the turbine rotation but undergo deep dynamic stall in the downwind half. These pitch angles suffer less from post-stall consequences than positive pitch angles but sacrifice power production. Moderately low pitch angle offsets ($10 < \alpha_{\text{offset}} < -3^\circ$) yield a strong power performance in the upwind half. Power enhancement is achieved by redirecting the total aerodynamic force towards the forward direction tangential to the blade's path. During the formation of large-scale vortices in the upwind half, force redirection is very beneficial to the turbine's performance. In the downwind half, moderately low pitch-angle offsets redirect the total force backwards in the direction

Chapter 6. The role of blade pitch angle in dynamic stall development

tangential to the blade's path. This effect is detrimental but limited because the flow is fully separated, and the total force is small. Overall moderately low pitch-angle offsets achieve the best compromise, improving the power coefficient by 25 % and reducing the load fluctuations related to flow separation by 20 % at $\lambda = 1.5$. Nevertheless, static pitch angle offsets have several limitations in improving turbine performance. Pitch-angle offsets that are beneficial in the upwind half become detrimental in the downwind half due to the reversal between the suction and pressure sides of the blade. The optimal pitch angle position will change across the operating condition, given that the blade perceives different flow conditions. Having an active control strategy is desirable.

OPTIMAL BLADE PITCHING KINEMATICS

Vertical-axis wind turbines are great candidates to enable wind power extraction in urban and off-shore applications. Currently, concerns around turbine efficiency and structural reliability limit their industrial deployment. Flow control can mitigate these concerns. Blade pitching is recognized as a high-potential flow control strategy, but we lack an understanding of the flow physics that could yield performance enhancement. We investigate blade pitching using a scaled-down turbine model coupled to a genetic algorithm optimiser that performed unsupervised experiments to seek optimal pitching kinematics at on and off-design operating conditions.

The content of this chapter was prepared for submission to a broad audience journal.

CHAPTER HIGHLIGHTS

- ⊙ Optimal blade kinematics yielded a three-fold power coefficient increase at both off and on-design operating conditions compared to the non-actuated turbine and a 70 % reduction in structure-threatening load fluctuations at off-design conditions.
- ⊙ We perform particle image velocimetry to uncover how blade pitching manipulates flow structures to achieve performance enhancement.
- ⊙ Optimal blade pitching can be parametrised using a simple sum of two sin waves. Guidelines on the design of a baseline pitch profile for a wind turbine blade operating at an arbitrary tip-speed ratio are provided.

7.1 Introduction

The aerodynamic complexity of vertical-axis wind turbines has hampered their industrial development. The blade encounters varying flow conditions throughout a single turbine rotation, even in a steady wind. When the turbine operates at a low rotational velocity compared to the incoming flow velocity, the blade perceives significant amplitude changes in the angle of attack and relative wind velocity. Varying flow conditions can give rise to flow separation and the formation of large-scale vortices on the surface of the turbine blades [14, 96]. For wind turbine applications, large-scale vortices are considered undesirable because they lead to a significant loss in efficiency and load transients that jeopardise the turbine's structural integrity [14, 58, 62]. Birds, insects, and fish have developed strategies to interact with vortical structures and achieve outstanding aerodynamic performance compared to homologous engineered devices [34, 103]. Implementing flow control strategies to harness the lift-enhancing properties of vortices on wind turbine blades is desirable. On a wind farm level, vortical flow structures were harnessed to improve turbine power performance by placing counter-rotating units adjacently [21]. Here, we wish investigate turbine-level control strategies.

Flow control strategies for vertical-axis wind turbines aim at influencing the angle of attack experienced by the blade. This is achieved by altering the blade kinematics or implementing surface flow control devices, such as plasma actuators or suction slots [88]. One way to alter the blade kinematics is to control the turbine's rotational velocity. This strategy is advantageous because it does not require any hardware modification to the turbine. Intracycle angular velocity control was demonstrated to be an effective strategy to improve wind turbine performance, both experimentally and numerically [23, 100]. A 59 % increase in mean power coefficient was achieved by Strom, Brunton, and Polagye [100] when using angular velocity control compared to a constant angular velocity. This method has two important technical limitations. Changing the angular velocity requires the generator to function as a motor when the control requires a velocity increase that is not supported by the wind conditions. An intracycle variation of the angular velocity also aggravates the intermittency of vertical-axis wind turbines, since instantaneous power is proportional to rotational frequency.

Another way to alter the blade kinematics is achieved with dynamic blade pitching. The blade's pitch angle, or the angle between the blade's chord and the tangent line to the blade's path (figure 1.2), has a significant influence on turbine performance. Dynamic blade pitching involves a direct blade-motor drive, allowing complete independence between the blade's pitch angle and the turbine's rotation. This added versatility is very advantageous to adapt the blade's kinematics to rapidly changing weather conditions while maintaining a constant angular velocity and a high power coefficient. Constant and predictable power output is a highly regarded attribute for urban applications and facilitates the implementation of vertical-axis turbine contribution to the electrical grid. Few studies have investigated dynamic blade pitching for vertical-axis wind turbines. A low-order model of turbine blade performance was coupled with a genetic algorithm optimiser to maximise power performance, demonstrating a 30 % increase in the annual energy production [82]. A numerical optimisation based on computational fluid dynamics (CFD) simulations achieved power coefficients of 0.64 and 0.72 at tip-speed ratios 4.5 and 3.4 [65].

We present an experimental multi-objective optimisation of blade pitching kinematics for vertical-axis wind turbine performance enhancement for on and off-design operating conditions. We actuate the turbine blade to control the formation of vortices to maximise power production and minimise undesired load transients. Our experimental apparatus allows the implementation of genetic algorithm-based optimisation, performing thousands of experiments to identify optimal blade-pitching strategies. These findings highlight the remarkable potential of blade pitching to help vertical-axis wind turbines reach commercial viability. The discussion offers guidelines to generalise our findings to other turbine geometries.

7.2 Experimental methods

We couple a genetic algorithm optimiser [17] to a scaled-down vertical-axis wind turbine model with dynamic blade pitching capabilities. The wind turbine blade is placed at the centre of the test section of a water channel and performs fully automated experiments to seek optimal blade pitching kinematics. An overview the experimental apparatus used for this investigation is presented in figure 7.1. The force and flow measurement methodology is the same as that described in chapter 3. We provide information on the parametrisation of blade pitching kinematics and the genetic algorithm hereafter.

7.2.1 Kinematics parametrisation

We parametrise the pitching kinematics using a sum of 3 sine waves with frequencies that are multiples of the main rotational frequency ω :

$$\alpha_{\text{pitch}}(t) = A_0 + \sum_{n=1}^3 A_n \sin(n\omega t + \theta_n), \quad (7.1)$$

where A_0 is a fixed angle offset, A_n is the amplitude and θ_n the phase shift of the n^{th} sine wave. The seven parameters are bounded by the values listed in table 7.1. These bounds were chosen to allow the optimiser to explore a comprehensive parameter space while ensuring the turbine's integrity. Additional flexibility was given to the higher tip-speed ratio $\lambda = 3.2$ since the geometric angle of attack variation α_{geo} has lower amplitude and yields lower stress on the turbine's structure.

Table 7.1: Lower and upper boundaries (LB and UB) constraining the parameter space for the generation of pitching profile using equation (7.1).

	A_0	A_1	A_2	A_3	θ_1	θ_2	θ_3
$\text{LB}_{\lambda=1.5}$	-10°	-31°	-15°	-8°	-45°	-60°	-60°
$\text{UB}_{\lambda=1.5}$	10°	0°	15°	8°	45°	60°	60°
$\text{LB}_{\lambda=3.2}$	-10°	-25°	-15°	-8°	-45°	-60°	-60°
$\text{UB}_{\lambda=3.2}$	10°	25°	15°	8°	45°	60°	60°

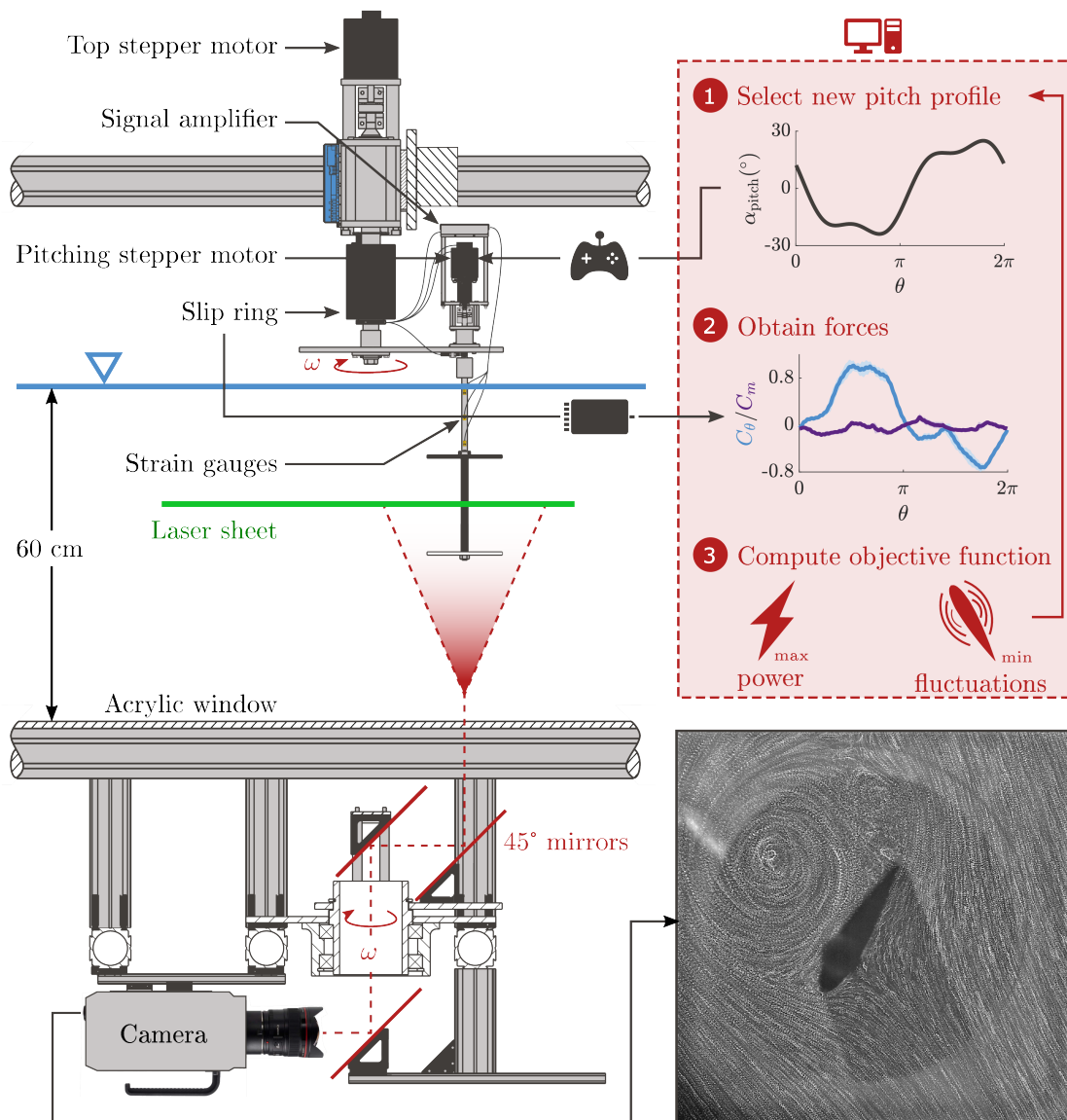


Figure 7.1: Cross-section view of the experimental set-up including the wind turbine model, the light sheet, the rotating mirror system and high-speed camera for particle image velocimetry (PIV). The turbine model and the camera have been omitted from the cross-section. The camera's field of view is shown in the bottom right. Here, the field of view was generated by computing the maximum intensity image over 50 images taken during the formation of a large leading-edge vortex. Similarly to a long exposure shot, it shows streaklines developing around the blade during the occurrence of dynamic stall. PIV was only used to understand the flow physics allowing the best individuals to perform well. The optimisation only required force measurements. The routine followed by the genetic algorithm for each individual is outlined in the top right part of the figure. At the beginning, of each generation, the genetic algorithm generates a new population comprised of 60 individuals based on the performance on the previous generation. For each individual, the pitch profile is uploaded to the motion controller. The motion controller synchronously actuates the top motor at a constant frequency and executes the requested pitch profile with the pitching motor. When PIV was performed, the motion controller also electronically gears the rotation of the rotating mirrors to the top motor, such that the blade remains in the field of view. Unsteady loads are measured with strain gauges. The signal is amplified on-board and transmitted to a data acquisition system (DAQ) via a slip ring. The computer retrieves physical forces and computes the two objective functions before moving on to the next individual.

7.2.2 Genetic algorithm

We implement an optimisation framework using the MATLAB global optimization toolbox [17]. The optimisation framework is fully automated and can run unsupervised. Genetic algorithms are inspired from the mechanics of natural selection, whereby the algorithm will reward and promote fit individuals, those that score the highest according to a user-defined objective function. Here, we maximise the turbine efficiency and minimise the load fluctuations related to flow separation. Turbine efficiency is quantified with the net power coefficient, obtained using equation (3.8). The numerator becomes the net generated power given by:

$$P_{\text{net}} = \underbrace{F_{\theta}\omega R}_{\text{blade-generated power}} - \underbrace{M_Z\dot{\alpha}}_{\text{actuation-consumed power}} \quad (7.2)$$

where F_{θ} and M_Z are the tangential force and pitching moment experienced by the turbine blade (figure 1.2), and ω and $\dot{\alpha}$ are the turbine's angular velocity and the blade's pitch rate (figures 1.2 and 7.1). The load fluctuations related to flow separation are directly correlated to the pitching moment's standard deviation $\sigma(M_Z)$ (chapter 4), so we use this metric to compute the second objective.

The genetic algorithm iteratively generates generations of 60 individuals characterised by one pitching kinematic parametrised using equation (7.1). The first generation is generated through a random uniform distribution constrained by the lower and upper bounds indicated in table 7.1. One experiment is performed for each individual. We developed a cost-function that performs the pitching kinematics requested by the optimisation solver, retrieves aerodynamic loads from the data acquisition system and calculates the two objective functions. Once all 60 experiments were completed, each individual is ranked according to its combined score across both objective functions. The best individuals are randomly mutated and recombined with other fit individuals to create a new generation of offspring. This new generation includes: individuals that are clones of the previous generation's elite (5 %), individuals that are a crossover of two parents (60 %) and mutated individuals from the previous generation (35 %). This procedure is iterated until the optimisation has converged. Here, we assume convergence when neither of our two objective have improved more than 5 % for the last 10 generations. This objective was reached within 18 and 26 generations at tip-speed ratios $\lambda = 1.5$ and $\lambda = 3.2$ respectively.

7.2.3 Flow conditions

We performed two pitching kinematics optimisations at a chord-based Reynolds number $Re_c = 50\,000$. The first optimisation was conducted at off-design operating tip-speed ratio $\lambda = 1.5$, where the non-actuated turbine blade is expected to undergo deep dynamic stall. The second was conducted at an on-design operating condition $\lambda = 3.2$, for which the non-actuated wind turbine blade has the highest mean power coefficient (chapter 4).

For each multi-objective optimisation, we obtain a set of optimal pitching kinematic solutions forming the Pareto front. An individual is considered Pareto-optimal and part of the Pareto

front when no other individual scored better than the said individual for both objectives. We cluster the Pareto-optimal kinematics to facilitate the analysis. We perform time-resolved particle image velocimetry (PIV) to support the analysis of the flow physics of the optimal kinematics. We compare and contrast the flow structures forming around the turbine blade for both optimally actuated and non-actuated individuals at both tip-speed ratios.

7.3 Results

7.3.1 Performance overview

Blade pitching yields a substantial increase in power coefficient compared to the non-actuated case for both objectives and at both off and on-design tip-speed ratios λ . The mean power coefficient of Pareto-optimal individuals show a performance enhancement by a factor ranging from 2.5 to 3.2 at $\lambda = 1.5$ (figure 7.2(a)) and between 0.9 to 3.1 at $\lambda = 3.2$ (figure 7.3(a)) compared to their respective non-actuated cases. Both optimisations converged to a maximum power coefficient improvement around 3, suggesting blade pitching has the potential to improve vertical-axis wind turbine performance across operating tip-speed ratios by a similar factor.

Blade pitching also helped protect the wind turbine from undesired load fluctuations related to the occurrence of flow separation from the blade surface, particularly for the off-design tip speed ratio $\lambda = 1.5$. At $\lambda = 1.5$, optimal individuals reduce the pitching moment standard deviation between 60 % and 77 % (figure 7.2(a)). With the significant power performance enhancement, blade pitching becomes an attractive solution to keep wind turbines safe and efficient at low tip-speed ratios. At the on-design tip-speed ratio $\lambda = 3.2$, optimal individuals scored a pitching moment standard deviation between 0.7 and 1.9 times the value scored by the non-actuated wind turbine (figure 7.3(a)). This result suggests that the most power-extracting individuals had to accept some load fluctuations to increase power production. The non-actuated case features a very low pitching moment standard deviation, and a 1.9 times increase remains acceptable for the turbine's structural integrity. Some individuals managed a 2.8 times power coefficient improvement while keeping the pitching moment standard deviation at the same low level compared to the non-actuated case (figure 7.3(c)).

A common trait for all high-scoring kinematics is that they achieve a significantly higher power production in the downwind half of the blade's rotation ($180^\circ \leq \theta < 360^\circ$). Top-scoring individuals in the off-design optimisation ($\lambda = 1.5$) achieve the same magnitude maxima in power production in both the upwind and downwind halves ($\Delta C_{p,\max} \approx 0$, figure 7.2 (a)). The balance in power generation suggests optimal pitching kinematics found a strategy to mitigate the undesirable consequences of dynamic stall, which generally limit the blade's performance for most of the downwind half. This strategy is not at the expense of overall power production since all Pareto-optimal individuals scored at least 2.5 times the mean power coefficient of the non-actuated case. Pareto-optimal individuals harness the lift-enhancing perks of forming a leading-edge vortex while mitigating undesirable consequences related to its separation and interaction with the turbine blade.

At the on-design tip-speed ratio $\lambda = 3.2$, optimal individuals surprisingly achieve a higher power coefficient in the downwind half than in the upwind half ($\Delta C_{P,\max} \approx -2$, figure 7.3 (a)). We wish to select optimal individuals from both optimisations to perform flow measurements and uncover how optimal blade kinematics manipulate the flow structures to improve turbine performance. Looking at all tested kinematics, we distinguish two typical pitch profiles that yielded Pareto-optimal performance. The kinematics were clustered using a standard k-means algorithm with two clusters for both optimisation runs (figures 7.2 and 7.3 (b)). Kinematics that belong to the same cluster sit next to each other in the Pareto front, apart from a small overlap observed in the bottom left corner of the Pareto front at $\lambda = 3.2$ (figure 7.3 (b)).

The first cluster provides optimal solutions to maximise the blade's torque production. For

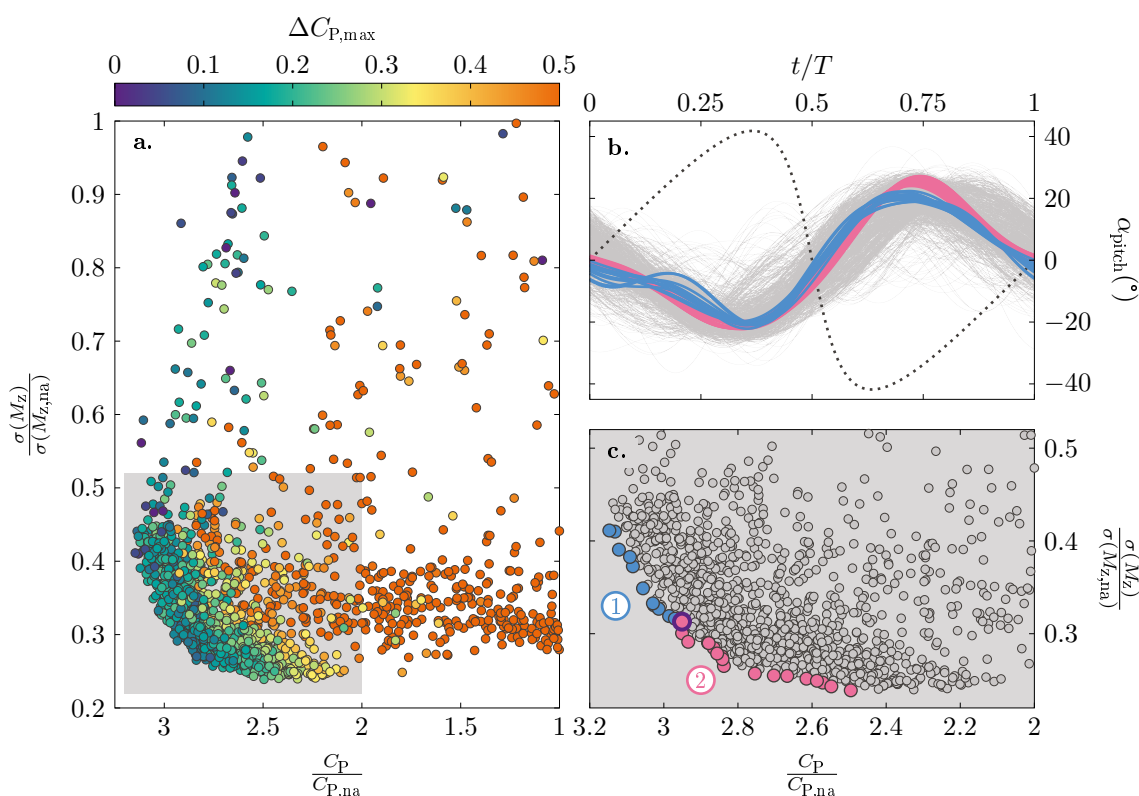


Figure 7.2: Performance overview for all 1860 tested individuals at tip-speed ratio $\lambda = 1.5$, with a focus on optimal kinematics. (a) The two optimisation objectives in this study, namely the mean power coefficient and pitching moment standard deviation, are shown as a parametric scatter plot. Optimisation objectives are conventionally formulated as objectives to minimise, so the power coefficient axis was inverted. Both axes were normalised by the performance of the non-actuated case that scored a mean power coefficient of $C_{P,na} = 0.08$ and a pitching moment standard deviation of $\sigma(M_{z,na}) = 0.03$ N. Normalising the axes offers a simple way to assess the improvement achieved by actuation, as the values shown on the axes represent a net improvement ratio compared to the non-actuated case. The colour bar represents the difference in peak power coefficient between the upwind and downwind halves of the blade's rotation $\Delta C_{P,\max}$. (b) Temporal evolution of the blade pitch angle for all individuals (background, light grey) and Pareto-optimal individuals (foreground, coloured). The colours represent individuals belonging to the same cluster. (c) Zoomed-in view of top-performing individuals (background, light grey) and Pareto-optimal individuals (foreground, coloured). The colours represent individuals belonging to the same cluster and correspond to those in (b). We performed flow measurements on the individual with a greater marker edge line-width, results are shown in figure 7.4.

Chapter 7. Optimal blade pitching kinematics

both tip-speed ratio cases $\lambda = 1.5$ and 3.2 , individuals that scored the highest power coefficients rely on higher order terms from the sin-series described in equation (7.1), creating more intricate kinematics (figures 7.2 and 7.3 (b)). These complex kinematics performed well in our controlled laboratory environment but are less likely to be generalised to a real field flow than simpler kinematics. High-power individuals tend to experience a significant increase in pitching moment standard deviation for a slight increase in power coefficient, particularly for the on-design case (figures 7.2 and 7.3 (c)). The pitching moment standard deviation measures the prominence of undesirable load fluctuations related to flow separation, which create heavy, transient and unpredictable stress on the turbine's structure. Though a high power coefficient is desirable in the design of a wind turbine, one can hardly justify sacrificing

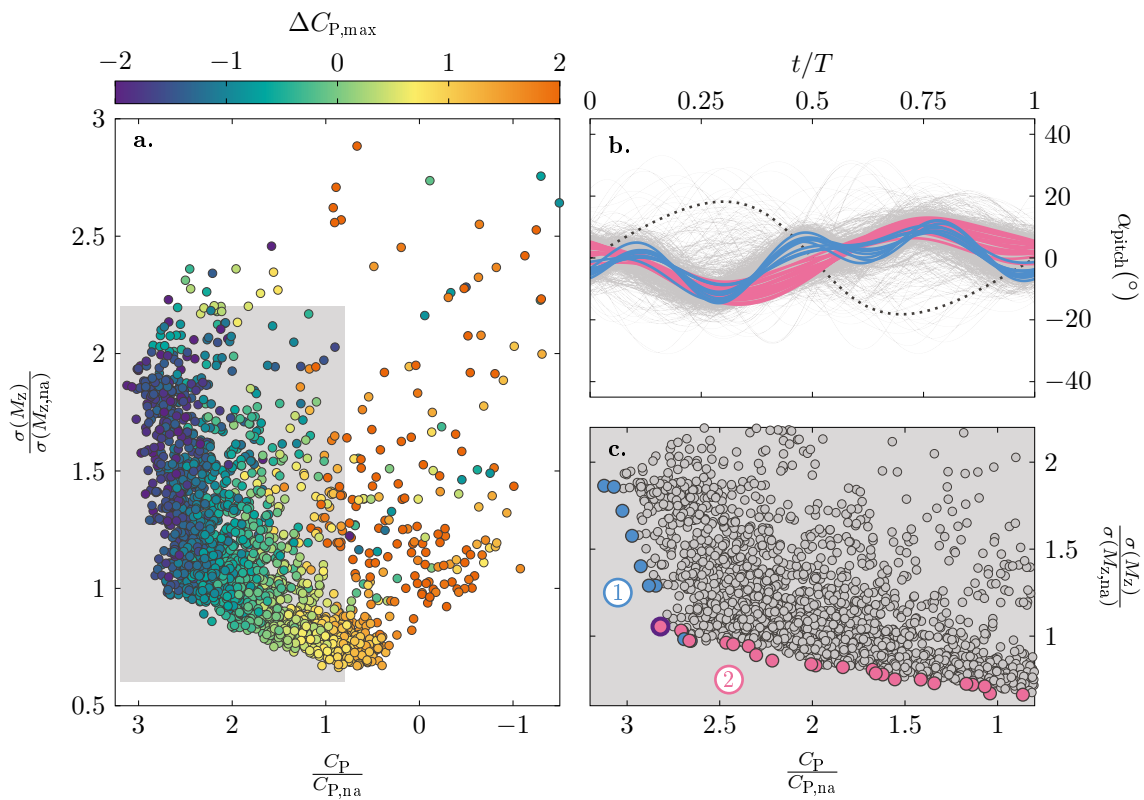


Figure 7.3: Performance overview for all 2280 tested individuals tip-speed ratio $\lambda = 3.2$, with a focus on optimal kinematics. (a) The two optimisation objectives in this study, namely the mean power coefficient and pitching moment standard deviation, are shown as a parametric scatter plot. Optimisation objectives are conventionally formulated as objectives to minimise, so the power coefficient axis was inverted. Both axes were normalised by the performance of the non-actuated case that scored a mean power coefficient of $C_{p,na} = 0.28$ and a pitching moment standard deviation of $\sigma(M_{z,na}) = 0.007$ N. Normalising the axes offers a simple way to assess the improvement achieved by actuation, as the values shown on the axes represent a net improvement ratio compared to the non-actuated case. The colour bar represents the difference in peak power coefficient between the upwind and downwind halves of the blade's rotation $\Delta C_{p,max}$. (b) Temporal evolution of the blade pitch angle for all individuals (background, light grey) and Pareto-optimal individuals (foreground, coloured). The colours represent individuals belonging to the same cluster. (c) Zoomed-in view of top-performing individuals (background, light grey) and Pareto-optimal individuals (foreground, coloured). The colours represent individuals belonging to the same cluster and correspond to those in (b.). We performed flow measurements on the individual with a greater marker edge line-width, results are shown in figure 7.5.

the turbine's structural integrity for limited gains in the power coefficient.

The second cluster provides optimal solutions to minimise the standard deviation of the pitching moment, referred to as the safe individuals. Both optimisation runs converged to comparable pitching kinematics to yield safe individuals, dominated by the first term in the sin-series used to parametrise pitching kinematics (equation (7.1)). Safe individuals that scored the highest power coefficient represent an excellent compromise: they achieve a 2.8 times power enhancement while reducing undesired load fluctuations by 70 % for the off-design case (figure 7.2 (c)) and maintaining the same levels for the on-design case (figure 7.3 (c)) compared to their respective non-actuated cases. The rest of our analysis will focus on the safe individuals with the highest power coefficients for both optimisation cases, circled by a thick line in figures 7.2 and 7.3 (c), hereafter referred to as optimal individuals. We performed time-resolved flow and unsteady force measurements for both optimal individuals to uncover the flow physics behind the performance enhancement.

7.3.2 Off-design flow control

We compare the interplay between the power coefficient and flow structures for the non-actuated turbine blade and the optimal pitching blade in figure 7.4. The non-actuated case is characterised by the occurrence of dynamic stall. As the blade climbs upwind, we note the formation of a leading-edge vortex that creates suction and allows for a peak in power production around $\theta = 80^\circ$. The large-scale vortex moves away from the leading edge, redirecting the aerodynamic force towards the radial direction. The vortex eventually lifts off from the blade, leading to a significant drag excursion and post-stall load fluctuations. In the downwind half, the flow remains fully separated, yielding sporadic regions of positive power coefficient.

Optimal pitching kinematics begin the turbine's rotation by pitching the blade downwards, effectively reducing the blade's angle of attack. This manoeuvre delays flow separation from the blade surface and redirects the aerodynamic force towards the direction tangential to the blade's path. First signs of a vortex are seen in the vorticity field at $\theta = 90^\circ$. The blade continues pitching down until $\theta = 130^\circ$, helping the vortex stay attached to the blade's leading edge by maintaining a moderate angle of attack. The blade yields a significant region of power production by keeping a concentrated vortex at its leading edge for a prolonged portion of the rotation. As the blade enters the downwind region, the blade executes a rapid pitch-up manoeuvre, forcing the vortex to shed into the blade's wake. The pitch-up manoeuvre ends at $\theta = 260^\circ$, allowing flow reattachment as evidenced by the lack of vorticity in the blade's surroundings at $\theta = 270^\circ$. The blade forms a second leading-edge vortex as it starts facing the wind when the effective velocity is the largest. This second vortex yields a peak in power production as significant as the one achieved by the first leading-edge vortex.

The optimal pitching kinematics achieve two distinct power production regions and a much smoother power curve. There are two essential features to the optimal pitch profile. The pitch-down manoeuvre delays flow separation, perfectly timing the shedding of the first leading-edge vortex and redirecting the aerodynamic force forwards in the upwind half. The pitch-up manoeuvre allows early flow reattachment minimising undesired load fluctuations

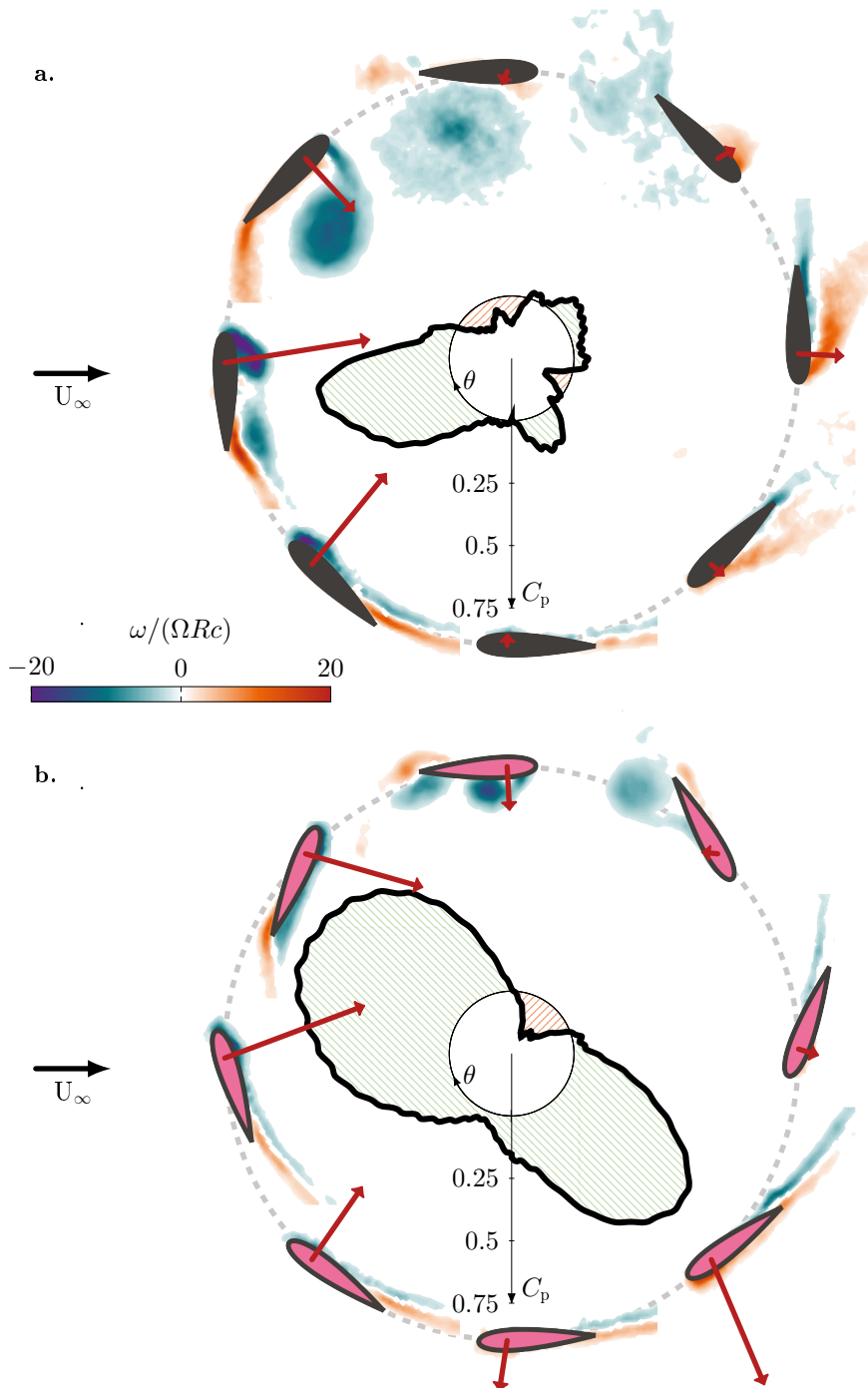


Figure 7.4: Polar plot comparison of the phase-averaged power coefficient for both the non-actuated case (a) and the optimal kinematics (b) at tip-speed ratio $\lambda = 1.5$. Phase-averaged normalised vorticity fields are shown at eight equally spaced azimuthal positions ($\theta = [0 : 45 : 360^\circ]$) to illustrate the development of flow structures for both individuals. The total aerodynamic force acting on the blade at the various azimuthal locations is depicted by arrows starting from the blade's quarter-chord. The length of the arrows indicates the relative magnitude of the force. The hatched regions \square and \square represent regions of torque generation and dissipation respectively. The blade's quarter-chord circular path is shown by a light grey dashed line.

and enabling the formation of a second leading-edge vortex.

7.3.3 On-design flow control

We compare the development of the power coefficient and the vorticity fields for the non-actuated blade and the optimal pitching blade operating at tip-speed ratio $\lambda = 3.2$ in figure 7.5. The non-actuated blade is characterised by the occurrence of light stall. Compared to the deep stall $\lambda = 1.5$ case, the shear-layer rolls up into a vortex much later, around $\theta = 90^\circ$. The vortex results in a peak in power production and sheds before growing into a large-scale dynamic stall vortex. As the blade enters the downwind half, the flow re-attaches to the blade surface and a second vortex forms at the leading edge around $\theta = 270^\circ$. The second leading-edge vortex is smaller and less coherent than the first one but still results in a second region of positive power coefficient.

The influence of the actuation on the development of flow structures is not as trivial here compared to the off-design case. Nevertheless, optimal pitching kinematics use the same mechanisms to enhance power production on design. The blade first executes a pitch-down manoeuvre that redirects the aerodynamic force towards the direction tangential to the blade path. Here, reducing the angle of attack is arguably more of a sacrifice since the actuated blade forms a smaller and weaker vortex, generating slightly less torque than the non-actuated blade in the upwind half. The actuated blade is arguably willing to sacrifice some prolificity of the first leading-edge vortex to better prepare for the second one. Forming a small vortex that quickly sheds allows for flow reattachment to occur in the early downwind half. The blade executes a pitch-up manoeuvre forcing the formation of the second leading-edge vortex at $\theta = 270^\circ$. As the blade starts facing the wind and experiences an increase in effective flow velocity, the second vortex grows stronger and yields a substantial peak in power production at $\theta = 315^\circ$.

7.4 Discussion

We demonstrated that blade pitching is the ideal flow control strategy to enhance vertical-axis wind turbine performance. In a controlled laboratory environment, blade pitching achieved a threefold increase in turbine power coefficient at both on and off-design tip-speed ratios compared to non-actuated turbines. At off-design conditions, the blade actuation mitigated post-stall symptoms, reducing undesirable load fluctuation by 70 % compared to the non-actuated case. These experiments demonstrate the potential blade pitching has to improve turbine performance across their operating envelope.

Two manoeuvres allowed optimal pitching kinematics to improve turbine performance at both tested operating conditions: a pitch-down manoeuvre during the upwind half and a pitch-up manoeuvre during the downwind half. Both manoeuvres enable a crucial mechanism in power enhancement: redirecting the total aerodynamic force towards the forward direction tangential to the blade path. Redirecting the total force suggests that actuated blades do not experience a greater force than non-actuated blades but rather make better use of the

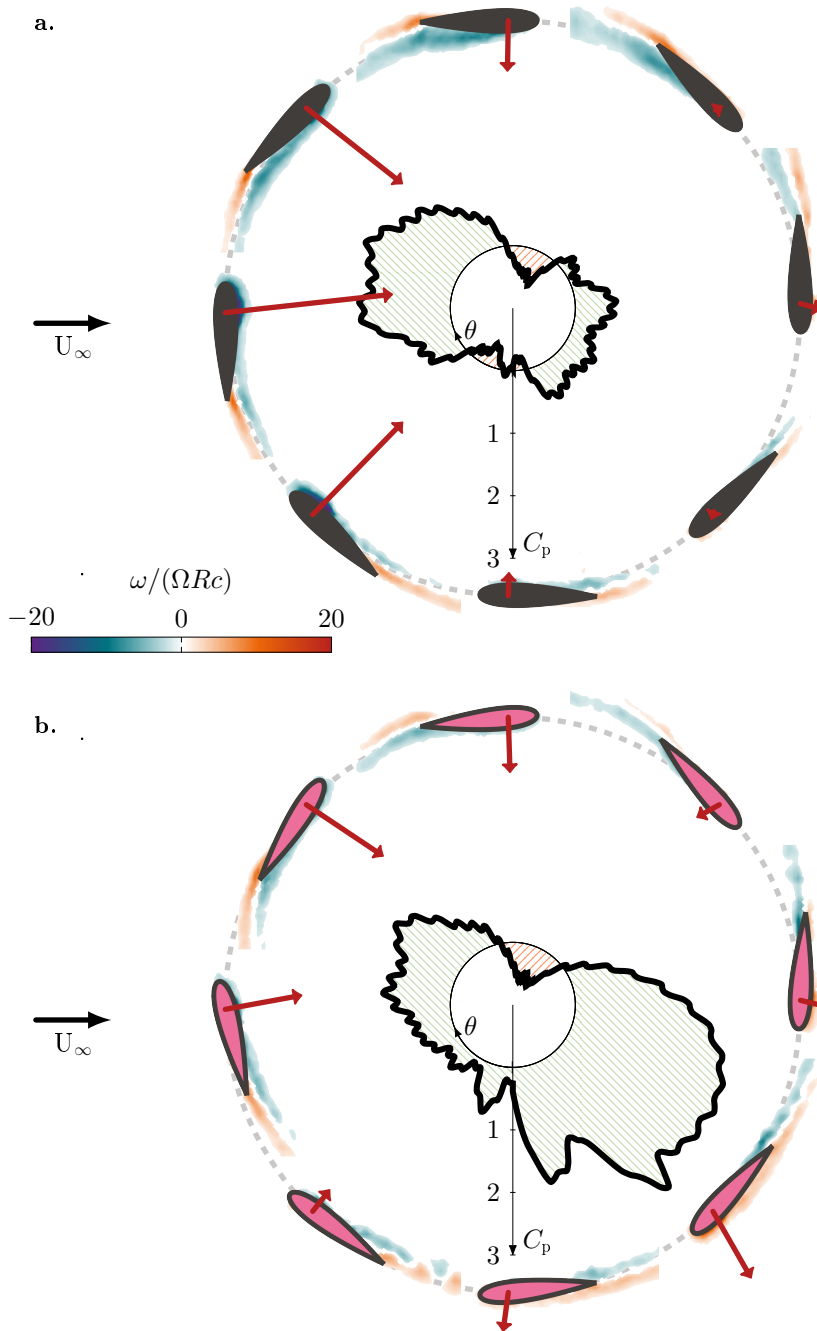


Figure 7.5: Polar plot comparison of the phase-averaged power coefficient for both the non-actuated case (a) and the optimal kinematics (b) at tip-speed ratio $\lambda = 3.2$. Phase-averaged normalised vorticity fields are shown at eight equally spaced azimuthal positions ($\theta = [0 : 45 : 360^\circ]$) to illustrate the development of flow structures for both individuals. The total aerodynamic force acting on the blade at the various azimuthal locations is depicted by arrows starting from the blade's quarter-chord. The length of the arrows indicates the relative magnitude of the force. The hatched regions \square and \square represent regions of torque generation and dissipation respectively. The blade's quarter-chord circular path is shown by a light grey dashed line.

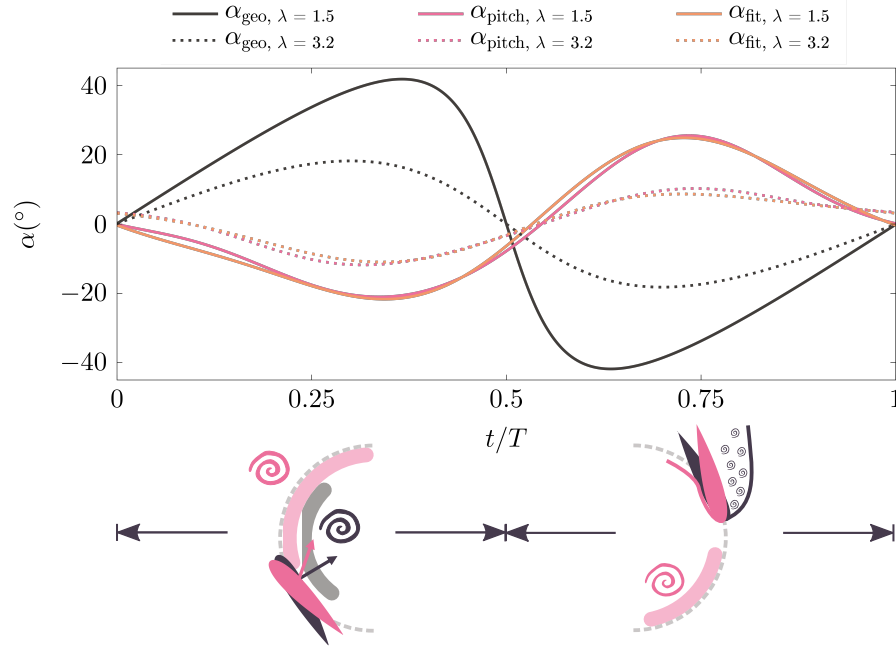


Figure 7.6: Graphic summary of optimal pitching kinematics and flow physics enabling performance enhancement. We show the geometric angle of attack α_{geo} calculated using equation (1.2) and the optimal pitching profile α_{pitch} obtained from optimisations performed at both tip-speed ratios $\lambda = 1.5$ and 3.2 . We fit the two optimal pitching kinematics using a simplified empirical sum of two sin waves (equation (7.3)). Both fitted profiles were obtained by assigning $A_1 = -\frac{1}{2}\alpha_{\text{geo,max}}$ and $A_2 = \frac{1}{8}\alpha_{\text{geo,max}}$, where $\alpha_{\text{geo,max}}$ is the amplitude of the geometric angle of attack variation. Phase-lags $\theta_{1,2}$ were tuned such that $\alpha_{\text{geo,max}}$ and $\alpha_{\text{pitch,min}}$ occur at the same time. This fit is suggested as a starting point pitch profile for any blade pitching application that cannot afford a large parameter-space optimisation. Key flow physics that enable performance enhancement are depicted at the bottom of the figure. In the upwind half ($0 \leq t/T < 0.5$), the pitch-down manoeuvre re-orientates the aerodynamic force to maximise torque contribution. Vortex formation is perfectly timed such that the vortex is shed at mid-rotation and avoids extended blade-vortex interaction. In the downwind half ($0.5 \leq t/T < 1$), the pitch-up manoeuvre encourages flow reattachment and enables the formation of a second coherent leading-edge vortex, yielding a second power production region.

experienced force. This mechanism increases power production while reducing structural stress. The upwind pitch-down delays the occurrence of flow separation, perfectly timing the shedding of the first leading-edge vortex. Vortex timing is critical at off-design conditions, where the non-actuated blade suffers from extended interaction with the shed dynamic stall vortex. The actuated blade sheds its vortex halfway through turbine rotation, limiting blade-vortex interaction to a brief period. The downwind pitch-up encourages early flow reattachment and the formation of a second leading-edge vortex, yielding a second region of high power production.

The idealisation of our experimental conditions limits the direct implementation of our findings to field applications. We performed experiments in a controlled environment using a motor-driven, single-bladed wind turbine model. Using a motor-driven turbine is perfectly suitable to study blade-level flow physics, particularly at low tip-speed ratios where the motor is likely to have mimicked the role of a generator on a field wind turbine [3]. Single-blade turbine models are also often used in literature to investigate blade-level physics. Extending to a multiple-blade unit is unlikely to significantly impact the power curve, as demonstrated

in [100], particularly in the upwind half of the turbine rotation where the blade interacts with unperturbed flow. We also perform experiments at a relatively low Reynolds number of 50 000. The dynamic stall and flow separation timescales are independent of the Reynolds number [5]. Increasing the Reynolds number may slightly affect the amplitude of optimal pitching kinematics but not the timing. The blade-level physics are deemed to be largely unaffected by our blockage conditions. The absolute power coefficient values most likely exceed those we would have obtained in an unconfined flow. At the on-design tip-speed ratio $\lambda = 3.2$, the turbine appears closer to a solid cylinder than at low tip-speed ratios. At high tip-speed ratios, blockage effects tend to enhance the absolute power coefficient values. For this reason, we concentrate our analysis on the relative values and improvement compared to the non-actuated case, which is subjected to the same blockage effects as any actuated case. Blockage corrections could be applied to estimate the expected power coefficient for an equivalent unconfined flow. Given the other limitations of our experimental setup compared to a large-scale, flow-driven wind turbine, we do not apply corrections to our data and focus on the relative performance comparison.

Implementing our findings also require field wind turbines fitted with blade pitching capabilities. Full-scale vertical-axis wind turbines with a 750 kW rated power and blade pitching capabilities are already available on the market. Significant interest in low-amplitude dynamically pitching blades for horizontal-axis wind turbines is also driving the industrial development of this technology. From a sensory standpoint, open-loop control only requires knowledge about the wind speed, direction, and the turbine's rotational frequency. This readily available information allows computing the current tip-speed ratio and the wind facing $\theta = 0^\circ$ position. Our findings suggest a rule of thumb to perform pitching kinematics parametrised using a sum of only two sin waves:

$$\alpha_{\text{pitch}}(t) = A_1 \sin(\omega t + \theta_1) + A_2 \sin(2\omega t + \theta_2). \quad (7.3)$$

The two amplitude parameters A_1 and A_2 can be set to $-\frac{1}{2}\alpha_{\text{max}}$ and $\frac{1}{8}\alpha_{\text{max}}$ respectively, where α_{max} is the amplitude of the geometric angle of attack variation experienced at the current operating tip-speed ratio, given by equation (1.2). The two phase-lags are tuned to align the pitch profile minimum $\alpha_{\text{pitch,min}}$ with the geometric angle of attack maximum α_{max} . Though these guidelines are unlikely to yield the optimal kinematics for an arbitrary unit, they represent a sound starting point to improve the power coefficient.

Further work shall extend these findings to implement closed-loop control. Closed-loop control will require gathering feedback from sensory components, such as the strain gauges, to adapt the blade's pitch angle without prior knowledge about the operating conditions. Though this method involves additional costs, it would allow for reaching the full potential of dynamic blade pitching on vertical-axis wind turbines across operating conditions.

CONCLUSION

This thesis investigates the occurrence and control of dynamic stall on vertical-axis wind turbines. The first notable results are on the role of frequency in the temporal development of stall for the case of a pitching wing in a steady free stream. We distinguish three frequency regimes. Very low frequencies have a reduced pitch rate below 1×10^{-4} and do not promote the onset of stall once the blade exceeds its critical angle. The stall delay, or the timespan between the moment the blade exceeds its critical angle and the occurrence of stall, featured a normal distribution centred around 30 convective times. Stall delay becomes independent from pitching frequency for reduced frequencies greater than 0.04. At these high frequencies, the stall delay has a constant value of 4 convective times, which correspond to the universal vortex formation time. Vortex formation time is the shortest amount of time that is required for a blade to stall. The stall delay follows a universal power-law decay for intermediate frequencies. This power law is validated for three pitching wings operating at three different Reynolds numbers $Re \in [75'000 - 920'000]$ and subjected to two different pitching kinematics (ramp-up and sinusoidal).

We conceived an experimental apparatus to obtain time-resolved force and flow measurements on a vertical-axis wind turbine blade for a wide operating envelope. We use this apparatus in a single-blade configuration to investigate the occurrence of stall for tip-speed ratios $\lambda \in [1.2 - 6]$. The turbine blade undergoes high-frequency variation in the angle of attack, and the stall delay follows the same power law as for pitching wings. We map turbine operating conditions to one of three regimes: deep stall, light stall, and no stall. Deep stall occurs on turbine blades when their angle of attack is greater than the blade's critical angle for longer than 4 convective times. For our turbine with a chord-to-diameter ratio of 0.2, deep stall occurs when $\lambda < 2.5$. For $\lambda > 4.5$, the blade did not exceed its critical angle and did not undergo stall. Intermediate tip-speed ratios undergo light stall. Decreasing tip-speed ratios offer higher peak power performance during vortex formation, but post-stall conditions are aggravated. The light stall regime offers VAWT the best compromise in the dynamic stall dilemma as it yields positive tangential forces during the upwind and downwind rotation and reduces load transients by 75 compared to the deep stall regime.

The succession of events during stall and their timescales are well characterised for wings undergoing dynamic stall when subjected to pitching manoeuvres in a steady free stream. The next objective was to characterise the temporal occurrence of stall in the turbine's rotating frame of reference. Parametric proper orthogonal decomposition was performed to identify dominant flow structures common to all tip-speed ratios where the blade experiences dynamic stall. We distinguish and quantify the timespan of six characteristic stall stages: the attached flow, shear-layer growth, vortex formation, upwind stall, downwind stall, and flow reattachment stage. Convective time is a strong candidate to scale the timescales of stall, but further work is required to characterise the effective flow conditions experienced by a wind turbine blade. We demonstrate that the aerodynamic loads hold sufficient sensory information to identify the transition between the stall events for closed-loop control applications.

Lastly, we investigate the potential of blade pitching to enhance vertical-axis wind turbine performance. A static blade-pitch offset of -4° yields a 25 % increase in power coefficient for a tip-speed ratio $\lambda = 1.5$. Passive control strategies do not offer the versatility required to enhance turbine performance across different operating conditions. We investigate dynamic blade pitching using a genetic algorithm optimiser to perform unsupervised wind turbine experiments and seek optimal pitching kinematics at on and off-design operating conditions. Optimal blade kinematics yielded a three-fold power coefficient increase for both wind conditions compared to the non-actuated turbine and a 70 % reduction in structure-threatening load fluctuations at off-design conditions. Particle image velocimetry enabled us to uncover how blade pitching manipulates flow structures to achieve performance enhancement. Optimal pitching kinematics consisted of two manoeuvres: a pitch-down manoeuvre during the upwind half of the turbine rotation and a pitch-up manoeuvre during the downwind half. Both manoeuvres enable a crucial mechanism in power enhancement: redirecting the total aerodynamic force towards the forward direction tangential to the blade path. Redirecting the total force suggests that actuated blades do not experience a greater force than non-actuated blades but rather make better use of the experienced force. This mechanism increases power production while reducing structural stress. The upwind pitch-down delays the occurrence of flow separation, perfectly timing the shedding of the first leading-edge vortex. The downwind pitch-up encourages early flow reattachment and the formation of a second leading-edge vortex, yielding a second region of high power production. Optimal blade pitching can be parametrised using a simple sum of two sin waves. We provide guidelines on the design of a baseline pitch profile for a wind turbine blade operating at an arbitrary tip-speed ratio. Though these guidelines are unlikely to yield the optimal kinematics for an arbitrary unit, they represent a sound starting point to improve the power coefficient.

This thesis leaves many open questions that require further work. Modelling of effective flow conditions acting on a wind turbine blade, particularly at low tip-speed ratios, can play a crucial role in achieving commercial viability. Low-order models that capture the behaviour of a turbine blade undergoing dynamic stall could help the industry design more robust and efficient units. The scaling of turbine flow physics would also benefit from an improved understanding of effective flow conditions. What are the characteristic length and time scales for a wind turbine? How should we define the Reynolds number when comparing our results? Should we vary the incoming flow velocity or the turbine angular velocity when tuning the

tip-speed ratio for a “constant” Reynolds number? What is the angle of attack on a high chord-to-diameter ratio wind turbine blade in a vortex-dominated flow? Are these questions relevant for a rotating wing that experiences a highly unsteady flow?

The flow control results we present are promising. Further work can attract industrial attention towards dynamic blade pitching. Implementing closed-loop control is desirable. Preliminary work has shown that aerodynamic forces are sufficient data to perform closed-loop control on the turbine blade in a controlled laboratory environment. We achieved a power enhancement similar to the open-loop control using cluster-based network modelling on the single-bladed turbine model without prior knowledge about the flow conditions. How do our results extend to a multi-blade turbine model? Does dynamic blade pitching perform well when the turbine is subjected to unsteady wind or gusts? Can closed-loop dynamic pitch control rely on cheaper, more accessible sensors than strain gauges? Is dynamic blade pitching economically viable, even for small-scale urban wind turbines? The advent of data-driven and physics-informed models can enable a breakthrough for vertical-axis wind turbines. The rise of affordable computing power and the industrial development of cost-efficient electric motors and sensors is already motivated by increasingly connected and intelligent machines. Will vertical-axis wind turbines gear up to capture the opportunity to provide power independence to cities and rural areas and meet their potential for off-shore floating wind farms?

BIBLIOGRAPHY

- [1] N. Akhtar et al. “Accelerating deployment of offshore wind energy alter wind climate and reduce future power generation potentials”. In: *Scientific Reports* 11.1 (2021), pp. 1–12. DOI: 10.1038/s41598-021-91283-3.
- [2] P. J. Ansell and K. Mulleners. “Multiscale vortex characteristics of dynamic stall from empirical mode decomposition”. In: *AIAA Journal* 58.2 (2020), pp. 600–617. DOI: 10.2514/1.J057800.
- [3] D. B. Araya and J. O. Dabiri. “A comparison of wake measurements in motor-driven and flow-driven turbine experiments”. In: *Experiments in Fluids* 56.7 (2015), p. 150. DOI: 10.1007/s00348-015-2022-7.
- [4] S. Armstrong, A. Fiedler, and S. Tullis. “Flow separation on a high Reynolds number, high solidity vertical axis wind turbine with straight and canted blades and canted blades with fences”. In: *Renewable Energy* 41 (2012), pp. 13–22. DOI: 10.1016/J.RENENE.2011.09.002.
- [5] F. Ayancik and K. Mulleners. “All you need is time to generalise the Goman–Khrabrov dynamic stall model”. In: *Journal of Fluid Mechanics* 942 (2022), R8. DOI: 10.1017/jfm.2022.381.
- [6] A. A. Ayati et al. “A double-multiple streamtube model for vertical axis wind turbines of arbitrary rotor loading”. In: *Wind Energy Science* 4.4 (2019), pp. 653–662. DOI: 10.5194/WES-4-653-2019.
- [7] P. Bachant and M. Wosnik. “Effects of Reynolds Number on the Energy Conversion and Near-Wake Dynamics of a High Solidity Vertical-Axis Cross-Flow Turbine”. In: *Energies* 9.2 (2016), p. 73. DOI: 10.3390/en9020073.
- [8] R. J. Barthelmie and S. C. Pryor. “Potential contribution of wind energy to climate change mitigation”. In: *Nature Climate Change* 4.8 (2014), pp. 684–688. DOI: 10.1038/nclimate2269.
- [9] M. Benedict et al. “Aerodynamics of a small-scale vertical-axis wind turbine with dynamic blade pitching”. In: *AIAA Journal* 54.3 (2016), pp. 924–935. DOI: 10.2514/1.J052979.
- [10] D. Bensason et al. “Greenberg’s Force Prediction for Vertical-Axis Wind Turbine Blades”. In: *AIAA Journal* (2022), pp. 1–4. DOI: 10.2514/1.J061417.

Bibliography

- [12] A. Bianchini et al. “A computational procedure to define the incidence angle on airfoils rotating around an axis orthogonal to flow direction”. In: *Energy Conversion and Management* 126 (2016), pp. 790–798. DOI: 10.1016/j.enconman.2016.08.010.
- [13] M. Borg, A. Shires, and M. Collu. “Offshore floating vertical axis wind turbines, dynamics modelling state of the art. part I: Aerodynamics”. In: *Renewable and Sustainable Energy Reviews* 39 (2014), pp. 1214–1225. DOI: 10.1016/J.RSER.2014.07.096.
- [14] A. J. Buchner et al. “Dynamic stall in vertical axis wind turbines: Scaling and topological considerations”. In: *Journal of Fluid Mechanics* 841 (2018), pp. 746–766. DOI: 10.1017/jfm.2018.112.
- [15] L. W. Carr, K. W. Mcalister, and W. J. McCroskey. *Analysis of Dynamic Oscillating the Development Stall Based on Airfoil Experiments*. Tech. rep. National Aeronautics and Space Administration, 1977.
- [16] P. Chatelain et al. “Vortex particle-mesh simulations of vertical axis wind turbine flows: from the airfoil performance to the very far wake”. In: *Wind Energy Science* 2 (2017), pp. 317–328. DOI: 10.5194/wes-2-317-2017.
- [17] A. Chipperfield. “The MATLAB Genetic Algorithm Toolbox”. In: *IEE Colloquium on Applied Control Techniques Using MATLAB*. Vol. 1995. IEE, 1995, pp. 10–10. DOI: 10.1049/ic:19950061.
- [18] D. G. Coleman et al. “Parametric Modal Decomposition of Dynamic Stall”. In: *AIAA Journal* 57.1 (2019), pp. 176–190. DOI: 10.2514/1.j057077.
- [19] T. C. Corke and F. O. Thomas. “Dynamic Stall in Pitching Airfoils: Aerodynamic Damping and Compressibility Effects”. In: *Annual Review of Fluid Mechanics* 47.1 (2015), pp. 479–505. DOI: 10.1146/annurev-fluid-010814-013632.
- [20] J. O. Dabiri. “Optimal Vortex Formation as a Unifying Principle in Biological Propulsion”. In: *Annual Review of Fluid Mechanics* 41.1 (2009), pp. 17–33. DOI: 10.1146/annurev.fluid.010908.165232.
- [21] J. O. Dabiri. “Potential order-of-magnitude enhancement of wind farm power density via counter-rotating vertical-axis wind turbine arrays”. In: *Journal of Renewable and Sustainable Energy* 3.4 (2011). DOI: 10.1063/1.3608170.
- [22] M. Dave and J. A. Franck. “Comparison of RANS and LES for a cross-flow turbine in confined and unconfined flow”. In: *Journal of Renewable and Sustainable Energy* 13.6 (2021), p. 064503. DOI: 10.1063/5.0066392.
- [23] M. Dave et al. “Simulations of intracycle angular velocity control for a crossflow turbine”. In: *AIAA Journal* 59.3 (2021), pp. 812–824. DOI: 10.2514/1.J059797.
- [24] D. De Tavernier et al. “Controlling dynamic stall using vortex generators on a wind turbine airfoil”. In: *Renewable Energy* 172 (2021), pp. 1194–1211. DOI: 10.1016/J.RENENE.2021.03.019.
- [25] A. T. Degani, J. D. Walker, and F. T. Smith. “Unsteady separation past moving surfaces”. In: *Journal of Fluid Mechanics* 375 (1998), pp. 1–38. DOI: 10.1017/S0022112098001839.

- [26] P. Delafin et al. “Effect of the number of blades and solidity on the performance of a vertical axis wind turbine”. In: *Journal of Physics: Conference Series* 753.2 (2016), p. 022033. DOI: 10.1088/1742-6596/753/2/022033.
- [27] J. Deparday and K. Mulleners. “Modeling the interplay between the shear layer and leading edge suction during dynamic stall”. In: *Physics of Fluids* 31.10 (2019), p. 107104. DOI: 10.1063/1.5121312.
- [28] T. Doligalski, C. Smith, and J. Walker. “Vortex interactions with walls”. In: *Annual Review of Fluid Mechanics* 26.1 (1994), pp. 573–616.
- [29] R. Dunne, P. J. Schmid, and B. J. McKeon. “Analysis of Flow Timescales on a Periodically Pitching/Surging Airfoil”. In: *AIAA Journal* 54.11 (2016), pp. 3421–3433. DOI: 10.2514/1.J054784.
- [30] R. Dunne and B. J. McKeon. “Dynamic stall on a pitching and surging airfoil”. In: *Experiments in Fluids* 56.8 (2015), pp. 1–15. DOI: 10.1007/s00348-015-2028-1.
- [31] E. Dupont, R. Koppelaar, and H. Jeanmart. “Global available wind energy with physical and energy return on investment constraints”. In: *Applied Energy* 209 (2018), pp. 322–338. DOI: 10.1016/j.apenergy.2017.09.085.
- [32] J. D. Eldredge and A. R. Jones. “Leading-Edge Vortices: Mechanics and Modeling”. In: *Annu. Rev. Fluid Mech* 51 (2019), pp. 75–104. DOI: 10.1146/annurev-fluid-010518.
- [33] M. Elkhoury, T. Kiwata, and E. Aoun. “Experimental and numerical investigation of a three-dimensional vertical-axis wind turbine with variable-pitch”. In: *Journal of Wind Engineering and Industrial Aerodynamics* 139 (2015), pp. 111–123. DOI: 10.1016/j.jweia.2015.01.004.
- [34] C. P. Ellington, C. V. den Berg, and A. P. Willmott. “Leading-edge vortices in insect flight”. In: *Nature* 384.December (1990), pp. 626–630.
- [35] L. Ericsson and J. Reding. “Fluid mechanics of dynamic stall part I. Unsteady flow concepts”. In: *Journal of Fluids and Structures* 2.1 (1988), pp. 1–33. DOI: 10.1016/s0889-9746(88)90116-8.
- [36] S. Eriksson, H. Bernhoff, and M. Leijon. “Evaluation of different turbine concepts for wind power”. In: *Renewable and Sustainable Energy Reviews* 12.5 (2008), pp. 1419–1434. DOI: 10.1016/j.rser.2006.05.017.
- [37] J. Farnsworth et al. “Design and qualification of an unsteady low-speed wind tunnel with an upstream louver system”. In: *Experiments in Fluids* 61.8 (2020), p. 181. DOI: 10.1007/s00348-020-03018-1.
- [38] C. S. Ferreira et al. “Comparison of aerodynamic models for Vertical Axis Wind Turbines”. In: *Journal of Physics: Conference Series* 524.1 (2014), p. 012125. DOI: 10.1088/1742-6596/524/1/012125.
- [39] C. S. Ferreira and F. Scheurich. “Demonstrating that power and instantaneous loads are decoupled in a vertical-axis wind turbine”. In: *Wind Energy* 17.3 (2014), pp. 385–396. DOI: 10.1002/WE.1581.

Bibliography

- [40] N. Fujisawa and S. Shibuya. “Observations of dynamic stall on turbine blades”. In: *Journal of Wind Engineering and Industrial Aerodynamics* 89.2 (2001), pp. 201–214. DOI: 10.1016/S0167-6105(00)00062-3.
- [41] A. Gehrke, G. De Guyon-Crozier, and K. Mulleners. “Genetic Algorithm Based Optimization of Wing Rotation in Hover”. In: *Fluids* 3.3 (2018), p. 59. DOI: 10.3390/FLUIDS3030059.
- [42] K. Gharali and D. A. Johnson. “Dynamic stall simulation of a pitching airfoil under unsteady freestream velocity”. In: *Journal of Fluids and Structures* 42 (2013), pp. 228–244. DOI: 10.1016/j.jfluidstructs.2013.05.005.
- [43] M. Gharib, E. Rambod, and K. Shariff. “A universal time scale for vortex ring formation”. In: *Journal of Fluid Mechanics* 360 (1998), pp. 121–140. DOI: 10.1017/S0022112097008410.
- [44] M. Goman and A. Khrabrov. “State-Space Representation of Aerodynamic Characteristics of an Aircraft at High Angles of Attack”. In: *Journal of Aircraft* 31.5 (1994), pp. 1109–1115. DOI: 10.2514/3.46618.
- [45] J. M. Greenberg. *Airfoil in sinusoidal motion in a pulsating stream*. Tech. rep. 1947.
- [46] G. He et al. “Stall Delay and Leading-Edge Suction for a Pitching Airfoil with Trailing-Edge Flap”. In: *AIAA Journal* 58.12 (2020), pp. 5146–5155. DOI: 10.2514/1.J059719.
- [48] R. F. Huang and H. W. Lee. “Turbulence effect on frequency characteristics of unsteady motions in wake of wing”. In: *AIAA journal* 38.1 (2000), pp. 87–94. DOI: 10.2514/2.926.
- [49] R. F. Huang and C. L. Lin. “Vortex shedding and shear-layer instability of wing at low-Reynolds numbers”. In: *AIAA Journal* 33.8 (1995), pp. 1398–1403. DOI: 10.2514/3.12561.
- [50] “IEEE Standard on Transitions, Pulses, and Related Waveforms”. In: *IEEE Std 181-2003* (2003), pp. 1–60. DOI: 10.1109/IEEESTD.2003.94394.
- [51] International Energy Agency. *Net Zero by 2050*. Tech. rep. 4. Paris: IEA, 2021.
- [52] P. Jamieson. *Innovation in Wind Turbine Design*. John Wiley and Sons, 2011. DOI: 10.1002/9781119975441.
- [53] A. R. Jones and O. Cetiner. “Overview of NATO AVT-282: Unsteady aerodynamic response of rigid wings in gust encounters”. In: *AIAA Scitech 2020 Forum*. 2020, p. 0078.
- [54] J. Kiefer et al. “Dynamic stall at high Reynolds numbers induced by ramp-type pitching motions”. In: *Journal of Fluid Mechanics* 938 (2022), A10. DOI: 10.1017/jfm.2022.70.
- [55] T. Kinsey and G. Dumas. “Parametric Study of an Oscillating Airfoil in a Power-Extraction Regime”. In: *AIAA* 46.6 (2008), pp. 1318–1330. DOI: 10.2514/1.26253.
- [56] J. Kissing et al. “Insights into leading edge vortex formation and detachment on a pitching and plunging flat plate”. In: *Experiments in Fluids* 61.9 (2020), p. 208. DOI: 10.1007/s00348-020-03034-1.
- [57] T. Kiwata et al. “Performance of a Vertical Axis Wind Turbine with Variable-Pitch Straight Blades utilizing a Linkage Mechanism”. In: *Journal of Environment and Engineering* Vol. 5.No. 1 (2010), pp. 213–225. DOI: 10.1299/jee.5.213.

- [58] A. Laneville and P. Vittecoq. “Dynamic Stall: The Case of the Vertical Axis Wind Turbine”. In: *Article in Journal of Solar Energy Engineering* 108 (1986). DOI: 10.1115/1.3268081.
- [60] S. Le Fouest, J. Deparday, and K. Mulleners. “The dynamics and timescales of static stall”. In: *Journal of Fluids and Structures* 104 (2021), p. 103304. DOI: 10.1016/j.jfluidstructs.2021.103304.
- [61] S. Le Fouest, D. Fernex, and K. Mulleners. “Timescales of dynamic stall development on a vertical-axis wind turbine blade”. In: *arXiv* (2022). DOI: 10.48550/arxiv.2210.16259.
- [62] S. Le Fouest and K. Mulleners. “The dynamic stall dilemma for vertical-axis wind turbines”. In: *Renewable Energy* 198 (2022), pp. 505–520. DOI: 10.1016/j.renene.2022.07.071.
- [63] J. G. Leishman and T. S. Bcddoes. “A semi-empirical model for dynamic stall”. In: *Journal of the American Helicopter Society* 34.3 (1989), pp. 3–17. DOI: 10.4050/JAHS.34.3.
- [64] J. G. Leishman. “Challenges in modelling the unsteady aerodynamics of wind turbines”. In: *Wind Energy* 5.2-3 (2002), pp. 85–132. DOI: 10.1002/we.62.
- [65] C. Li et al. “Optimization of blade pitch in H-rotor vertical axis wind turbines through computational fluid dynamics simulations”. In: *Applied Energy* 212.July 2017 (2018), pp. 1107–1125. DOI: 10.1016/j.apenergy.2017.12.035.
- [66] J. L. Lumley. *Stochastic tools in turbulence*. Courier Corporation, 2007.
- [67] J. K. Lundquist et al. “Costs and consequences of wind turbine wake effects arising from uncoordinated wind energy development”. In: *Nature Energy* 4 (2019), pp. 26–34. DOI: 10.1038/s41560-018-0281-2.
- [68] H. A. Madsen. “The actuator cylinder - a flow model for vertical axis wind turbine.” PhD thesis. Aalborg University, Denmark, 1982. DOI: 10.13140/RG.2.1.2512.3040.
- [69] K. W. McAlister, L. W. Carr, and W. J. McCroskey. *Dynamic stall experiments on the NACA 0012 airfoil*. Tech. rep. 1978.
- [70] W. McCroskey and R. Fisher. “Detailed aerodynamic measurements on a model rotor in the blade stall regime”. In: *Journal of the American Helicopter Society* 17.1 (1972), pp. 20–30. DOI: 10.4050/jahs.17.1.20.
- [71] W. J. McCroskey. *The phenomenon of dynamic stall*. Tech. rep. 1981.
- [72] W. J. McCroskey. “Unsteady airfoils”. In: *Annual review of fluid mechanics* 14.1 (1982), pp. 285–311.
- [73] G. E. McCullough and Donald Gault. *Examples of Three Representative Types of Airfoil-sectionstall at Low Speed*. Tech. rep. National Advisory Committee For Aeronautics, 1951.
- [74] P. G. Migliore, W. P. Wolfe, and J. B. Fanucci. “Flow Curvature Effects on Darrieus Turbine Blade Aerodynamics.” In: *Journal of energy* 4.2 (1980), pp. 49–55. DOI: 10.2514/3.62459.
- [75] M. A. Miller et al. “Vertical-axis wind turbine experiments at full dynamic similarity”. In: *J. Fluid Mech* 844 (2018), pp. 707–720. DOI: 10.1017/jfm.2018.197.

Bibliography

- [76] K. Mulleners, P. Mancini, and A. R. Jones. “Flow Development on a Flat-Plate Wing Subjected to a Streamwise Acceleration”. In: *AIAA Journal* 55.6 (2017), pp. 2118–2122. DOI: 10.2514/1.J055497.
- [77] K. Mulleners and M. Raffel. “Dynamic stall development”. In: *Experiments in Fluids* 54.2 (2013), pp. 1–9. DOI: 10.1007/s00348-013-1469-7.
- [78] K. Mulleners and M. Raffel. “The onset of dynamic stall revisited”. In: *Experiments in Fluids* 52.3 (2012), pp. 779–793. DOI: 10.1007/s00348-011-1118-y.
- [79] P. Ouro, T. Stoesser, and L. Ramirez. “Effect of blade cambering on dynamic stall in view of designing vertical axis turbines”. In: *Journal of Fluids Engineering* 140.June (2018), pp. 1–12. DOI: 10.1115/1.4039235.
- [80] I. Paraschivoiu. “Double-Multiple Streamtube Model for Studying Vertical-Axis Wind Turbines”. In: *Journal of Propulsion and Power* 4.4 (1988), pp. 370–378.
- [81] I. Paraschivoiu and F. Delclaux. “Double multiple streamtube model with recent improvements (for predicting aerodynamic loads and performance of Darrieus vertical axis wind turbines)”. In: *Journal of Energy* 7.3 (1983), pp. 250–255. DOI: 10.2514/3.48077.
- [82] I. Paraschivoiu, O. Trifu, and F. Saeed. “H-Darrieus Wind Turbine with Blade Pitch Control”. In: *International Journal of Rotating Machinery* 2009 (2009), pp. 1–7. DOI: 10.1155/2009/505343.
- [83] C. M. Parker, D. B. Araya, and M. C. Leftwich. “Effect of chord-to-diameter ratio on vertical-axis wind turbine wake development”. In: *Experiments in Fluids* 58.12 (2017), pp. 1–11. DOI: 10.1007/s00348-017-2451-6.
- [84] C. M. Parker and M. C. Leftwich. “The effect of tip speed ratio on a vertical axis wind turbine at high Reynolds numbers”. In: *Experiments in Fluids* 57.5 (2016), pp. 1–11. DOI: 10.1007/S00348-016-2155-3/FIGURES/9.
- [85] M. Raffel et al. *Particle Image Velocimetry*. Berlin, Heidelberg: Springer Berlin Heidelberg, 2007. DOI: 10.1007/978-3-540-72308-0.
- [86] *Renewable Energy Market Update 2022*. Tech. rep. International Energy Agency, 2022, pp. 1–29.
- [87] A. Rezaeiha, I. Kalkman, and B. Blocken. “Effect of pitch angle on power performance and aerodynamics of a vertical axis wind turbine”. In: *Applied Energy* 197 (2017), pp. 132–150. DOI: 10.1016/j.apenergy.2017.03.128.
- [88] A. Rezaeiha, H. Montazeri, and B. Blocken. “Active flow control for power enhancement of vertical axis wind turbines: Leading-edge slot suction”. In: *Energy* 189 (2019), p. 116131. DOI: 10.1016/j.energy.2019.116131.
- [89] A. Rezaeiha, H. Montazeri, and B. Blocken. “Characterization of aerodynamic performance of vertical axis wind turbines: Impact of operational parameters”. In: *Energy Conversion and Management* 169 (2018), pp. 45–77. DOI: 10.1016/J.ENCONMAN.2018.05.042.
- [90] D. E. Rival et al. “Characteristic length scales for vortex detachment on plunging profiles with varying leading-edge geometry”. English. In: *Experiments in Fluids* 55 (2014), p. 1660. DOI: 10.1007/s00348-013-1660-x.

- [91] A. Roshko. “Experiments on the flow past a circular cylinder at very high Reynolds number”. In: *Journal of Fluid Mechanics* 10.3 (1961), pp. 345–356. DOI: 10.1017/S0022112061000950.
- [92] H. Ross and B. Polagye. “An experimental assessment of analytical blockage corrections for turbines”. In: *Renewable Energy* 152 (2020), pp. 1328–1341. DOI: 10.1016/j.renene.2020.01.135.
- [93] I. Scherl et al. “Geometric and control optimization of a two cross-flow turbine array”. In: *Journal of Renewable and Sustainable Energy* 12.6 (2020), p. 064501. DOI: 10.1063/1.50022428.
- [94] F. Scheurich and R. E. Brown. “Effect of Dynamic Stall on the Aerodynamics of Vertical-Axis Wind Turbines”. In: *AIAA Journal* 49.11 (2012), pp. 2511–2521. DOI: 10.2514/1.J051060.
- [95] W. Sheng, R. A. D. Galbraith, and F. N. Coton. “A modified dynamic stall model for low mach numbers”. In: *Journal of Solar Energy Engineering, Transactions of the ASME*. Vol. 130. 2008, pp. 0310131–03101310. DOI: 10.1115/1.2931509.
- [96] C. J. Simão Ferreira et al. “Simulating dynamic stall in a two-dimensional vertical-axis wind turbine: verification and validation with particle image velocimetry data”. In: *Wind Energy* 13.1 (2009), pp. 1–17. DOI: 10.1002/we.330.
- [97] C. Simão Ferreira et al. “Visualization by PIV of dynamic stall on a vertical axis wind turbine”. In: *Experiments in Fluids* 46.1 (2008), pp. 97–108. DOI: 10.1007/s00348-008-0543-z.
- [98] L. Sirovich. “Turbulence and the dynamics of coherent structures. II. Symmetries and transformations”. In: *Quarterly of Applied Mathematics* 45.3 (1987), pp. 573–582.
- [99] M. J. Smith et al. “An Assessment of the State-of-the-Art from the 2019 ARO Dynamic Stall Workshop”. In: *AIAA Aviation forum*. virtual, 2020. DOI: 10.2514/6.2020-2697.
- [100] B. Strom, S. L. Brunton, and B. Polagye. “Intracycle angular velocity control of cross-flow turbines”. In: *Nature Energy* 2.8 (2017), pp. 1–9. DOI: 10.1038/nenergy.2017.103.
- [101] K. Taira et al. “Modal analysis of fluid flows: An overview”. In: *Aiaa Journal* 55.12 (2017), pp. 4013–4041.
- [102] T. Theodorsen. *General theory of aerodynamic instability and the mechanism of flutter*. Tech. rep. NACA-TR-496. National Advisory Committee for Aeronautics, 1979, pp. 291–311. DOI: 10.1016/s0016-0032(35)92022-1.
- [103] D. Weihs. “Hydromechanics of Fish Schooling”. In: *Nature* 241.5387 (1973), pp. 290–291. DOI: 10.1038/241290a0.
- [104] S. Xie et al. “Benefits of collocating vertical-axis and horizontal-axis wind turbines in large wind farms”. In: *Wind Energy* 20.1 (2017), pp. 45–62. DOI: 10.1002/we.1990.
- [105] S. Yarusevych and M. S. Boutilier. “Vortex shedding of an airfoil at low Reynolds numbers”. In: *AIAA journal* 49.10 (2011), pp. 2221–2227.

CURRICULUM VITAE

Education and professional experience

Sébastien Le Fouest Ricci was born on August 17th 1995 in New York, United States of America. He attended the Lycée International de Ferney-Voltaire and obtained the French Baccalaureate with International Option (BOI) in 2013.

After that, he pursued a Master of Engineering (MEng) at Imperial College London. There, he developed a strong interest in fluid dynamics, aerodynamics specifically, and energy sciences. In 2016, Sébastien co-founded CommuniTech London, a charitable organisation that aimed to bridge generations and encourage sustainable communities by providing technological literacy to those suffering from a rapidly digitalising world. He co-directed this organisation as Director of Services until 2020 when the global pandemic made it impossible to deliver their service. He graduated with first-class honours in 2017, delivering a master thesis on the life-cycle analysis of tidal turbines to be commissioned in France and Costa Rica.

After six months working at a start-up in the British gas industry as a technical writer, Sébastien found his dream PhD position at the Unsteady Flow Diagnostics Laboratory, EPFL. In June 2018, he moved to Lausanne to experimentally investigate the occurrence of dynamic stall on vertical-axis wind turbines under the supervision of Karen Mulleners. During his PhD, Sébastien developed a strong interest in science communication, winning several prizes in this discipline. Most notably, Sébastien qualified for the 2020 Swiss Final of the My Thesis in 180 s after being awarded third prize at the EPFL final. On December 9th 2022, Sébastien successfully defended this thesis.

Relevant publications and conference proceedings

S. Henne, S. Le Fouest, and K. Mulleners. “Dynamic stall on an airfoil undergoing VAWT blade angle of attack variations”. In: *Journal of Physics: Conference Series*. Vol. 1618. 5. IOP Publishing Ltd, 2020, p. 52033. DOI: 10.1088/1742-6596/1618/5/052033

S. Le Fouest, J. Deparday, and K. Mulleners. “The dynamics and timescales of static stall”. In: *Journal of Fluids and Structures* 104 (2021), p. 103304. DOI: 10.1016/j.jfluidstructs.2021.103304

D. Bensason et al. “Greenberg’s Force Prediction for Vertical-Axis Wind Turbine Blades”. In:

Bibliography

AIAA Journal (2022), pp. 1–4. DOI: 10.2514/1.J061417

D. Bensason et al. “Strategy for diagnosing the degree of dynamic stall on a vertical-axis wind turbine blade”. In: *AIAA Science and Technology Forum and Exposition, AIAA SciTech Forum 2022* (2022). DOI: 10.2514/6.2022-1786

S. Le Fouest, D. Bensason, and K. Mulleners. “Asymmetry of timescales, loads, and flow structures for a vertical-axis wind turbine blade”. In: *AIAA SCITECH 2022 Forum*. San Diego, USA: American Institute of Aeronautics and Astronautics (AIAA), 2022, pp. 1–12. DOI: 10.2514/6.2022-1788

S. Le Fouest and K. Mulleners. “The dynamic stall dilemma for vertical-axis wind turbines”. In: *Renewable Energy* 198 (2022), pp. 505–520. DOI: 10.1016/j.renene.2022.07.071

S. Le Fouest, D. Fernex, and K. Mulleners. “Timescales of dynamic stall development on a vertical-axis wind turbine blade”. In: *arXiv* (2022). DOI: 10.48550/arxiv.2210.16259